Free-Standing Nanomechanical and Nanophotonic Structures in Single-Crystal Diamond

Free-standing nanomechanical and nanophotonic structures in single-crystal diamond

A dissertation presented

by

Michael John Burek

to

The School of Engineering and Applied Sciences

in partial fulfillment of the requirements

for the degree of

Doctor of Philosophy

in the subject of

Applied Physics

Harvard University

Cambridge, Massachusetts

December 2015

Dissertation advisor: Marko Lončar Michael John Burek

Free-standing nanomechanical and nanophotonic structures in single-crystal diamond

Abstract

Realizing complex three-dimensional structures in a range of material systems is critical to a variety of emerging nanotechnologies. This is particularly true of nanomechanical and nanophotonic systems, both relying on free-standing small-scale components. In the case of nanomechanics, necessary mechanical degrees of freedom require physically isolated structures, such as suspended beams, cantilevers, and membranes. For nanophotonics, elements like waveguides and photonic crystal cavities rely on light confinement provided by total internal reflection or distributed Bragg reflection, both of which require refractive index contrast between the device and surrounding medium (often air). Such suspended nanostructures are typically fabricated in a heterolayer structure, comprising of device (top) and sacrificial (middle) layers supported by a substrate (bottom), using standard surface nanomachining techniques. A selective, isotropic etch is then used to remove the sacrificial layer, resulting in free-standing devices. While high-quality, crystalline, thin film heterolayer structures are readily available for silicon (as silicon-on-insulator (SOI)) or III-V semiconductors (i.e. GaAs/AlGaAs), there remains an extensive list of materials with attractive electro-optic, piezoelectric, quantum optical, and other properties for which high quality single-crystal thin film heterolayer structures are not available. These include complex metal oxides like lithium niobate (LiNbO3), silicon-based compounds such as silicon carbide (SiC), III-V nitrides including gallium nitride (GaN), and inert single-crystals such as diamond.

Diamond is especially attractive for a variety of nanoscale technologies due to its exceptional physical and chemical properties, including high mechanical hardness, stiffness, and thermal conductivity. Optically, it is transparent over a wide wavelength range (from 220 nm to the far infrared), has a high refractive index ($n \sim 2.4$), and is host to a vast inventory of luminescent defect centers (many with direct optical access to highly coherent electron and nuclear spins). Diamond has many potential applications ranging from radio frequency nanoelectromechanical systems (RF-NEMS), to all-optical signal processing and quantum optics. Despite the commercial availability of wafer-scale nanocrystalline diamond thin films on foreign substrates (namely SiO_2), this diamond-on-insulator (DOI) platform typically exhibits inferior material properties due to friction, scattering, and absorption losses at grain boundaries, significant surface roughness, and large interfacial stresses. In the absence of suitable heteroepitaxial diamond growth, substantial research and development efforts have focused on novel processing techniques to yield nanoscale single-crystal diamond mechanical and optical elements.

In this thesis, we demonstrate a scalable 'angled-etching' nanofabrication method for realizing nanomechanical systems and nanophotonic networks starting from bulk single-crystal diamond substrates. Angled-etching employs anisotropic oxygen-based plasma etching at an oblique angle to the substrate surface, resulting in suspended optical structures with triangular cross-sections. Using this approach, we first realize single-crystal diamond nanomechanical resonant structures. These nanoscale diamond resonators exhibit high mechanical quality-factors (approaching $Q \sim 10^5$) with mechanical resonances up to 10 MHz.

Next, we demonstrate engineered nanophotonic structures, specifically racetrack resonators and photonic crystal cavities, in bulk single-crystal diamond. Our devices feature large optical Q-factors, in excess of 10^5, and operate over a wide wavelength range, spanning visible and telecom. These newly developed high-Q diamond optical nanocavities open the door for a wealth of applications, ranging from nonlinear optics and chemical sensing, to quantum information processing and cavity optomechanics. Beyond isolated nanophotonic devices, we also developed free-standing angled-etched diamond

waveguides which efficiently route photons between optical nanocavities, realizing true on-chip diamond nanophotonic networks. A high efficiency fiber-optical interface with aforementioned on-chip diamond nanophotonic networks, achieving > 90% power coupling, is also demonstrated.

Lastly, we demonstrate a cavity-optomechanical system in single-crystal diamond, which builds upon previously realized diamond nanobeam photonic crystal cavities fabricated by angled-etching. Specifically, we demonstrate diamond optomechanical crystals (OMCs), where the engineered co-localization of photons and phonons in a quasi-periodic diamond nanostructure leads to coupling of an optical cavity field to a mechanical mode via the radiation pressure of light. In contrast to other material systems, diamond OMCs possess large intracavity photon capacity and sufficient optomechanical coupling rates to exceed a cooperativity of ~ 1 at room temperature and realize large amplitude optomechanical self-oscillations.

Page intentionally left blank.

Contents

Author list

Portions of Chapter 2 appeared in the following publications and issued patent:

Burek M.J., de Leon N.P., Shields B.J., Hausmann B.M., Chu Y., Quan Q., Zibrov A.S., Park H., Lukin M.D., and Lončar M., "Free-standing mechanical and photonic nanostructures in single-crystal diamond" *Nano Letters*, **12** (12), 6084–6089, (2012).

Atikian H.A., Eftekharian A., Salim A.J., **Burek M.J.**, Choy J.T., Majedi A.H., and Lončar M., "Superconducting nanowire single photon detectors on diamond" *Applied Physics Letters* **104**, 122602, (2014). (*arXiv*:1401.4490)

U.S. Patent No. 8,999,105, (issued Apr. 7, 2015), "SMALL-SCALE FABRICATION SYSTEMS AND METHODS" by M. Lončar, M.D. Lukin, **M.J. Burek**, N.P. de Leon, and B.J. Shields.

Chapter 3 appeared in the following publication:

Burek M.J., Ramos D., Patel P., Frank I.W., and Lončar M., "Nanomechanical resonant structures in single-crystal diamond" *Applied Physics Letters* **103**, 131904, (2013). (*arXiv*:1309.1834)

Portions of Chapter 4 appeared in the following publication and patent application, as well as a manuscript in preparation:

Burek M.J., Chu Y., Liddy M.S.Z., Patel P., Rochman J., Meesala S., Hong W., Quan Q., Lukin M.D., and Lončar M., "High-Q optical nanocavities in bulk single-crystal diamond" *Nature Communications* **5** (5718), 1-7 (2014). (*arXiv*:1408.5973)

U.S. Patent Application No. 2015/0036975 A1, (filing date Feb. 5, 2015), "DEVICE SUPPORT STRUCTURES FROM BULK SUBSTRATES" by **M.J. Burek** and M. Lončar.

Burek M.J., Meuwly C., Meesala S., Rochman J., Atikian H.A., Ruelle T., Venkataraman V., and Lončar M., "Fiber-integrated diamond nanophotonic networks in bulk single-crystal diamond" In preparation (2015).

Chapter 5 appeared in the following manuscript preprint:

Burek M.J., Cohen J.D., Meenehan S.M., Meesala S., Ruelle T., Rochman J., Atikian H.A., Markham M., Twitchen D.J., Painter O., and Lončar M., "Single-crystal diamond optomechanics" *arXiv*:1512.04166 (2015).

Portions of Chapter 6 appeared in the following manuscript in preparation:

Sipahigil A., Evans R.E., Sukachev D.D., **Burek M.J.**, Nguyen C., Borregaard J., Bhaskar M., Pacheco J., Atikian H.A., Camacho R.M., Jelezko F., Bielejec E., Park H., Lončar M., and Lukin M.D., "Quantum optical switch controlled by a color center in a diamond nanocavity" In preparation (2015).

List of figures

List of tables

To my beloved parents, John and Marilena Burek, I dedicate this work.

Acknowledgements

First and foremost, I must thank my adviser Professor Marko Lončar. Since beginning my graduate studies in August 2010, Marko has been an overwhelmingly positive and supportive person in my life, in both the high points of great results and accepted papers, as well as lower points spent dealing with what we would call "metaphysics". I feel both blessed and incredibly lucky to have joined his group, and continue to view Marko's patience, fairness, and friendly demeanor as an example I strive to emulate. Though I have my many memories of Marko throughout my time in the Lončar group, one which defines our relationship is the many individual meetings we had. While I remember countless times entering these meetings either stressed or feeling under duress from competition with researchers in our community, around our own campus, or even in our own group, I only ever remember leaving our meetings feeling reassured and reenergized to continue the work at hand. Marko's positivity and ability to help me rise above the noise was a large factor in my success over the past five and a half years. Lastly, I must thank Marko for his willingness to let me operate in his group in a very independent and self-directed manner. He provided me the freedom to tackle projects of interest at my pace, allowed me to hire and direct undergraduate interns and Master's students, and gave me the opportunity to travel and attend many conferences around the USA and abroad. For these reasons and more, I say thank you Marko for making my time at Harvard as special as it was.

I would like to acknowledge and extend my deepest gratitude to my committee members Professor Evelyn Hu and Professor Mikhail Lukin. Though I did not actually have the chance to work directly with Prof. Hu, her constant support was greatly appreciated over my time at Harvard. I especially valued her guidance during our many plasma etching efforts in the Harvard Center for Nanoscale Systems (CNS), as

well as her comments and feedback on this thesis during the time of my Ph.D. defense. Since my very first year at Harvard, I have had the incredible opportunity to work closely with Prof. Lukin and his students. While our initial joint efforts began in an admittedly rocky manner, I was very happy our relationship prevailed and my collaboration with his group has enjoyed much success in the past several years. I must also sincerely thank Professor Oskar Painter from Caltech, who joined my committee during my Ph.D. defense, and has been a close collaborator over the past two years of my Ph.D. work. Without his involvement and guidance, it is unlikely our final efforts on diamond optomechanics would have be as successful as they were. Finally, I would also like to thank both Professor Eric Mazur and Professor Donhee Ham, who also served on my committee during my qualifying exam.

I would like to acknowledge and thank the Lončar group – both past and present – for making my time at Harvard an incredible experience. When I joined the Lončar group, a few years prior to Marko's tenure appointment, I was fortunate to have many senior graduate students and postdoctoral fellows as excellent examples to learn from. Tom Babinec, in particular, was a huge help in my first two years, as an outlet for talking about research and also working with me to understand how I should shape and frame my thesis. Qimin Quan supported me greatly as I first started to learn and study photonics, and his efforts guiding me through photonic crystal design were (and still are) immensely helpful. Jennifer Choy and Birgit Hausmann were very important early on, as I ventured into the clean room and started to work with diamonds. Birgit's initial guidance and continued collaboration in my first three years were hugely influential to my early success with new ways to fabricate diamond nanostructures. Jennifer, as my neighbor in the office, was constantly there to chat and help me work through developing new techniques in the clean room. Yinan Zhang and Raji Shankar were awesome officemates and great people to vent/chat with. Their positive attitudes were a constant example for me. Daniel Ramos and Ian Frank were hugely helpful during my initial efforts with diamond nanomechanics. Daniel was the first person to help me venture out of the clean room and into the optics lab, and for his patience and initial guidance I

am deeply grateful. Finally, Shota Kita was an awesome office/lab mate and friend, and his work effort and humbleness remain a constant example for me.

The present members of the Lončar group include some very close friends and have all made our time in the clean room, lab, and office worlds more fun. I must thank Vivek Venkataraman, Stefan Kalchmair, Young-Ik Sohn, and Srujan Meesala, Anna Shneidman, I-Chun Huang, Cheng Wang, Zin Lin, Pawel Latawiec for their valued friendship and support. As office and lab mates they have been there with me through the trials of doing experiment research, dealing with Marko, helping to organize and maintain the lab, and generally making life around Harvard a better place. I especially want to thank Haig Atikian, my neighbor in the office and fellow Canadian. Haig, and I have shared some incredible memories over the years, both inside and outside of the lab. I was blessed to have a close friend like Haig there through thick and thin, and I will never forgot our road trips back home to Toronto, trips for late night junk food after finishing problem sets or long hauls in the clean room, grilling on his porch after hitting the gym, our conference trip to Nashville and visit to Delaware, and the countless other times we just hung out and talked about life, research and everything in between. Throughout every rough period I have had in the lab these past five years, Haig was there talking me through it and a constant pillar of support. Thank you buddy, I'll never forget it.

I would also like to thank Peter Stark and Kathleen Masse. Peter was a great help in the last few years as we restructured the lab and our experiments. Kathleen is in many ways the perfect staff assistant for Marko and the Lončar group. I appreciate all her help tracking down Marko for meetings, handling reimbursements for all the conferences and trips Marko sent me on, and with the many eBay and other purchases I made while building up the lab. I must also acknowledge the Lončar lab interns I was fortunate to work with: Parth Patel, Madelaine Liddy, Jake Rochman, Thibaud Ruelle, Charles Meuwly, and Nayera El-Sawah. I am very thankful to have had the opportunity to work with all of you, and feel like I was the one who learned the most in our time together.

Beyond the Lončar group, I must acknowledge and thank my many collaborators and friends around and outside the Harvard community. From the Lukin group, I have been extremely fortunate to work with incredibly talented people, including Alp Sipahigil, Ruffin Evans, Denis Sukachev, Yiwen Chu, Nathalie de Leon, and Brendan Shields. Most recently, Alp and Ruffin have been amazing collaborators, and I look forward to continued success working with them. From the Painter group at Caltech, I must thank Justin Cohen and Seán Meenehan, who were instrumental in the success of the diamond optomechanics project. I would like to thank Mikhail Kats, Andrew Magyar, Tony Zhou, Daniel Wintz and Alex Woolf for many great conversations around the hallways on campus and the clean room. I want to also acknowledge Daniel Twitchen, Matthew Markham, and Harpreet Dhillion from Element Six, and Joe Tabeling and Peter Morton from Delaware Diamond Knives. Thank you for your immense help securing diamond samples, in enough quantity to be able to make mistakes in the clean room, and turning around re-polished diamond plates quickly and at a high quality. Finally, I am deeply grateful to all the technical staff at the Harvard CNS, in both the nanofabrication and imaging facilities, for their continued hard work and support: Jiangdong Deng, Yuan Lu, David LaFleur, Steve Paolini, Ling Xie, Mac Hathaway, Ed Macomber, Jason Tresback, Greg Lin, David Bell, Dave Lange, Andrew Magyar, Adam Graham, and Jules Gardener. Thank you for being the lifeline throughout my research, keeping the tools I relied on up and running. Absolutely none of the work in this thesis would have been possible without their efforts.

On a final, more personal note, my success over the time I've spent at Harvard is deeply rooted in a support network of friends and family back home in Canada and around Boston. I must thank my parents, John and Marilena Burek, my brother Christopher Burek, and my grandparents Frank and Lidia Burek, and Lena and Salvatore Cardamone. Without their love and constant support, I would not have had the focus and energy to complete my journey from undergrad at Waterloo to graduate school at Harvard. I also am deeply grateful to Ting Tsui, my undergraduate adviser, and the person responsible for my acceptance to Harvard. His constant support, both personally and professionally, since we met in 2009 has been hugely important to me. I would also like to thank my close friends I grew up with in Waterloo, the

Big Cats group. You boys were always there to fall back on and keep me going. Especially, Ryan Iutzi, my brother in arms since the time we both realized we were into math and science and decided to give Nanotechnology Engineering at Waterloo a try. Somehow we ended up on a on a path together which has taken us from elementary and high school, through five years of undergrad, and another nearly six years together in Boston for graduate school at MIT and Harvard. I am not sure who followed who, but we did it together and I know I could not have done it without you. Finally, I would like to thank the friends I've made since moving to Boston back in 2010, people I have come to love and cherish in a city I never thought would feel as much like home as it does: Jesse Keenan, Brandon Lehoux, Haig Atikian, Jeremy Armstrong, Christine Zgrabik, Philip Preiss, Ben Good, and Shelly Upton. It's been an incredible ride, always ridiculous, sometimes bumpy (especially waking up the morning after a night spent at Coogans or Bell in Hand), but I would not change it for the world.

Chapter 1

Background

With their extraordinary glamour and attraction, natural diamonds have been heavily sought after throughout modern history (albeit controversially at times [1]). The prominence of diamond jewelry stems from the stone's superlative physical qualities: its optical brilliance and seemingly timeless lifespan. However, unlike materials similarly revered by jewelers such as platinum or gold, diamond is readily synthesized. Man-made diamonds have only existed since the 1950s [2], yet today are produced at an estimated rate of nearly 4500 million carats (900 metric ton) per year as of 2015 estimates [3], exceeding all mine production by nearly fifty times (importantly, production of industrial-quality natural diamonds is merely a byproduct of gem-quality diamond mining). Industrial uses of synthetic diamond are well rooted in its extreme hardness and thermal conductivity (the highest of any bulk material [4]). Accordingly, synthetic diamond bits are ubiquitous components in mining, drilling, and precision machining applications [5]. Nevertheless, the overwhelming majority of synthetic diamond production yields "bort" grade material: dark shards with varying levels of crystallization and opacity.

With continually improving and expanding growth techniques – namely the evolution of low pressure chemical vapor deposition (CVD) [6] – synthetic diamond has witnessed resurgence in the last two decades as a viable engineering material for advanced mechanical, thermal, and optical applications. Specifically, the realization of diamond substrates with high thermal conductivity [7], and ultra-low stain-related birefringence and absorption [8] – now available up to 120 mm in diameter and 2 mm thick in the case of polycrystalline material [9]– has generated commercial success in optical solutions for high-power laser applications [8-10] and thermal management solutions for ultra-high-speed gallium nitride (GaN)

integrated circuits [11-13]. Moreover, the availability of high-quality and isotopically pure single-crystal diamond substrates [14, 15] have enabled major joint academia-industry research initiatives focused on diamond optical-spintronics for quantum information science and technology (QIST).

1.1. OPPORTUNITIES FOR NANOSCALE OPTICS IN DIAMOND

The material properties of diamond [4, 16] (summarized in Table 1, in comparison to competing materials) feature a high refractive index (n ~ 2.4), and a wide transparency window spanning the ultraviolet (band edge at 0.22 μm) to the mid-infrared, apart from a moderate absorption band between 2.5 and 6.5 μm due to multi-phonon excitation [4, 8-10, 17]. In combination with its mechanical and chemical robustness, low absorption, and its high thermal conductivity and small thermal expansion, diamond can withstand significant optical power densities while avoiding thermal lensing [8]. Consequently, manufacturers of kW-class CO_2 lasers have long made extensive use of optics machined from CVD polycrystalline diamond [18]. Along similar lines, its broadband transparency and high damage threshold make diamond well suited for exploiting nonlinear optical effects, which have applications in areas such as telecommunications, signal processing, and metrology [19-22]. While diamond is a centrosymmetric crystal, and thus possesses only an intrinsic third-order nonlinear susceptibility ($\chi^{(3)}$) [23], its large intensity-dependent refractive index (the Kerr coefficient) of $n_2 = 1.3\text{x}10^{-19}$ m^2/W [24, 25] is comparable to that of materials like silicon nitride (Si_3N_4, $n_2 = 2.5\text{x}10^{-19}$ m^2/W) [19, 20], which have already proven to be good candidates for integrated nonlinear optics at telecom wavelengths. Additionally, diamond has the largest Raman gain coefficient (~ 15 $cm \cdot GW^{-1}$) among all relevant materials [26]. Stimulated Raman scattering in diamond could potentially yield coherent sources of substantial power, operating at wavelengths inaccessible by current technologies.

Table 1.1 | Optical, mechanical, and thermal properties of diamond and competing materials. In this plot, E_g is the bandgap energy, E is the Young's modulus, κ is the thermal conductivity, ρ is the mass density, and c is the sound velocity.

	E_g (eV)	Transmission window (μm)	Refractive index (n)	E (GPa)	κ (W/m·K)	ρ (g/cm^3)	c (m/s)
Diamond	5.47	0.22 - 20	2.4	1100	2200	3.52	17700
Si	1.12	1.1 - 6.5	3.5	162	140	2.33	8300
Si_3N_4	5	0.3 - 5.5	2	800	33	3.24	15800
3C-SiC	2.39	0.2 - 5	2.6	390	1.4	3.21	11000
SiO_2	9	0.38 - 2.2	1.5	95	10	2.65	6000
Sapphire	9.9	0.17 - 5.5	1.8	340	24	3.98	9200
AlN	6.14	0.2 - 13.6	2.1	294	150	3.26	9500
GaN	3.44	0.36 - 7	2.4	294	130	6.1	6900
GaP	2.26	0.54 - 10	3.2	140	100	4.13	5800
GaAs	1.42	0.9 - 17.3	3.7	116	52	5.32	4700
InP	1.34	0.93 - 14	3.5	89	68	4.8	4300
ZnO	3.4	0.37 -	2	110	30	5.6	4400
TiO_2	3.5	0.42 - 4	2.5	250	10	4.26	7700

Whereas nonlinear optical processes in bulk materials suffer from low efficiencies, employing wavelength-scale optics such as on-chip waveguides and cavities (i.e. nanophotonics) enables superior light confinement and field enhancements [27-29], thus tailoring strong light-matter interactions. In the case of Raman-scattering in diamond, engineered high quality factor (Q-factor) optical cavities resonant with an incident pump beam and at the phonon scattered Stokes wavelength would provide the necessary optical feedback to stimulate the process and achieve lasing action [27, 30]. The lasing power threshold in such a system scales directly with the photon lifetime of the resonant cavity modes (i.e. inversely with optical Q-factor), and is also linearly proportional with the cavity mode volumes [31]. Indeed, orders of magnitude smaller threshold powers – reaching the mW range – were demonstrated in on-chip optical cavities [32] compared to bulky, external-cavity geometries (Watt level thresholds) [26, 33-37]. As well, since the intrinsic material dispersion of diamond is normal for visible to infrared wavelengths, the engineered geometrical dispersion afforded by nanoscale diamond waveguides is necessary to yield net

anomalous cavity dispersion [19, 20]. Hence, nanophotonics would enable compact, on-chip diamond frequency combs based on four-wave mixing by the $\chi^{(3)}$ nonlinearity [25]. Finally, integrated and compact, chip-scale diamond nanophotonics are of interest for their scalability and mass-producibility.

1.1.1. DIAMOND: A QUANTUM OPTICAL MATERIAL

Along with its desirable optical properties, diamond is also rich in lattice defects revealing the optical activity of their electronic and vibrational transitions, with in excess of 500 optical defect centers known [17, 38]. In the case of luminescence defect centers (i.e. color centers) the large diamond bandgap energy (~ 5.5 eV) is a particularly favorable condition, as radiative transitions require that both the ground and excited electronic states lie within the bandgap. Moreover, diamond's extreme stiffness and thus, high Debye temperature (~ 2000 K) [4], limits significant electro-phonon coupling to lattice modes of optical defects. This makes diamond color centers unique compared to other solid-state emitters (i.e. epitaxial quantum dots) in that many provide stable, coherent single photon fluorescence at room [39, 40] and even elevated temperatures [41]. For a small subset of diamond color centers, optical signatures of an associated electron spin has been observed and subsequently exploited for applications including quantum information processing (QIP) and magnetometry [38, 42]. Without doubt, the most notable of this faction is the negatively charged nitrogen vacancy center (NV^-, zero phonon line (ZPL) at ~ 637 nm), as its spin-dependent fluorescence can be used to optically read out its electron spin polarization [39, 43, 44]. Initialization of the NV^- center electron spin is also performed optically, and its state manipulated with microwave fields. Last but not least, unlike spins associated with quantum dots in III-V semiconductor systems, a diamond lattice comprised of the spin-free ^{12}C (98.9% naturally abundant) yields exceptional coherence times, reaching nearly ~ 2 ms at room temperature for NV^- centers in ultrapure, isotopically

enriched single-crystal diamond substrates [14, 15].

The combination of its electron spin acting as a long lived solid state quantum bit (qubit) able to store information, with emitted single photons carrying the spin state information ("flying" qubits), provides the diamond NV^- center with the quantum mechanical functions necessary for QIP. With NV^- centers buried deep in single-crystal diamond substrates, seminal results including photon entanglement with a single-spin [45], a quantum bit memory exceeding 1 second via coupling to nearby longer-lived ^{13}C nuclear spins [46], two photon interference for the generation of indistinguishable photons [47, 48], entanglement of two distance solid-state qubits [49], and finally, deterministic quantum teleportation over a distance of 3 meters [50], were successfully demonstrated. Most recently, entanglement of the electron spins from two remote NV^- centers in diamond, separated by 1.3 km, enabled the first demonstration of loop-hole free violation of Bell's inequality [51] – strongly supporting the existence of quantum-mechanical entanglement phenomenon.

Building on these results, major advancements are surely to come by engineering the NV^- center emission through coupling to well-defined radiation channels: namely, those provided by diamond nanophotonics [38, 52-54]. Specifically, QIP with optically interfaced diamond NV^- centers faces two major obstacles: (1) most photons emitted by NV^- centers remain inside the diamond as a consequence of total internal reflection (TIR); and (2) the NV^- center has a moderate excited state lifetime ($\tau \sim 12$ ns in bulk), with the majority of its emission spread over a wide band due to phonon-mediated transitions. As such, only 3 to 5 % of emitted photons are in the ZPL at ~ 637 nm, with the remaining fluorescence into a phonon side band (PBS) out to nearly 800 nm. Accordingly, recently demonstrated entanglement between two remote NV^- centers (a landmark result) was constrained to a rate of a single entanglement event only every few minutes, fundamentally limited by the photon production and collection efficiencies [49].

Potentially, QIP with negatively charged silicon vacancy (SiV^-) centers [55] in diamond is a viable solution, as their fluorescence properties boast narrow band emission (> 70 % of photons emitted into the

ZPL at ~ 740 nm) and faster photon production ($\tau \sim 1$ ns in bulk) [56]. Recent experiments focused on the SiV^- spectral properties have revealed its electronic structure [57, 58], as well as observed extremely narrow inhomogeneous distribution in the optical transition frequencies of as-grown SiV^- emitters in the bulk [59], already less than a factor of ten compared to its natural radiative linewidth. This enabled the observation of two-photon quantum interference from a pair of SiV^- centers without the need for spectral tuning [60]. Moreover, unlike the NV^- center, the SiV^- retains its optical coherence as a result of its inversion symmetry and thus, vanishing permanent electric dipole moment for the SiV^- orbitals. As such, the SiV^- does not exhibit significant spectral diffusion stemming from fluctuating charges in the lattice or on the diamond surface [61], a promising attribute in the context of integration with monolithic nanoscale optical components [62]. Lastly, the SiV^- electron spin has recently been optically identified [61, 63], though more work is ultimately necessary to develop a similarly coherent SiV^- spin-photon interface as the NV^- center [64].

Configuring the diamond substrate with broadband collection optics – i.e. machined diamond solid immersion lenses (SILs) [65, 66] or diamond nanowire single photon sources [67] – can substantially improve the collection efficiency of NV^-, SiV^-, or other color center emission. Indeed, these approaches have been used in nearly all the relevant QIP experiments [47-51, 68]. Hence, the development of diamond nanophotonics is necessary for further progression of solid state QIP, as well as future scalability and integration [38, 52-54]. Specifically, resonant coupling of NV^- or SiV^- centers to monolithic diamond optical cavities would provide both the spectral filtering necessary to ensure a high percentage of color center emission into its ZPL, as well as enhancement of the photon production rate (reduced emitter lifetime) via the Purcell effect [62, 69-72]. Even with moderate optical Q-factors ($\sim 10^2$ to 10^3), the wavelength scale mode volume inherent to photonic crystal cavities ($V \sim (\lambda/n)^3$) provides sufficient coupling such that the cavity field may operate as an efficient interface between photons and coherent quantum emitters – an essential element of quantum networks comprised of nonlinear optical devices operating at the single-photon level [73]. Ultimately, diamond nanophotonics is a clear route to practical

devices which are scalable to larger quantum photonic networks involving many color centers as quantum nodes.

1.2. OPPORTUNITIES FOR NANOSCALE MECHANICS IN DIAMOND

Nanomechanical systems [74], i.e. engineered sub-micron scale mechanical components, are of interest for a range of technical and fundamental research, from frequency selective oscillators and passive filters for radio frequency (RF) signal processing and microwave communications [75], to high speed mechanical memory elements [76, 77] and ultrasensitive mass or charge detectors [78, 79]. Specifically, small-scale mechanical systems are ubiquitous in current cellular, GPS, and wireless technologies, where their integrated nature allows for efficient coupling of individual on-chip and on-board components, thus minimizing signal losses. In nearly all aforementioned applications, a key figure of merit which encompasses the mechanical component performance is the product of its natural frequency (f_o) and mechanical Q-factor (Q) [74]. High $f_o \cdot Q$ is essential in passive RF filter applications requiring deep off-band rejection and low phase noise. As well, applications in precision measurements benefit greatly from high $f_o \cdot Q$, since a mechanical resonator's minimum detectable force (F_{min}) per unit bandwidth is set by thermal force noise, as given by:

$$F_{\min} = \sqrt{\frac{4k_c k_b T}{(2\pi) f_o Q}} \tag{1.1}$$

where k_c is the resonator spring constant, and k_bT is the available thermal energy (product of Boltzmann's constant and system temperature) [80-82].

Diamond's superior material properties offer a number of advantages in the realization of nanomechanical systems. Owing to its large Young's modulus (E ~ 1000 GPa) and low mass density (ρ ~ 3.52 g/cm-3), diamond possesses the largest sound velocity ($v_{sound} = \sqrt{E/\rho}$ ~ 18 000 m/s) among all materials relevant for small-scale mechanical systems [16, 83]. Consequently, diamond resonators are able to support higher mechanical resonant frequencies than equivalent geometries in other material platforms. Moreover, diamond exhibits extremely low thermoelastic dissipation (TED), which is the intrinsic loss mechanism limiting mechanical resonators operating in the RF regime [81, 82]. Specifically, as a resonator vibrates, regions of the structure experience counteracting compressive and tensile stresses resulting in temperature gradients; this in turn yields energy loss due to the heat flow. The mechanical Q-factor associated with this TED mechanism can be expressed as [81, 82]:

$$Q_{TED}^{-1} = \Gamma(T)\Omega(f) \tag{1.2}$$

with

$$\Gamma(T) = \frac{\alpha^2 TE}{\rho C_p} \tag{1.3}$$

and

$$\Omega(f) = \frac{f/F_o}{1+(f/F_o)^2} \tag{1.4}$$

In the above expressions, α is the thermal expansion coefficient, T is temperature, E is the Young's modulus, ρ is the mass density, C_p is the heat capacity, f is the resonator linear natural frequency, and F_o is a characteristic frequency set by the thermal time constant for heat transfer, which is dependent on the resonator geometry and material properties. For the simple case of a rectangular cross-section cantilever with thickness t, the expression for F_o is given by [81, 82]:

$$F_o = \frac{\pi\kappa}{2\rho C_p t^2} \tag{1.5}$$

where κ is the thermal conductivity. As made evident by the above relationships, diamond, with its extremely high thermal conductivity, would ultimately enable nanomechanical systems to be engineered with much larger Q-factors than more conventional material platforms, i.e. silicon.

1.2.1. DIAMOND NANOMECHANICS: A ROUTE TO HYBRID QUANTUM SYSTEMS

In addition to classical applications of diamond nanomechanical systems, recent experiments have shown coherent coupling of the diamond NV^- center ground state electronic spin to mechanical resonators

via lattice strain modulation [84-88], thereby opening avenues for phonon-based hybrid quantum systems in diamond. Currently, the spin-phonon coupling rate in these systems can enable manipulation of the NV^- center spin state at large driven mechanical amplitudes, but is insufficient to provide a detectable back-action on the mechanical mode from the spin. This is largely due to the intrinsically small strain susceptibility of the NV^- spin levels, and the relatively large size of the mechanical resonators. One way to boost this interaction into the strong spin-phonon coupling regime would be to engineer truly nanoscale mechanical resonators, with feature sizes of a few hundred nanometers, and with frequencies in the hundreds of MHz to few GHz range – such mechanical modes would provide a large change in local strain per phonon. Such a system may ultimately be used to map non-classical spin qubit states as well as quantum states of light onto phonons and vice-versa [89], and will enable fundamentally new ways to prepare, control, and read out the quantum states of diamond color centers.

1.3. PROGRESS TOWARDS DIAMOND NANOMECHANICAL AND NANOPHOTONIC SYSTEMS

Realizing complex three-dimensional structures in a range of material systems is critical to a variety of emerging nanotechnologies. This is particularly true of nanophotonic and nanomechanical systems, both relying on free-standing small-scale components. In the case of nanomechanics [74], necessary mechanical degrees of freedom require physically isolated structures, such as suspended beams, cantilevers, and membranes. For nanophotonics, elements like waveguides and photonic crystal cavities rely on light confinement provided by TIR or distributed Bragg reflection, both of which require refractive index contrast between the device and surrounding medium (often air) [90, 91]. Such suspended

nanostructures are typically fabricated in a heterolayer structure, comprising of device (top) and sacrificial (middle) layers supported by a substrate (bottom), using standard surface nanomachining techniques [92-94]. A selective, isotropic etch is then used to remove the sacrificial layer, resulting in free-standing devices. While high-quality, crystalline, thin film heterolayer structures are readily available for silicon (as silicon-on-insulator (SOI)) or III-V semiconductors (i.e. GaAs/AlGaAs), there remains an extensive list of materials with attractive electro-optic, piezoelectric, quantum optical, and other properties for which high quality single-crystal thin film heterolayer structures are not available. These include complex metal oxides like lithium niobate (LiNbO3), silicon-based compounds such as silicon carbide (SiC), III-V nitrides including gallium nitride (GaN), and inert single-crystals such as diamond.

Ideally, an integrated nanoscale mechanics or photonics platform in diamond would mimic (to some degree) the planar technologies which have been developed in SOI since the mid-1990s. In the context of silicon nanophotonics, large scale integrated photonic networks comprised of low loss (< 1 db/cm) waveguides are a reality [95-97], and include key passive elements like waveguide splitters/couplers, and high optical Q-factor microring resonators [98] and photonic crystal cavities [99], all operating at infrared wavelengths used by most fiber optic telecommunication systems (namely, $\lambda \sim 1550$ nm). Moreover, efficient off-chip coupling schemes are available [100, 101] (< 0.5 dB insertion loss for state-of-the-art [102]), providing near seamless transition of photons on-chip into commercial optical fibers. Such a requirement is especially pertinent in applications involving single photons, such as quantum optics with diamond color centers [103].

1.3.1 OPTICAL-GRADE SYNTHETIC DIAMOND SUBSTRATES

While the maturity and flexibility of silicon-based nanoscale mechanics and photonics is a result of advanced material processing and fabrication, the infancy of optical grade synthetic diamond brings about

significant challenges to the realization of similar integrated nanomechanics and nanophotonics platforms. Current state-of-the-art synthetic diamond material is produced by CVD using microwave plasmas for the activation method, since it has proven to minimize the amount of impurities incorporated during growth. By microwave plasma CVD, wafer-scale nanocrystalline diamond thin films (with average grain sizes between 10 and 100 nm) on foreign substrates (typically SiO2) are readily available [104]. While recently, such films were used to demonstrate integrated microring resonators at telecom wavelengths [105], substantial propagation losses (in excess of 50 dB/cm) were observed. This was the result of scattering and absorption losses at grain boundaries – which become even more prevalent at shorter wavelengths – and significant film roughness. Moreover, nanocrystalline thin films typically exhibit inferior material properties, large interfacial stresses, and are not suitable for the incorporation of spectrally stable color centers. Similar reasons have also limited the development of diamond-based micron and nanometer scale mechanical systems in wafer-scale nanocrystalline diamond thin films on supporting substrates [104, 106, 107].

Polycrystalline diamond substrates with much larger average grain sizes (on the order of 10 μm), are also available [9], and are routinely used for optical components serving long, mid-IR wavelength applications (i.e. high power CO_2 lasers and infrared spectrometers). However, this material is only grown in hundreds of microns to millimeter thicknesses and is ultimately inapt for shorter wavelength applications, where inter-grain strain yields significant birefringence and grain boundaries remain a sizeable contribution to material loss.

Single-crystal diamond is by and large a more suitable material for diamond nanomechanics and nanophotonics operating in the visible to near-infrared spectrum. Commercially available single-crystal diamond substrates are grown with the lowest levels of background impurities (for instance, nitrogen as low as ~ 1 ppb), minimal strain-related birefringence, and nearly isotopically pure (99.7% ^{12}C enriched) [8, 9, 15]. Such high quality, low optical loss single-crystal material enables the incorporation of color centers suitable for QIP experiments [14, 15], as well as boasts the best reported physical properties for

synthetic diamond [7]. Unfortunately, CVD grown single-crystal diamond is only available via homoexpitaxial growth on a pre-existing single-crystal seed or substrate [6]. Though some limited efforts towards heteroepitaxial growth of thick single-crystal diamond films on lattice-matched iridium substrates [108] has been reported, the overall quality of this material is considerably less than homoexpitaxial grown diamond.

1.3.2. BULK SINGLE-CRYSTALS VERSUS MEMBRANES

In the absence of suitable heteroepitaxial growth, substantial efforts by the diamond nanomechanics, nanophotonics, and quantum optics communities have focused on novel processing techniques to yield engineered nanostructures in single-crystal diamond. The majority of this work has centered on developing a thin film diamond-on-insulator (DOI, where the insulator is SiO_2) technology, followed by conventional planar fabrication techniques to realize either supported or suspended diamond nanomechanical or nanophotonic devices. Towards DOI, crystal ion slicing techniques – analogous to SOI fabrication – have been utilized [109-117]. Ion slicing of single-crystal diamond employs high energy ion-bombardment (typically ~ MeV He^+) to form a sub-surface damaged graphite-like layer, which may be subsequently removed by electrochemical etch. As well, newly developed homoexpitaxial regrowth on single-crystal diamond ion sliced membranes have advanced this methodology [118]. Though nanophotonic devices have been demonstrated with this method, ion slicing has not achieved widespread use due to sizeable limitations in the ability of high temperature annealing to repair residual crystal damage and release large film stresses resulting from ion bombardment and subsequent thermal treatments.

For the most part, efforts towards DOI have involved heterogeneous integration of laser cut single-crystal diamond slabs (commercially available from ~ 5 to 30 μm thick) onto supporting silica substrates,

with subsequent oxygen plasma etching to thin the slab near a target thickness ~ 500 nm or less. Mechanical resonators [80, 119, 120], optical microring resonators [25, 32, 69, 121-123], and photonic crystal cavities [62, 70, 72] have been realized in such thinned diamond membranes, with recent results demonstrating ultra-low propagation loss optical waveguides at slightly less than 1 dB/cm [25, 32]. While this approach remains promising, complications due to material handling, scalability, repeatability, and sheer difficulty of removing tens of microns of diamond while preserving uniform hundred-nanometer scale films limit this approach significantly. Moreover, the integration of diamond thin films on foreign substrates places considerable restrictions on post processing techniques needed to stabilize implantation-defined color centers, which often include high temperature (up to ~ 1200 ^{o}C) annealing [124-126].

Prompted by the shortcomings of demonstrated DOI platforms, the community has also explored focused ion beam (FIB) milling of diamond nanostructures in bulk diamond single-crystal substrates [127-129]: a significant departure from conventional planar fabrication wisdom. The three-dimensional capabilities of FIB patterning enabled carving of free-standing diamond nanostructures from a bulk substrate, thus providing the necessary refractive index contrast for operation. However, FIB-induced artifacts – including Ga^{+} implantation and crystal damage, redeposited material, tapered sidewalls, and one-of-a-kind devices – generally compromise the final material quality and irrefutably limit device performance.

With inspiration from FIB milling, we have conceived and developed a scalable three-dimensional nanofabrication method for suspended nanostructures from bulk single-crystal diamond substrates. This fabrication process employs anisotropic oxygen plasma etching performed at an oblique angle to the substrate surface (referred to hereafter as "angled-etching"). Angled-etching yields free-standing nanobeams – with triangular cross-sections – directly from single-crystal diamond substrates, and has been used to demonstrated high Q-factor nanomechanical resonators and nanoscale optical cavities in single-crystal diamond, as well as the first demonstration of a diamond cavity-optomechanical system operating in the resolved sideband regime.

1.4. OUTLINE OF THESIS

Herein, we describe the aspects of angled-etching, an unconventional, yet scalable fabrication platform, which we have developed to demonstrate state-of-the art nanomechanical and nanophotonic resonators in bulk single-crystal diamond substrates. Chapter 2 describes the original proof-of-concept demonstration of angled-etching [130, 131], accompanied by optimized fabrication details and post-fabrication device inspections.

In Chapter 3, the mechanical resonance characteristics of freestanding, single-crystal diamond nanobeams fabricated by angled-etching techniques are reported [132]. Resonance frequencies displayed evidence of significant compressive stress in doubly clamped diamond nanobeams, while cantilever resonance modes followed the expected inverse-length-squared trend. Mechanical Q-factors on the order of 10^4 to 10^5 were recorded in high vacuum.

Chapter 4 describes the realization of key nanophotonics devices (racetrack resonators and photonic crystal cavities) in single-crystal diamond by angled-etching [133]. These devices feature large optical Q-factors, in excess of 10^5, and operate over a wide wavelength range, spanning visible and telecom. Additionally, we describe the fabrication and characterization of on-chip nanophotonic networks in bulk single-crystal diamond, and demonstrate a high efficiency (> 90 % power coupling) fiber-optical interface with aforementioned on-chip diamond nanophotonic devices.

In Chapter 5 we describe the demonstration of a cavity-optomechanical systems in single-crystal diamond [134], which builds upon previously realized diamond nanobeam photonic crystal cavities fabricated by angled-etching. Specifically, we demonstrate diamond optomechanical crystals, where the

engineered co-localization of photons and phonons in a quasi-periodic diamond nanostructure leads to coupling of an optical cavity field to a mechanical mode via the radiation pressure of light.

In Chapter 6, we describe a recent significant collaborative effort utilizing diamond nanotechnologies realized by angled-etching. Several appendices are also included to supplement the information and discussions included in each chapter.

Chapter 2

Angled-etching nanofabrication of diamond nanostructures

The key aspect of our angled-etching nanofabrication approach, illustrated in Figures 2.1 (a), is the realization of anisotropic oxygen-based plasma etching at an oblique angle to the substrate surface, resulting in undercut and eventually suspended nanostructures with triangular cross-sections. Single-crystal diamond nanobeams fabricated in this manner will support mechanical resonances, as well as guided optical modes given the refractive index contrast afforded by the free-standing structure. Angled-etching is performed in a standard inductively coupled plasma-reactive ion etcher (ICP-RIE), however the diamond substrate is housed within a specifically designed aluminum Faraday cage which modifies the trajectory of the incident plasma ions towards the sample surface. Specifics regarding the fabrication procedure are given in Section 2.1, with details of the Faraday cage designs provided in Section 2.2. Proof-of-concept device prototypes are discussed in Section 2.3, and post-fabrication device inspections are described in Section 2.4.

2.1. ANGLED-ETCHING NANOFABRICATION DETAILS

Angled-etching fabrication of diamond devices (schematically illustrated in Figure 2.1 (b)) begins with standard optical grade single-crystal diamond (CVD grown type IIa substrates, < 1 ppm [N],

Element Six), typically 3 x 3 mm^2 in area. While larger, higher purity single-crystal diamond substrates (i.e. up to ~ 25 mm^2 CVD grown 'electronic grade' substrates, < 5 ppb [N], Element Six) are available; financial limitations and material availability restrict their use to select applications. Throughout this work, <100>-oriented diamond substrates were used, however angled-etching techniques may also be applied to <110> and <111> oriented substrates as well. Received substrates are initially polished to a surface roughness < 5 nm RMS (performed commercially by Delaware Diamond Knives, Inc.), followed by cleaning in a boiling mixture consisting of equal parts concentrated sulfuric, nitric, and perchloric acid.

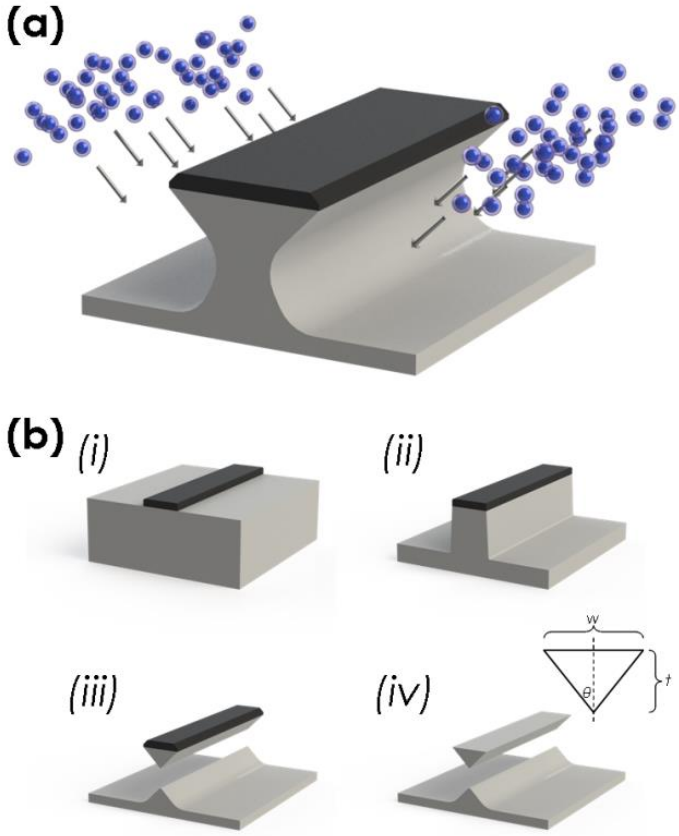

Figure 2.1 | Angled-etching nanofabrication scheme. **(a)** Illustration of the angled-etching fabrication scheme used to realize free-standing structures in bulk single-crystal diamond. **(b)** Angled-etching fabrication steps: *(i)* define an etch mask on substrate via standard fabrication techniques, *(ii)* transfer etch mask pattern into the substrate by conventional top down plasma etching, *(iii)* employ angled-etching to realize suspended nanobeam structures, *(iv)* remove residual etch mask.

Cleaned, polished substrates are then treated to a pre-fabrication surface preparation performed in a UNAXIS Shuttleline ICP-RIE. This includes a 30 minute etch with the following parameters: 400 W ICP power, 250 RF power, 25 sccm Ar flow rate, 40 sccm Cl_2 flow rate, and 8 mTorr chamber pressure, immediately followed by a second 30 minute etch with the following parameters: 700 W ICP power, 100 RF power, 50 sccm O_2 flow rate, and 10 mTorr chamber pressure. The purpose of this pre-fabrication step is to remove several microns from the top of the diamond substrate which are likely strained due to initial mechanical polishing, and also reduce the surface roughness to < 1 nm RMS [135]. Figure 2.2 (a) and (b) display large area representative atomic force microscope (AFM) images of a single-crystal diamond substrate before and after surface preparation respectively, with a significant reduction in overall surface roughness apparent. Striations on the diamond surface observed in Figure 2.2 are the result of diamond polishing carefully aligned to the high wear direction of the diamond, also known as the "easy direction" [136]. In the case of the <100>-oriented diamond substrate, the easy direction on the (100) surface plane is along the <100> direction. Striations are significantly reduced in the final polished and pre-etched surfaces (Figure 2.2 (b)), but are exceedingly difficult to remove completely.

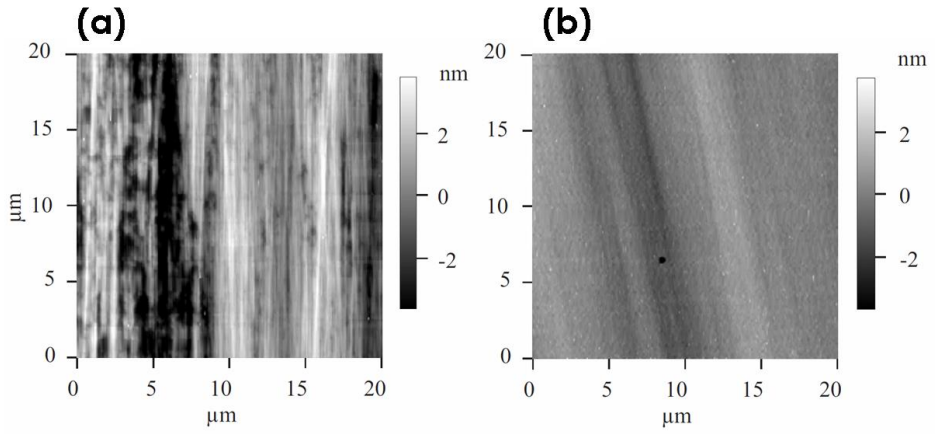

Figure 2.2 | Surface preparation of polished single-crystal diamond substrates. AFM images of a representative <100>-oriented CVD type IIa diamond substrate (a) as received after mechanical polishing carefully aligned to the easy access (performed by Delaware Diamond Knives), and (b) after surfaced preparation by extended Ar/Cl_2 and O_2 plasma etching processes. The surfaces RMS is approximately 1 to 2 nm and ~ 300 pm in (a) and (b) respectively.

Following surface preparation, a silica etch mask is patterned on the diamond substrates using hydrogen silsesquioxane (HSQ, FOX®-16 from Dow Corning) negative resist and electron beam lithography. Prior to spin-coating HSQ, the bare diamond substrate surface was coated in a ~ 20 to 40 nm thick layer of titanium, deposited by electron beam lithography. The purpose of this titanium layer was to promote adhesion of the exposed HSQ resist during the development and subsequent plasma etching steps, as well as provide a charge compensation layer during electron beam lithography. Exposure of the HQS is done via an electron beam lithography system operating at 125 kV (Elionix F-125). Unexposed HSQ is removed in tetramethylammonium hydroxide (TMAH, 25% diluted solution).

The exposed HSQ (silica) etch mask pattern is transferred into the diamond via a conventional top down anisotropic plasma etch – also in the UNAXIS Shuttleline ICP-RIE – again in a two-step process. This includes a 35 to 60 second etch with the following parameters: 400 W ICP power, 250 RF power, 25 sccm Ar flow rate, 40 sccm Cl_2 flow rate, and 8 mTorr chamber pressure, immediately followed by a second 3 to 5 minute etch with the following parameters: 700 W ICP power, 100 RF power, 50 sccm O_2 flow rate, and 10 mTorr chamber pressure. These ICP-RIE parameters result in perpendicular etching of diamond structures at a rate of approximately 200 nm/min, and were optimized for smooth, near vertical side walls [137]. The purpose of the initial short Ar/Cl_2 plasma etch was to first remove the blanket titanium charge compensation layer, while the subsequent O_2 plasma transferred the etch mask pattern into the diamond substrate. The diamond is typically etched to a depth between 600 and 1000 nm, depending on the particular structure being fabricated. While not schematically represented in Figure 2.1 (b), the final silica etch mask resulting from exposed HSQ is not limited to solid strip line structures, but may also contain intricate internal features required for fabrication of perforated or slotted diamond nanobeams, limited only by the lithographic process. Such internal features are also transferred into the diamond during this top down etch step, allowing for the fabrication of free-standing nanobeam structures with engineered photonic or phononic bandgaps.

Following the top down plasma etch, the angled-etching step is performed to realize the final free-

standing diamond nanobeam structures. Angled-etching is achieved using the same ICP-RIE parameters as the initial O_2 plasma top down etch, but also includes housing the sample inside a specifically designed aluminum Faraday cage to direct the plasma ions to the substrate surface at the intended angle (refer to next section) [138, 139]. Additionally, 2 sccm of either Cl_2 or Ar gas is bled into the chamber during the angled-etching step. This additional chlorine or argon gas was included in the oxygen plasma diamond etch in order to prevent mask redeposition and subsequent roughening of the suspended features. Throughout the angled-etching step, periodic manual sample rotation (~ 30 s intervals) was implemented to average the effective etch angle across the substrate (discussed in more detail in Section 2.4).

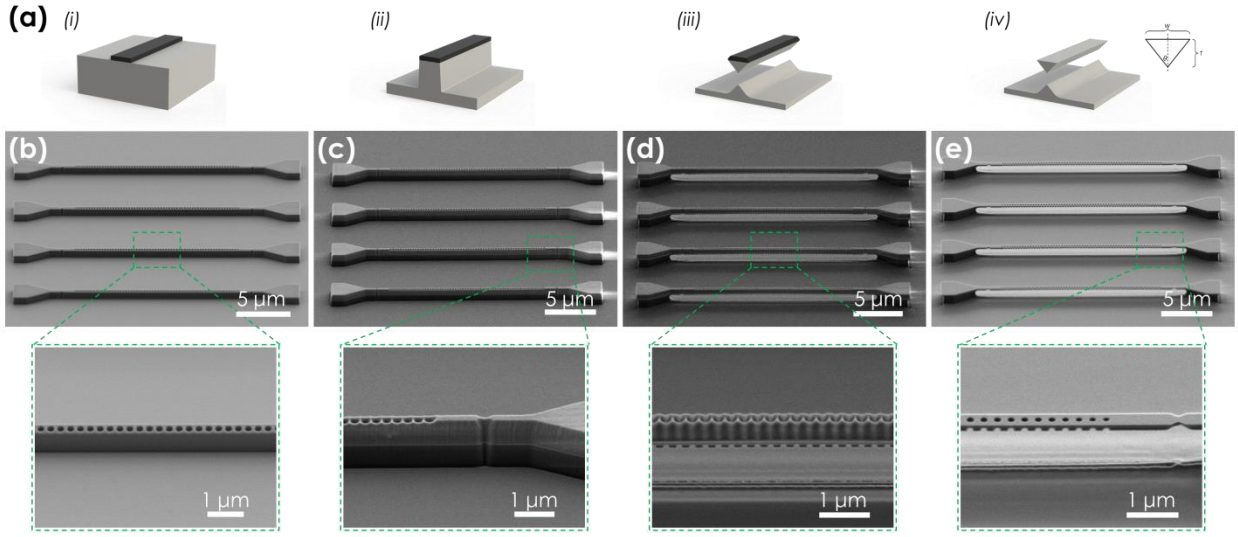

Figure 2.3 | Angled-etching steps with corresponding SEM images. (a) Angled-etching nanofabrication steps with corresponding SEM images: (i) define an etch mask on substrate via standard fabrication techniques (panel **(b)**), (ii) transfer etch mask pattern into the substrate by conventional top down plasma etching (panel **(c)**), (iii) employ angled-etching to realize suspended nanobeam structures (panel **(d)**), (iv) remove residual etch mask (panel **(e)**). All SEM images taken at a stage tilt of 60°.

After angled-etching, the residual etch mask is removed in concentrated hydrofluoric acid. In the case of long suspended diamond nanobeams, critical point drying after removing the etch mask is used. Figure

2.3 illustrates the angled-etching process with corresponding SEM images collected from the same array of diamond nanobeams after each fabrication step. The particular diamond nanobeams shown are perforated structures, where holes in the original silica etch mask resulted in airholes in the final structure. The function of these structures will be described in detail in Chapter 4.

2.2. FARADAY CAGE DESIGNS

As alluded to previously, angled-etching is achieved by housing the diamond substrate within a specifically designed aluminum Faraday cage, which is subsequently placed within the ICP-RIE system. The Faraday cage shields the diamond substrate from the electromagnetic fields which build up inside the ICP-RIE system and are responsible for acceleration of plasma ions towards the sample surface [139]. Although the Faraday cage has small grid openings on its surface, the effect of an external field is drastically attenuated within a small distance of the openings. Thus, during plasma etching, the potential gradient builds up over the face of the Faraday cage and accelerates ions along a path perpendicular to the cage surface. After ions move through the potential gradient and past the metal grid, they are no longer accelerated and travel virtually unimpeded inside the cage towards the substrate. Therefore, with a properly designed Faraday cage geometry, plasma ions may be directed to the sample surface at an oblique angle in multiple directions. It is important to emphasize that while different configurations of Faraday cages can be used, angled-etching is not realized through simple tilting of the substrate within a plasma etcher without a Faraday cage [140].

In our work, Faraday cages consisted of two parts: (1) a structural base machined from aluminum and (2) commercially available wire mesh (also aluminum). The mesh (woven 250 μm diameter wire at a 2 x 2 mm^2 pitch) is bent around the machined structural base and fixed with aluminum bolts, thus forming the

completed Faraday cage. Aluminum is used since is not chemically attacked by oxygen plasma, does not erode at a significant rate during an etching process, and forms only a thin, stable oxide layer.

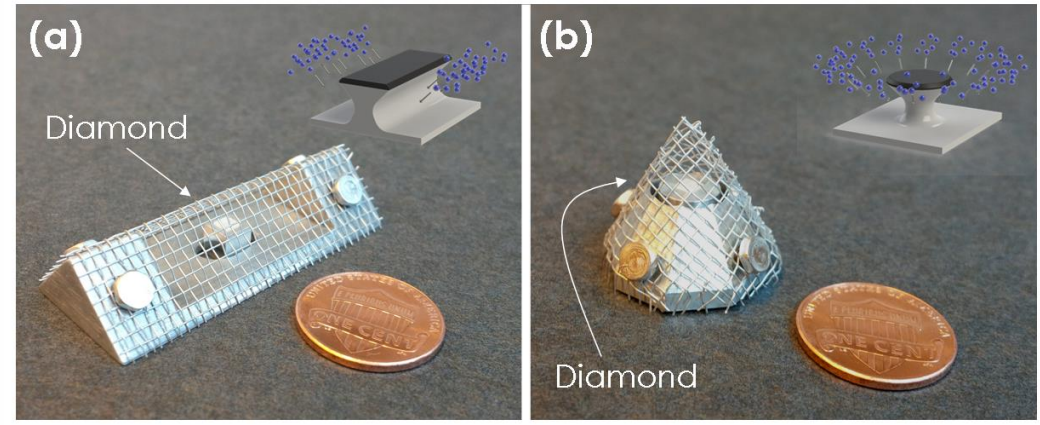

Figure 2.4 | Faraday cage designs. Images of constructed Faraday cage designed used in this work: **(a)** triangular prism Faraday cage with incline angle of θ = 45º, and **(b)** conical Faraday cage with incline angle of θ = 60º. The position of the single-crystal diamond substrate within each Faraday cage is indicated, and insets show models indicating the directions in which angled-etching occurs.

Two specific Faraday cage designs are generally used for angled-etching. The main design constraint for the Faraday cages is the load-lock height clearance of our ICP-RIE system, which is approximately 20 mm. The first Faraday cage design is a triangular prism structure shown in Figure 2.4 (a), which allows for angled-etching in two simultaneous directions (see inset). The ion incidence angle relative to the substrate surface normal (the etch angle, θ) is defined by the incline angle of the Faraday cage. The incline angle of this Faraday cage was θ = 45º, and its height and length were 10 mm and 50 mm respectively. The distance between cage bottom and the surface of the diamond substrate fixed at ~ 3.5 mm using an aluminum sample mounting block. A hole in the bottom of the cage allowed it to be placed over the mounted sample on the ICP-RIE wafer carrier. The second Faraday cage used in this work was a conical design shown in Figure 2.4 (b), where angled-etching occurred in all directions simultaneously

(again, see inset). The conical Faraday cage was constructed in a similar fashion as the triangular prism Faraday cage, and had a bottom diameter of 20 mm with an incline angle of $\theta = 60^{o}$. The diamond substrate surface fixed at a height of ~ 10 mm from the cage bottom in a similar fashion as before.

2.3. PROOF-OF-CONCEPT ANGLED-ETCHING DEMONSTRATION

Figure 2.5 (a) displays scanning electron microscopy (SEM) image of an array of suspended single-crystal diamond nanobeams fabricated by optimized angled-etching techniques with the triangular prism Faraday cage design. The nanobeam structures appear smooth and straight, and are suspended above the diamond substrate with significant clearance (~ 2 μm). A range of nanobeam widths is accessible by angle-etching, from sub-100 nm up to several microns, with long suspended nanobeams (in excess of 100 microns) possible. Figure 2.5 (b) and (c) show SEM images of curved nanobeam waveguides and wheel-and-spoke suspended nanobeam rings fabricated using the conical Faraday cage design, with the same processing conditions as described previously. Since the conical cage enables angled-etching in all directions, suspended nanobeams at arbitrary curvatures are possible.

As a point of reference, Figure 2.6 (a) to (d) display representative SEM images of diamond nanobeams fabricated by angle-etching with parameters which were not yet optimized. In Figure 2.6 (a) and (b), significant micromasking is observed, yielding "grassy" needle-like features. For the fabrication run corresponding to Figure 2.6 (a), the global nature of the observed micromasking was attributed to non-ideal surface preparation. Specifically, without properly cleaning the polished diamond surface in a boiling mixture consisting of equal parts concentrated sulfuric, nitric, and perchloric acid, residual surface contaminants yielded rough grassy texture over the entirety of the sample following angled-etching.

However, once implementing this tri-acid cleaning procedure, these global micromasking features were eliminated.

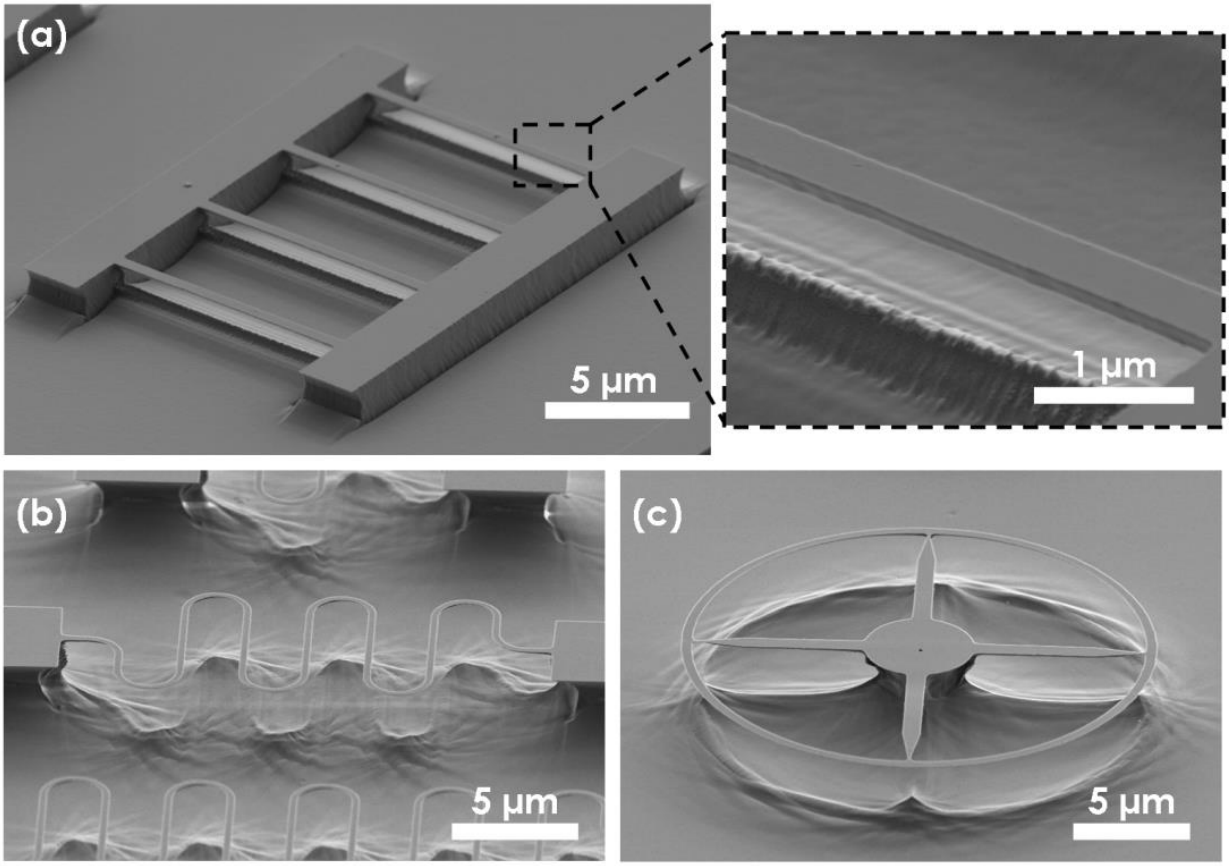

Figure 2.5 | Proof-of-concept diamond nanobeams fabricated by angled-etching. SEM images of **(a)** an array of suspended ~ 500 nm wide solid diamond nanobeams fabricated with a triangular prism Faraday cage. Inset shows a close-up SEM image of the free-standing diamond nanobeam. SEM images of suspended **(b)** ~ 500 nm wide nanobeam wheel-and-spoke ring structure and **(c)** ~ 500 nm wide curved nanobeam, both fabricated with the conical Faraday cage.

Figure 2.6 (b) reveals a fabrication run in which local micromasking was observed in the vicinity of the etched structures. This local variety of micromasking was attributed to erosion of the etch mask during the angled-etching step. Since our angled-etching occurs in multiple directions simultaneously,

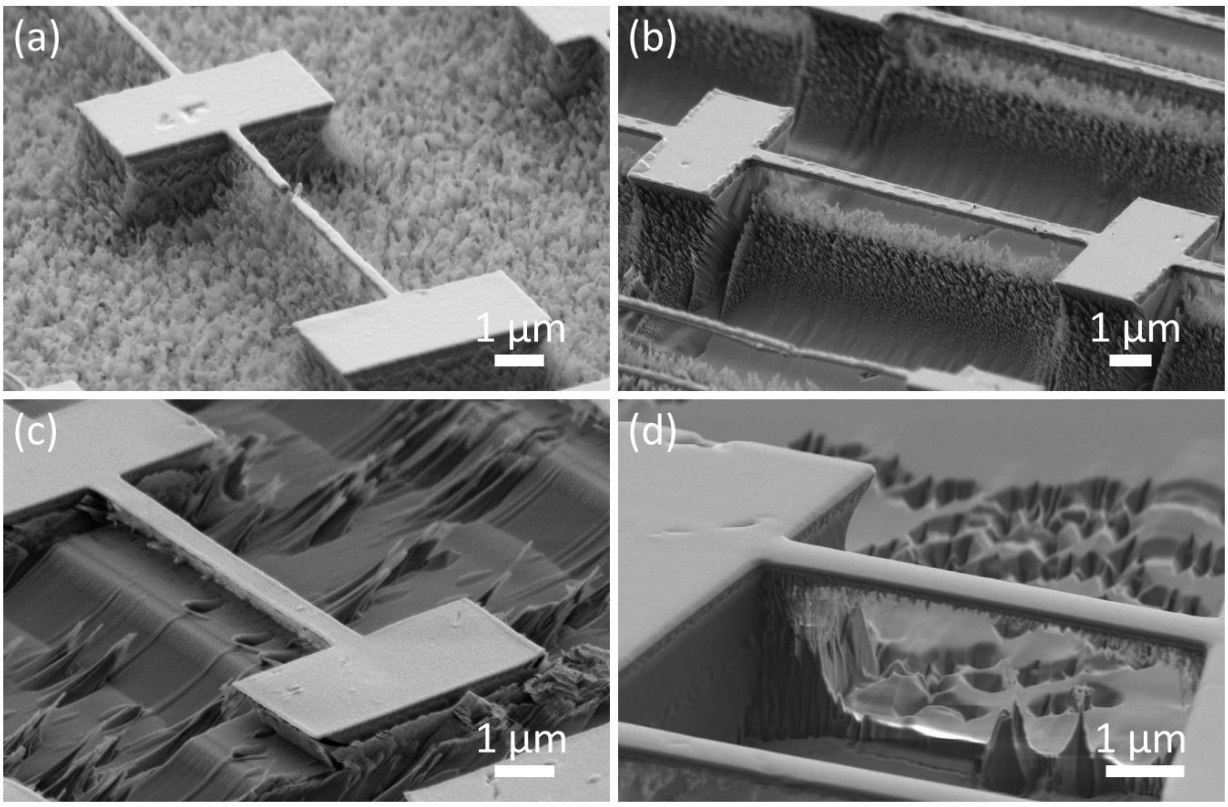

Figure 2.6 | Angled-etching with non-optimized parameters. SEM images of diamond nanobeams fabricated by angled-etching with various non-optimized parameters. **(a)** Global micromasking is observed and attributed to improper surface preparation and cleaning. **(b)** Local micromasking is observed and attributed to mask erosion in the vicinity of the etched structures. **(c)** and **(d)** display fabricated nanobeams with a non-optimized etch angle and a non-ideal etch mask preparation.

small clusters of the etch mask which erode from the patterned structures are in the direct line of incident plasma ions from other directions. With an etch mask of even moderate selectivity, these clusters yield rough, needle-like features on the etching faces of the structure, making it difficult to fully clear the diamond nanobeams. In fact, for the diamond nanobeam shown in Figure 2.6 (b), excessive etch times were necessary to achieve the clearance observed. To circumvent this local micromasking effect, it was necessary to bleed a small amount of gas which would reduce the selectivity of the etch mask into the plasma etch. For the final optimized parameters, 2 sccm of either Cl or Ar was introduced with the 50

sccm of O_2 during the angled-etching plasma etch. It is believed that this trace amount of gas removed any eroded mask clusters from the etching surfaces throughout the course of the angled-etching step, eliminating the formation of needle-like grassy features.

Finally, Figure 2.6 (c) and (d) display the result of fabrication runs which had a non-optimized etch angle and improper etch mask preparation, respectively. In Figure 2.6 (c), the prescribed etch angle was quite steep, and the final diamond nanobeam was not sufficiently cleared. This was resolved in later fabrication attempts by introducing the initial top down plasma etch to provide adequate clearance of the diamond nanobeam, prior to the actual angled-etching step. In Figure 2.6 (d), the preparation of the etch mask was non-ideal, yielding etch mask residue in the local vicinity of the nanobeam feature. As a result, a significant amount of surface roughness on the final suspended structure was observed.

2.4. POST-FABRICATION DEVICE INSPECTIONS

To characterize the etch angle of the fabricated structures, suspended nanobeams were cross-sectioned by FIB-milling. Prior to milling, the diamond nanobeams were sputter coated with ~ 150 nm of gold, which provides charge compensation during FIB exposure. FIB cross-sections also require coating a section of the nanobeam in a thick layer of platinum using ion beam-assisted deposition. A 30 kV Ga^+ ion beam was then used to mill away the platinum and gold coated diamond, exposing the triangular cross-section for SEM imaging. Figure 2.7 (a) and (b) shows representative FIB milled cross-sections of diamond nanobeams fabricated with triangular prism and conical Faraday cage designs respectively.

The corresponding etch angles were measured to be approximately 35^o and 50^o. A ~ 10^o deviation from target etch angle is observed for both Faraday cage designs and attributed to several factors, including the non-ideal verticality of the O_2 plasma etch conditions for single-crystal diamond, and also a

dependence of etch angle on sample height observed within the Faraday cage (i.e. samples near the bottom of the cage etch at slightly steeper angles due to the plasma parameters and small Faraday cage size). From the cross-sections, the diamond nanobeams also appear slightly asymmetric, though it is difficult to quantitatively characterize the cross-sectional symmetry by FIB-milling alone.

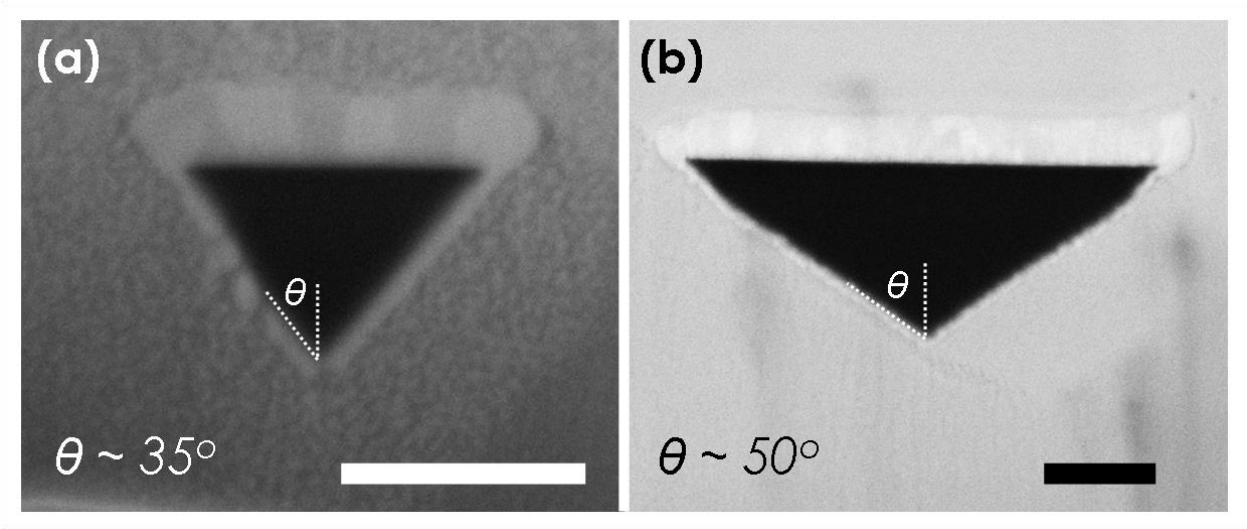

Figure 2.7 | FIB-milled diamond nanobeam cross-sections. SEM images of FIB cross-sectioned diamond nanobeams fabricated with etch angles of **(a)** ~ 35°, and **(b)** ~ 50°. The designated "etch angle" is depicted on the images. Scale bars correspond to 200 nm. All SEM images were taken at a 60° stage tilt.

In typical post-fabrication SEM analysis of free-standing diamond nanobeams, the angled-etched surfaces are mostly hidden from view; even at large stage tilts (for instance, see the inset of Figure 2.5 (a)). As well, given the insulating nature of diamond, high resolution SEM becomes problematic due to charging effects, despite operation at low acceleration voltages. To circumvent this problem, we developed a stamping technique to liberate angled-etch diamond nanobeams from their bulk diamond substrate onto a smooth silver thin film supported by a silicon wafer. While this technique is ultimately destructive, it ensures that many diamond nanobeams are removed from the sample and transferred to a conductive substrate, with most ending up on their back side such that the angled-etched surfaces are

revealed. Since many diamond nanobeams are transferred at once, it also enables ensemble characterization, which allows for concrete conclusions regarding the fabrication process to be made. In this technique, a silver thin film (~ 100 nm thick) is first deposited onto a clean silicon wafer by electron beam evaporation. No specific adhesion layer is used in this deposition step. A second cleaned silicon wafer is then spin coated with a thermally curable epoxy. The epoxy coated silicon wafer is cleaved into reasonably sized chips (~ 1 cm^2), which are then flipped over and pressed onto the silver coated silicon wafer. The epoxy coated silicon chips are then removed carefully by tweezers, with the silver film adhered to the epoxy and peeled cleanly off the original silicon wafer. This silver thin film transfer enables a very smooth film surface over large areas, which is essential for contacting the diamond nanobeams with sufficient van der Waals interaction to break them off of their supporting diamond substrate. After preparation of the conductive silver films, the diamond substrate containing nanobeams to be inspected is flipped upside down on the silver coated substrate and pressed down with moderate force (i.e. several taps with a pair of tweezers). This forces the diamond nanobeams to contact the silver film and break off from their original substrate.

Figure 2.8 (a) to (e) shows a series of high-resolution SEM images taken of perforated diamond nanobeams transferred onto silver substrates. The smooth and polycrystalline nature of the silver thin film is immediately apparent in the SEM images. Moreover, the roughness on the angled-etched surfaces exhibit an interesting bimodal character (refer to Figure 2.8 (b) and (c)), with an extremely rough region localized to the upper portion of the angled-etched surface adjacent to the top side of the diamond nanobeam. In the lower portion of the angled-etched surfaces, a very smooth surface is apparent, and any roughness is not directly visible with the resolution of the SEM. This bimodal character in the surface roughness of the angled-etched sides is quite unique, and its origins are not presently understood. However, current knowledge suggests the greater degree of roughness near the upper half of the angled-etched surface results from micro-masking during fabrication. It is likely that as the angled-etching takes place, small clusters erode from the silica etch mask and are driven towards the opposite face of the

etching diamond nanobeam. As this happens, incident ions from the opposite direction are also etching the structure, and encountering this flux of eroding silica clusters. Since silica is ultimately a good masking material, the small silica clusters are in all likelihood micromasking the upper half of the angled-etch surface, resulting in the significant surface roughness.

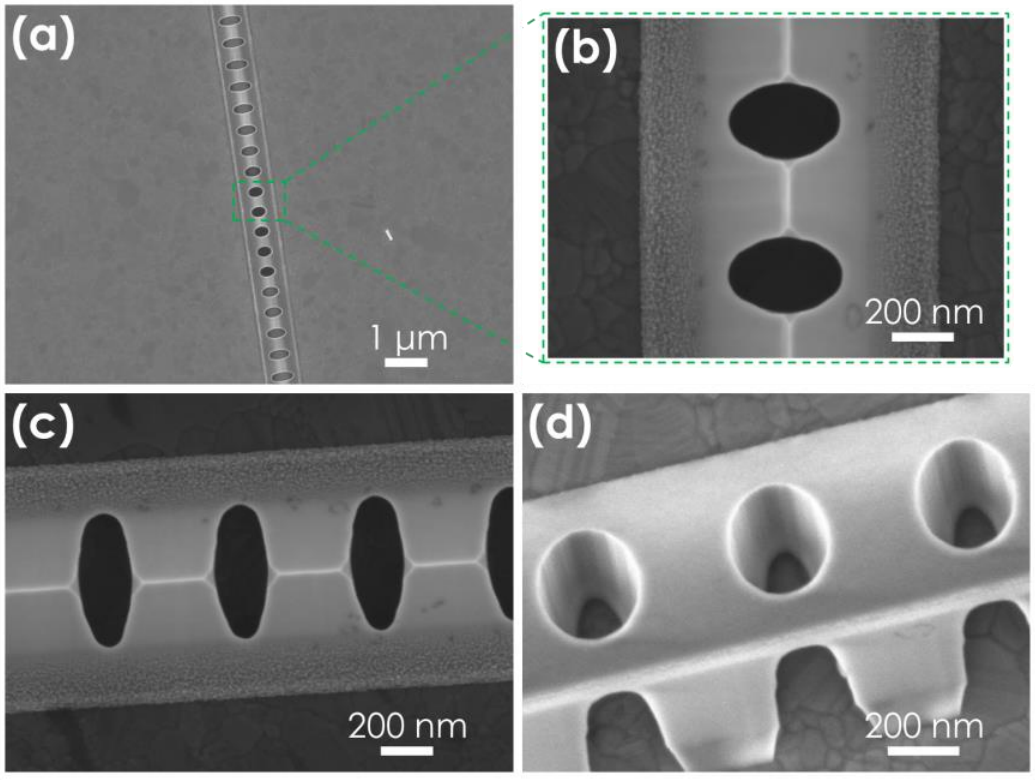

Figure 2.8 | High resolution SEM images of devices post-fabrication. (a) SEM image of an individual diamond nanobeam liberated from its original bulk diamond substrate and adhered to a silver coated silicon chip. **(b,c)** High resolution SEM images of the angled-etched surfaces of the diamond nanobeam, revealing a bimodal character in the surface roughness. **(d)** SEM image of a liberated diamond nanobeam which is laying on one of its angled-etched surfaces, revealing the smooth nature of the interior air hole surfaces.

While most diamond nanobeams are directly transferred to the silver film and appear upside down, some diamond nanobeams break off and land on one of their angled-etch sides. This prospective allows

for inspection of surface roughness on the air holes interior, a location inaccessible by other imaging methods such as atomic force microscopy. In Figure 2.8 (d), the SEM image reveals that the interior of the air holes is quite smooth, without noticeable striations resulting from any micromasking during the initial top down etch. A similar style of bimodal surface roughness like that found on the angled-etched surface is not apparent on the interior of the air holes, which is expected since the air holes are only defined by the initial top down oxygen plasma etch, and are protected during angled-etching by shadowing from the silica etch mask. Additionally, the air holes appear round and symmetrical, a further indication of optimized lithographic parameters.

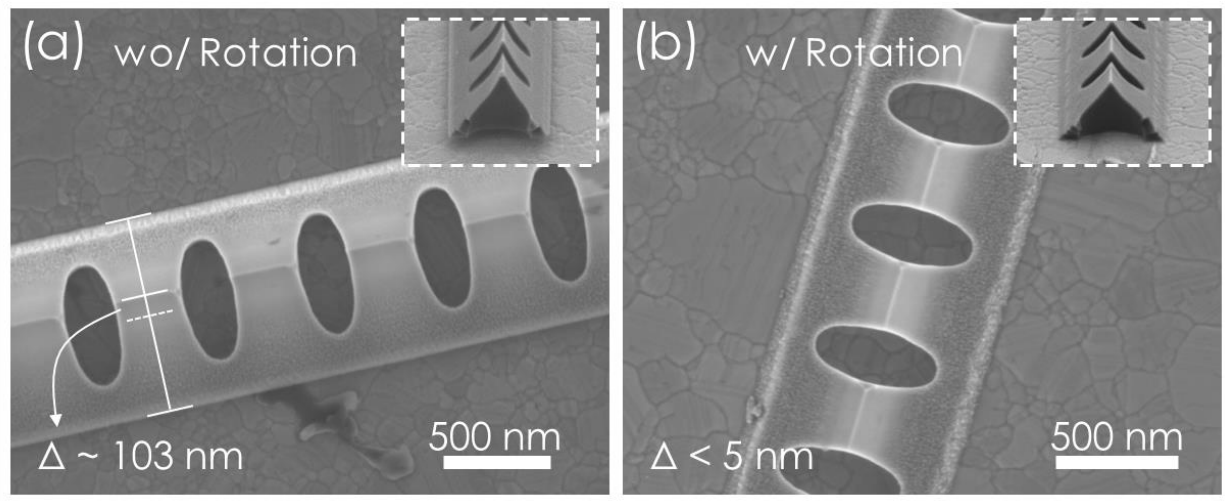

Figure 2.9 | Angled-etched diamond nanobeam cross-sectional symmetry. High resolution SEM images of the backside of diamond nanobeams fabricated by angled-etching **(a)** without and **(b)** with sample rotation during angled-etching. A significant improvement in the cross-section asymmetry (Δ) is observed. Insets tilted SEM images of broken diamond nanobeams, revealing the diamond nanobeam cross-section.

Evidently, a unique consideration of angled-etched diamond nanobeam structures is their triangular cross-section symmetry. For instance, uneven sample mounting during the angled-etching step or diamond substrate wedge tolerances will lead to a distribution of effective etch angles across the sample,

breaking symmetry in the final device cross-section. To circumvent this, periodic sample rotation was implemented during angled-etching to average the effective etch angle across the substrate. High-resolution SEM images shown in Figure 2.9 (a) and (b), respectively, reveal perforated diamond nanobeams (oriented upside down) fabricated without and with sample rotation during angled-etching, with insets displaying a tilted cross-sectional view. Sample rotation appears to reduce the degree of asymmetry (defined as the offset in the bottom apex of the triangular cross-section from its centerline) considerably.

Further device inspection via transmission electron microscopy were also conducted, and discussed in the Appendix.

Chapter 3

Nanomechanical resonant structures in single-crystal diamond

In the past, fabrication of single-crystal diamond nanomechanical systems has mainly utilized crystal ion slicing [109, 110], where irradiation of a single-crystal diamond substrate with energetic ions creates a sub-surface graphitized layer which can be selectively removed. However, residual crystal damage and large film stresses resulting from ion implantation significantly reduces final device quality [109-112]. Recently, micron-scale single-crystal diamond cantilevers [80, 119] – exhibiting mechanical Q-factors > 10^5 – were fabricated via a DOI platform [69, 120-122], created by thinning diamond slabs adhered to a supporting substrate. Though this approach remains promising, without heteroepitaxially grown thin films, further development of truly nanoscale mechanical systems in single-crystal diamond requires exploring alternative device fabrication avenues. In this chapter, the characterization of fabricated diamond nanomechanical resonators is described in Section 3.1. The nanomechanical properties of doubly clamped nanobeam resonators are presented in Section 3.2, and Section 3.3 discusses the characterization of diamond nanobeam cantilevers.

3.1 CHARACTERIZATION OF DIAMOND NANOMECHANICAL RESONATORS

Figure 3.1 displays SEM images of fabricated diamond nanobeam mechanical resonators. Free-

standing nanobeams were 10 to 85 μm long, with widths between 500 nm and 1.3 μm. Optical grade, <100>-oriented, single-crystal diamonds (< 1 ppm [N], Element Six) were used throughout this work. In general, angled-etching fabrication offers excellent yield (> 95%) and throughput (> 10^3 devices/mm^2), with over 500 devices measured in this work. Nanobeams shown in Figure 3.1 (a) and (b), which are doubly clamped nanomechanical resonators, are suspended above the diamond substrate with significant clearance (~ 1.5 μm). As displayed in Figure 3.1 (c), focused ion beam (FIB) milled cross-sections revealed a symmetric triangular shape, with a bottom apex half-angle of $\theta \sim 50^o$. Figure 3.1 (d) and (e) show images of as-fabricated single-crystal diamond nanobeam cantilevers, which displayed identical substrate clearance and cross-section to doubly clamped nanobeams.

Diamond nanobeam Brownian motion was characterized via optical interferometric displacement detection, employing a focused laser at normal incidence to the substrate [141, 142]. In this detection scheme, interference between light confined within the nanobeam and the standing light wave – which originates from the incident laser interfering with light reflected from the substrate – provided ample displacement sensitivity to out-of-plane motion. Additionally, optical characterization of nanobeam resonators in a similar configuration has previously been shown to provide comparable sensitivity to in-plane resonator motion [143]. The characterization set up, shown schematically in Figure 3.1 (f), employed a tunable telecom laser (Santec TSL-510) focused by an objective (NA = 0.5), through a vacuum chamber view port, on the diamond nanobeams. Individual nanobeams were positioned under the focused laser spot using motorized stages. Light reflected from the sample was collected by a photodetector (New Focus model 1811). A spectrum analyzer (Tektronix RSA3303B) at the photodetector output revealed mechanical resonances. All measurements were conducted at ~ 10^{-6} Torr and room temperature.

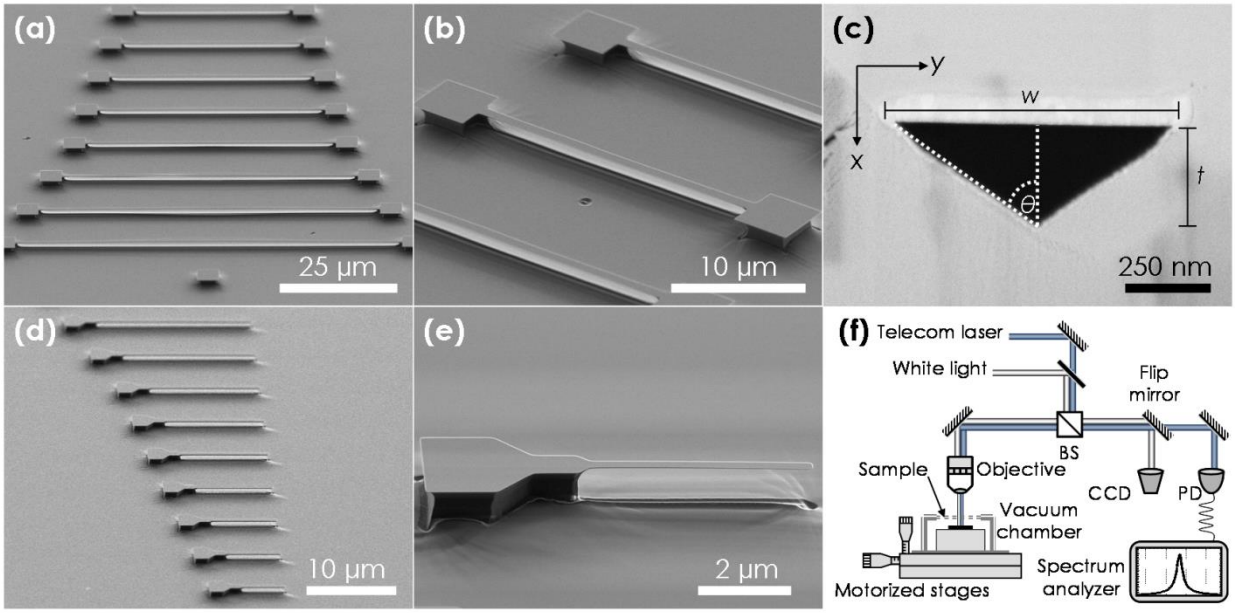

Figure 3.1 | Fabricated diamond nanobeam mechanical resonators. (a) SEM image of an array of freestanding doubly clamped single-crystal diamond nanobeams. **(b)** SEM image and **(c)** corresponding FIB cross-section of an individual as-fabricated ~ 675 nm wide diamond nanobeam. SEM images of **(d)** an array of freestanding single-crystal diamond cantilevers and (e) an individual as-fabricated ~ 675 nm wide diamond cantilever. All SEM images taken at a 60° stage tilt. **(f)** Schematic of the optical characterization setup.

3.2 DOUBLY CLAMPED DIAMOND NANOBEAMS

The transverse vibrations of rigid nanobeams are described by Euler-Bernoulli theory [144], which yields a relationship for nanobeam resonance frequency that is inversely proportional the length squared and directly proportional to the width. Since the diamond nanobeam cross-section is not axially symmetric, out-of-plane and in-plane bending moments are $I_x = wt^3/36$ and $I_y = w^3t/48$, respectively. As such, the geometry dependent resonance frequencies (f_n) are:

$$f_{x,n} = \frac{1}{(2\pi)} \frac{k_n^{\,2}}{l^2} \sqrt{\frac{Et^2}{18\rho}} \tag{3.1}$$

and

$$f_{y,n} = \frac{1}{(2\pi)} \frac{k_n^{\,2}}{l^2} \sqrt{\frac{Ew^2}{24\rho}} \tag{3.2}$$

where E is the Young' modulus, ρ is the material density, and l is the nanobeam length. The parameter k_n is a mode index, which is determined from boundary conditions associated with the specific type of nanobeam resonator [144]. From the triangular nanobeam cross-section in Figure 3.1 (c), Eq. (3.1) and Eq. (3.2) indicate the same order out-of-plane vibrations occur at lower frequencies than in-plane resonances.

Figure 3.2 (a) displays a thermomechanical power spectral density (PSD) collected from a 675 nm wide, 55 μm long doubly clamped diamond nanobeam. High-resolution thermal noise spectra of the observed resonances are displayed as insets. Since diamond nanobeams are not externally actuated, the voltage spectral density of the thermal fluctuations, $S_v^{1/2}$ (μV/Hz$^{1/2}$), may be converted to a displacement spectral density, $S_z^{1/2}$ (pm/Hz$^{1/2}$), via equipartition theorem [145]. To do so, the spring constant of each mode was determined via finite element method (FEM) simulations (COMSOL Multiphysics). Thermomechanical calibration of doubly clamped diamond nanobeams took into account the built up compressive stress determined through FEM fits to the frequency versus length plots in Figures 3.2 (b) and (c), as will be discussed shortly. Fitting to calibrated thermomechanical spectra gave the resonance frequency, mechanical Q-factor, conversion from voltage to displacement, and displacement noise floor.

The mechanical Q-factors are approximately 9,400, 10,900, and 19,000 for the three mechanical modes, respectively.

Mechanical resonance frequencies measured from ~ 565 and 675 nm wide doubly clamped nanobeams are plotted in Figure 3.2 (b) and (c) as a function of length. Here, only the first three observed resonance frequencies are plotted. Although the higher-frequency resonances appear to follow an inverse power law relationship with length, the lowest frequency mode displays a complicated behavior, not following trends predicted by Euler-Bernoulli theory. Such a discrepancy between theory and experiment is a strong indication the diamond nanobeams are compressively stressed [146, 147], which modifies the expected resonance frequencies as:

$$f_n(\sigma) = f_n \sqrt{1 - \frac{\sigma A l^2}{k_n{}^2 EI}} \tag{3.3}$$

where σ is the magnitude of uniaxial compressive stress along the length of the beam and A is the cross-sectional area. As such, compressive stress lowers the resonance frequency, with the term under the square root in Eq. (3.3) vanishing when the stress approaches the critical Euler buckling load σ_c, which for a doubly clamped beam, is defined as:

$$\sigma_c = \frac{\pi^2 EI}{(0.5l)^2 A} \tag{3.4}$$

In the context of Figure 3.2 (b) and (c), Eqs. (3.3) and (3.4) may be alternatively viewed in terms of a critical buckling length, l_c, given a built-in compressive stress. Previous reports noted that experimental resonance frequencies of polycrystalline silicon resonators were strikingly different for beams longer than the critical-buckling length dictated by a built-in compressive film stress [147], while shorter nanobeams were well approximated by Eq. (3.3). Similar observations are made here in Figure 3.2 (b), where the first experimental resonance mode of 565 nm wide nanobeams reaches a minimum near $l \sim 25$ μm, beyond which the resonance frequencies increase and level off until $l \sim 40$ μm. Away from this point, resonance frequencies eventually recover an inverse-power-law relationship. The local minimum near $l \sim 25$ μm represents the transition from a compressively-stressed, unbuckled nanobeam to a buckled nanobeam (i.e. critical buckling length). The increase in resonance frequency for lengths slightly greater than 25 μm is likely due to the significant release of compressive stress through buckling deformation, while nanobeams much longer than 25 μm will recover the frequency-versus-length trend predicted by Euler-Bernoulli theory. A similar trend, though less pronounced, is observed in Figure 3.2 (c) for 675 nm wide diamond nanobeams, with a minimum in the first experimental resonance now near $l \sim 40$ μm.

FEM simulations were employed to fit the experimental data in Figure 3.2 (b) and (c), as shown by dashed lines. Built-in compressive stress was applied by gradually increasing the initial material strain. By employing non-linear solvers and this monotonically increasing parameter, the software is able to avoid the bifurcation in solutions normally associated with the buckling of a rigid beam and calculate the final deformed shape for a given compressive stress. A non-linear eigenfrequency solver is then used to calculate the mechanical modes of the resulting stressed and deformed structures. Their simulated flexural shape allowed discrimination between in-plane and out-of-plane vibrations, as well as determining the mode order by the number of anti-nodes. The simulations show excellent agreement with experimental data for all three plotted modes, and interestingly, also predict a spectral crossing of the first and second resonance mode shapes. It is important to note the fitting parameters employed in the simulations (initial

material strain and Young's modulus) were extremely sensitive to the experimental data near and to the left of the buckling transitions.

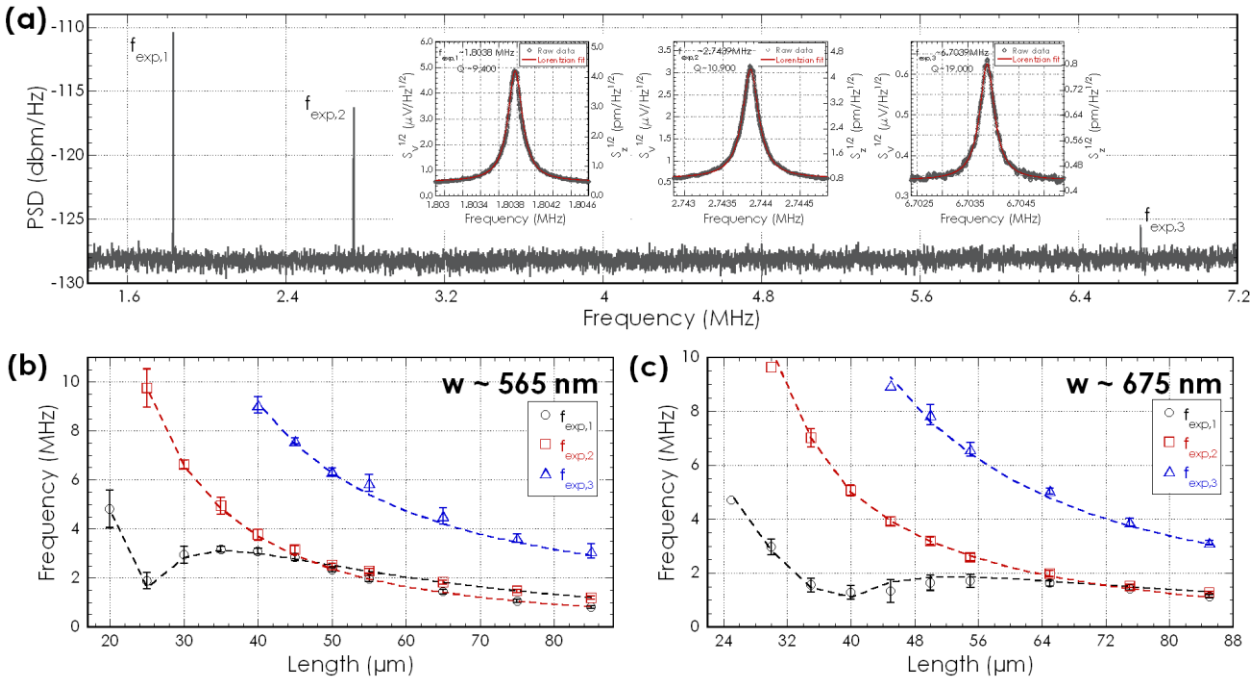

Figure 3.2 | Nanomechanical properties of doubly clamped diamond nanobeams. (a) Representative thermomechanical power spectral density of a ~ 675 nm wide and 55 μm long doubly clamped diamond nanobeam revealing three resonance peaks, with corresponding high-resolution thermally calibrated noise spectra of the first, second, and third resonance modes shown as insets. Experimentally measured mechanical resonance frequencies of **(b)** ~ 565 nm wide and **(c)** ~ 675 nm wide doubly clamped diamond nanobeams, plotted as a function of nanobeam length. Dashed lines correspond to FEM simulations, with the local minimums in **(b)** and **(c)** representing the transition from a compressively-stressed, unbuckled nanobeam to a buckled nanobeam.

From simulation, the estimated built-in compressive stress was ~ 140 MPa, assuming a diamond Young's modulus of roughly 900 GPa. Origins of compressive stress in fabricated nanobeams are not entirely clear, especially since the nanostructures are fabricated from a bulk crystal, making interfacial stresses unlikely. Presumably, stress may have originated from the etch mask used during fabrication,

though further investigation of stress in diamond nanobeams is beyond the scope of the present study. Knowledge of built-in stress in angled-etched nanobeams – in the context of diamond nanomechanics with integrated NV^-, or other color centers, is particularly important since spectral properties of diamond color centers are impacted by both local and global lattice perturbations.

3.3 DIAMOND NANOBEAM CANTILEVERS

Ultimately, the potentially adverse effects of compressive stress on resonance frequency and mechanical Q-factor are circumvented in nanobeam cantilevers, where axial stress is released by the free-ended structure. Figure 11 (a) displays a thermomechanical power spectral density for an 880 nm wide, 20 μm long cantilever. Two resonance peaks are revealed, with lower and higher frequencies now – by Euler-Bernoulli theory – attributed to out-of-plane and in-plane flexural modes, respectively. By Eq. (3.1) and Eq. (3.2), the ratio of the same order in-plane to out-of-plane resonance frequencies reflects the etch angle through:

$$\theta = \tan^{-1}\left(\frac{f_{y,n}}{\sqrt{3} f_{x,n}}\right) \tag{3.5}$$

Applying this relation to the experimental data gave an etch angle of $53.5^o \pm 2^o$, which is an ensemble estimate and in close agreement with that obtained from FIB cross-sections. Measured out-of-plane cantilever resonances are plotted in Figure 3.3 (b). Here, the expected $f \propto l^2$ trend is clear. Dashed lines in Figure 3.3 (b) are calculated with Eq. (3.1), using appropriate beam geometries and ρ = 3500 kg/m^3.

From the fits, the Young's modulus was estimated to be ~ 901 ± 58 GPa. This low modulus value for single-crystal diamond is likely due to the high level of nitrogen doping in the substrates. We note that diamond nanomechanics from single-crystal substrates developed here enables investigation of resulting material properties and processes latitude for synthetic diamond growth in a chip-scale manner, as has previously been done with silicon-based substrates and thin films [147-149].

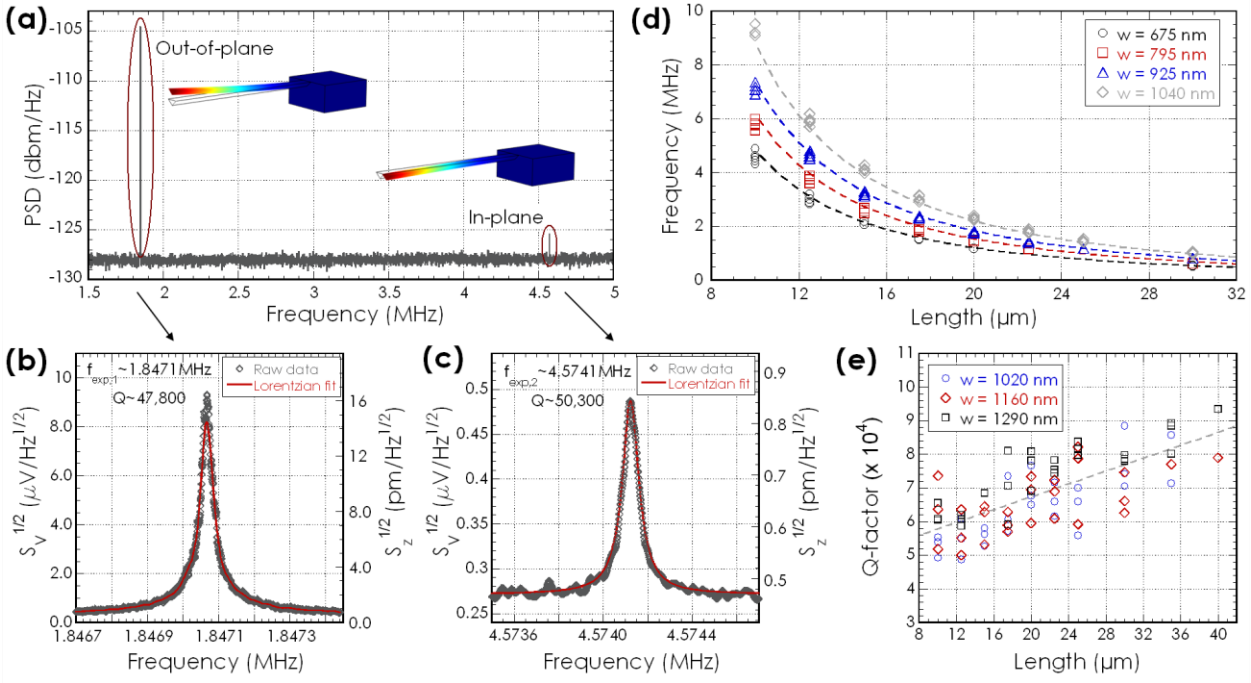

Figure 3.3 | Nanomechanical properties of diamond nanobeam cantilevers. **(a)** Representative thermomechanical power spectral density of an 880 nm wide and 20 μm long diamond nanobeam cantilever revealing out-of-plane (lower frequency) and in-plane (higher frequency) resonance peaks (shown as insets), with corresponding high-resolution thermally calibrated noise spectra of the **(b)** out-of-plane and **(c)** in-plane resonance modes. **(d)** Mechanical resonance frequencies and **(e)** Q-factors estimated from fundamental out-of-plane resonance modes of diamond cantilevers plotted as a function of nanobeam length, with the dashed line given as a guide for the eye.

High-resolution thermal noise spectra of the out-of-plane and in-plane resonance peaks displayed in

Figure 3.3 (a) are shown in Figures 3.3 (c) and (d), respectively. Again, thermomechanical calibration is carried out on the acquired spectra. The mechanical Q-factors, estimated from FWHM of the peaks, are approximately 47,800 and 50,800 for the two modes, respectively. The highest measured Q-factor in the range of fabricated cantilevers was ~ 94,000. Q-factors estimated for fundamental out-of-plane diamond cantilevers resonances are plotted in Figure 3.3 (e), with the dashed line as a guide for the eye. From Figure 3.3 (e), the mechanical dissipation displays a limited dependence on length, though higher Q-factors for longer nanobeams are apparent. This likely suggests diamond cantilevers are limited by clamping losses, and longer devices would likely increase mechanical Q-factor [150-152].

Chapter 4

Nanophotonic devices in single-crystal diamond

In this chapter we demonstrate state-of-the art nanophotonic resonators in bulk single-crystal diamond substrates, fabricated by angled-etching. Our devices feature large optical Q-factors, in excess of 10^5, and operate over a wide wavelength range, spanning visible (400 nm to 800 nm) and telecom (1.3 μm and 1.55 μm). In section 4.1, we present one dimensional photonic crystal cavities (referred hereafter as "nanobeam cavities") operating at telecom wavelengths. These nanobeam cavities feature Q-factors on par with those typically found in devices fabricated in standard photonic materials, by conventional means. Considering their wavelength scale mode volume ($V \sim (\lambda/n)^3$), diamond nanobeam cavities reported here feature the highest Q/V figure of merit demonstrated in single-crystal diamond to date [16].

In section 4.2, we demonstrate low optical loss free-standing waveguides carved from a bulk diamond crystal, realized using novel tapered vertical support structures. Free-standing looped-waveguide racetrack resonators, fabricated by angled-etching, are shown to support high-Q resonances in the telecom band. Fabrication and characterization of diamond nanobeam cavities and racetrack resonators operating at visible wavelengths is presented in Section 4.3. These newly developed high-Q diamond optical nanocavities open the door for a wealth of applications, ranging from nonlinear optics and chemical sensing, to quantum information processing and cavity optomechanics. Finally, in Section 4.4 we realize on-chip nanophotonic networks in bulk single-crystal diamond, and demonstrate a high efficiency (> 90 % power coupling) fiber-optical interface with aforementioned on-chip diamond nanophotonic devices.

4.1 DIAMOND NANOBEAM CAVITIES AT TELECOM WAVELENGTHS

Following the demonstration of free-standing diamond nanobeams starting from a bulk single-crystal (described Chapter 2), the necessary refractive index contrast now exists to realize engineered diamond nanophotonic structures. Therefore, we demonstrate diamond photonic crystal nanobeam cavities using our angled-etching approach [130]. These devices consist of a waveguide perforated with a chirped lattice of elliptically-shaped air holes, resulting in a photonic bandgap structure, which has been engineered to support localized resonances with ultra-high Q-factors and ultra-small mode volumes [99]. Figures 4.1 (a) to (c) display a representative single-crystal diamond nanobeam cavity fabricated with etch angle $\theta \sim 35^{o}$ for operation in the telecom band.

Since the nanobeam thickness and width are linked through angled-etching, global scaling of the nanobeam cavity dimensions results in tuning of the cavity resonance while maintaining all cavity figures of merit (i.e. Q-factor and mode volume). Therefore, the nanobeam cavity design used in this work is parameterized by the target fundamental transverse electric (TE-like) cavity mode resonance wavelength, λ_{TE}. Note, more detailed description of diamond nanobeam cavities designs described in this chapter are given in Appendix B.

Our design – based on previously developed design principles [153, 154] – has the following parameters: a nanobeam width $w = 0.58\lambda_{TE}$, lattice constant (hole spacing) $a = 0.319\lambda_{TE}$, and elliptical hole minor radius $r = 0.087\lambda_{TE}$. Furthermore, to minimize the scattering and maximize the cavity Q, the major radius of the elliptical hole array is decreased quadratically, over 31 periods, from $r_1 = 0.145\lambda_{TE}$ at the center of the cavity, to $r_{31} = 0.087\lambda_{TE}$ at its end. We modeled the devices using finite-difference time-domain (FDTD, Lumerical Solutions Inc.) methods, and found they support both transverse magnetic

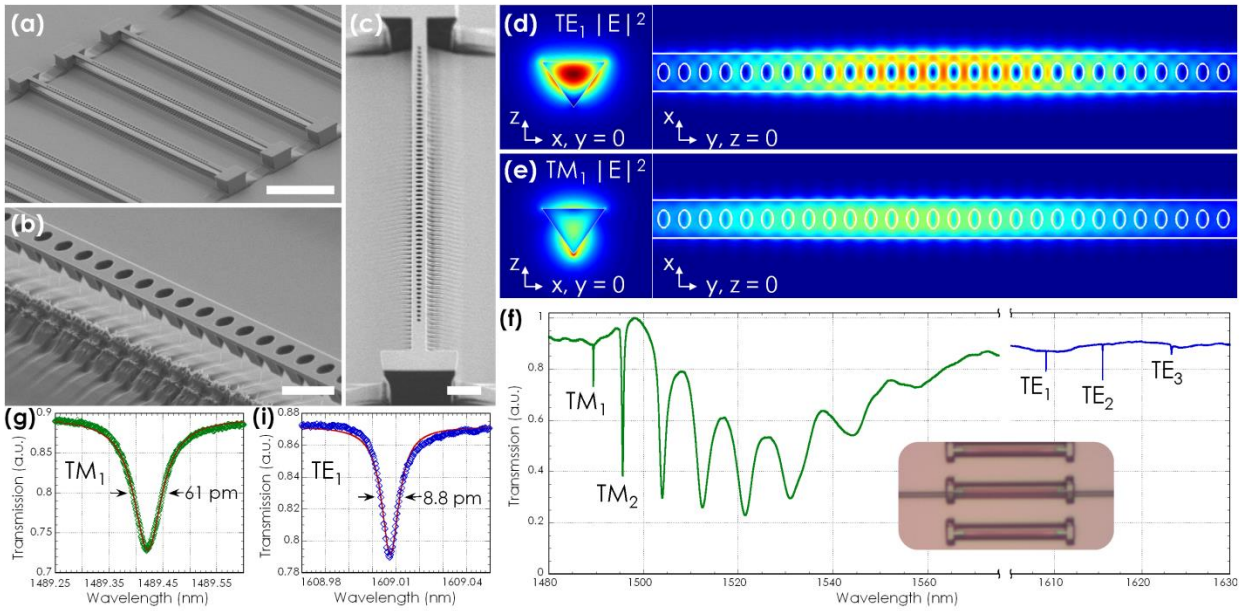

Figure 4.1 | High-Q diamond nanobeam photonic crystal cavities. Scanning electron microscope (SEM) images of **(a)** diamond nanobeam photonic crystal cavities, with close-up **(b)** prospective and **(c)** top down views. Note, a ~ 35° etch angle was used to fabricate devices shown. Scale bars for SEM images in **(a)**, **(b),** and **(c)** correspond to 10 μm, 1 μm, and 2 μm respectively. All SEM images were taken at a 60° stage tilt. Simulated cross-sectional and top down electric field intensity profiles of the fundamental quasi- **(d)** transverse electric (TE-like) and **(e)** transverse magnetic (TM-like) nanobeam photonic crystal cavity modes. Note, top down mode profiles correspond to top face of the nanobeam cavity. Theoretical figures of merit for the fundamental nanobeam photonic crystal cavity modes are Q-factors of $Q_{TM} \sim 1.3\text{x}10^5$ and $Q_{TE} \sim 3.0\text{x}10^6$, with mode volumes $V_{TM} \sim 2.55(\lambda/n)^3$ and $V_{TE} \sim 2.26(\lambda/n)^3$, (the subscript refers to the cavity mode transverse polarization). **(f)** Representative normalized broadband spectrum of a fabricated diamond photonic crystal cavity collected by fiber taper measurement, with inset optical micrograph indicating the fiber taper coupling position. High resolution spectra of the fundamental **(g)** TM-like and **(h)** TE-like cavity modes, with Lorentzian fits to the data also shown. The taper-loaded Q-factors (extracted from Lorentzian fits to the data) of the fundamental and second order TM-like cavity modes were 24,000 and 3,700 respectively, while the first three TE-like cavity modes had loaded Q-factors of 183,000, 94,000, and 22,000, respectively.

(TM-like) and TE-like resonances (with the fundamental TM-like resonance, λ_{TM}, located at $0.9\lambda_{TE}$), with representative mode profiles shown in Figure 4.1 (d) and (e) respectively. The dual mode nature of the

triangular cross-section nanobeam cavities is of interest for applications in nonlinear optics and wavelength conversion [155-157]. Theoretical figures of merit for the fundamental cavity modes are Q-factors of $Q_{TM} \sim 1.3x10^5$ and $Q_{TE} \sim 3.0x10^6$, with mode volumes $V_{TM} \sim 2.55(\lambda/n)^3$ and $V_{TE} \sim 2.26(\lambda/n)^3$, (the subscript refers to the cavity mode transverse polarization). Additionally, due to the gradual nature of the chirped lattice of air holes, the devices also support higher order longitudinal modes of both polarization. We note that devices shown in Figure 4.1 are based on a design with fundamental cavity resonances located at λ_{TE} = 1680 nm and λ_{TM} = 1507 nm respectively.

A normalized transmission spectrum of a representative diamond nanobeam cavity is shown in Figure 4.1 (f). Transmission measurements in the telecom band were collected via fiber taper coupling [158] to suspended single-crystal diamond nanobeam cavities. Fiber tapers were manufactured from SMF-28 fiber (Corning) by the conventional flame anneal and pulling method [159], resulting in a final diameter of ~ 1 μm. The fiber taper was mounted in a U-shaped configuration, resulting in self-tension of the taper region and allowing it to be position in close proximity to the desired diamond device [160]. Since the diamond nanophotonic devices are positioned above the diamond substrate in excess of 2 microns, dimpling the fiber taper was not necessary. The fiber taper was spliced into an optical set-up, and its position with respect to the device under test was precisely controlled via motorized stages with 50 nm encoder resolution. Two tunable lasers (Santec TSL-510, tuning range from 1480 to 1680 nm) were used, along with an inline fiber polarizer, and high gain InGaAs detector (EO Systems, IGA1.9-010-H) to record transmission spectra. All displayed spectra were normalized by transmission data collected from an uncoupled position.

Two sets of transmission dips are observed, and are attributed to cavity resonances: dips located near 1610 nm correspond to TE-like modes, while those located near 1490 nm correspond to TM-like modes. The experimentally obtained fundamental resonance wavelengths for the two modes indicate $\lambda_{TM,exp} \sim 0.92\lambda_{TE,exp}$, which is in good agreement with FDTD predictions. The absolute values of cavity resonances are blue shifted by roughly 5% from the target values, which is likely due to the uncertainty in the actual

etch angle. The latter was previously estimated to deviate up to 2° degrees from the nominal value [132] (see Chapters 2 and 3). High resolution spectra of fundamental TM-like and TE-like transverse cavity modes are shown in Figure 4.1 (g) and (h) respectively. The loaded Q-factor of the fundamental TE-like cavity mode is remarkably high at $Q_{TE} \sim 183{,}000$ and compares very well to the state-of-the-art silicon photonic crystal nanobeam cavities realized by standard fabrication techniques. We note that the loaded Q-factor of the fundamental TM-like nanobeam cavity is approximately $Q_{TM} \sim 24{,}000$. Nearly an order of magnitude reduction in cavity Q for this mode is likely due to its localization at the bottom apex of the nanobeam, which increases its losses by scattering from overlap with etched surfaces and leakage into the diamond substrate.

4.2 DIAMOND RACETRACK RESONATORS AT TELECOM WAVELENGTHS

Of the myriad of on-chip optical cavities demonstrated to date, ring and racetrack resonators are arguably the most ubiquitous [98]. Conceptually, the optical cavity is a waveguide looped back on itself, and the resonance is formed when the optical path length is an integer multiple of the wavelength. In the context of angled-etching, creating a free-standing looped waveguide represents a challenge, since suspended devices must be supported by at least one physical attachment to the bulk substrate. While free-standing wheel-and-spoke optical cavity structures [161, 162] (as demonstrated in Chapter 2) are an intuitively obvious solution, spoke attachment points to the looped triangular cross-section waveguide are difficult to fabricate, resulting in significant scattering losses. To circumvent this, we have developed novel vertical support structures [163], shown in Figure 4.2 (a) - (c), and used it to realize single-crystal diamond racetrack resonators. This was accomplished by positively tapering the width of the 20 μm long straight portions of the racetrack resonator by 15 % of the nominal value. Note, a ~ 50° etch angle

(designated as the semi angle at the bottom apex of the triangular cross-section) was used to fabricate diamond racetrack resonators shown in Figure 4.2. In angled-etching [130], wider features require more time to be fully released from the substrate. As a consequence, wider sections can remain attached to the substrate resulting in a pedestal-like support at their center. At the same time, the tapered nature of the vertical support structure minimizes optical losses.

A typical normalized transmission spectrum (again collected by fiber taper coupling) from diamond racetrack resonator is shown in Figure 4.2 (f). Two distinct sets of transmission dips are observed, corresponding to fundamental TE-like and TM-like modes of the structure, shown Figure 4.2 (d) and (e), respectively. Nearly critically coupled resonances displayed in Figure 4.2 (g) and (h) reveal loaded Q-factors of $Q_{L,TE} \sim 151{,}000$ and $Q_{L,TM} \sim 113{,}000$, where the subscript indicates the cavity mode transverse polarization. We note that the term loaded Q-factor refers to the Q-factor that includes losses due to fiber taper coupling, and at critical coupling is half the intrinsic Q-factor (i.e., $Q_L = \frac{1}{2}Q_i$). The latter is determined by losses due to scattering, material absorption, leakage to the substrate (if any), and waveguide bends/overlaps. From our measurements, we estimate intrinsic Q-factors to be $Q_{i,TE} \sim 302{,}000$ and $Q_{i,TM} \sim 226{,}000$. From measured Q-factors, an upper limit on the diamond waveguide transmission loss (α) is estimated to be ~ 1.5 dB/cm for both guided modes via the relationship [164]:

$$\alpha \approx \frac{2\pi n_g}{Q_i \lambda} \tag{4.1}$$

where n_g is the mode group index, and λ is the resonant wavelength. While this loss value is roughly five times greater than that recently reported for single-crystal diamond waveguides fabricated via the membrane thinning approach, it is also an order of magnitude smaller than losses of polycrystalline diamond ring resonators also operating at telecom wavelengths [105].

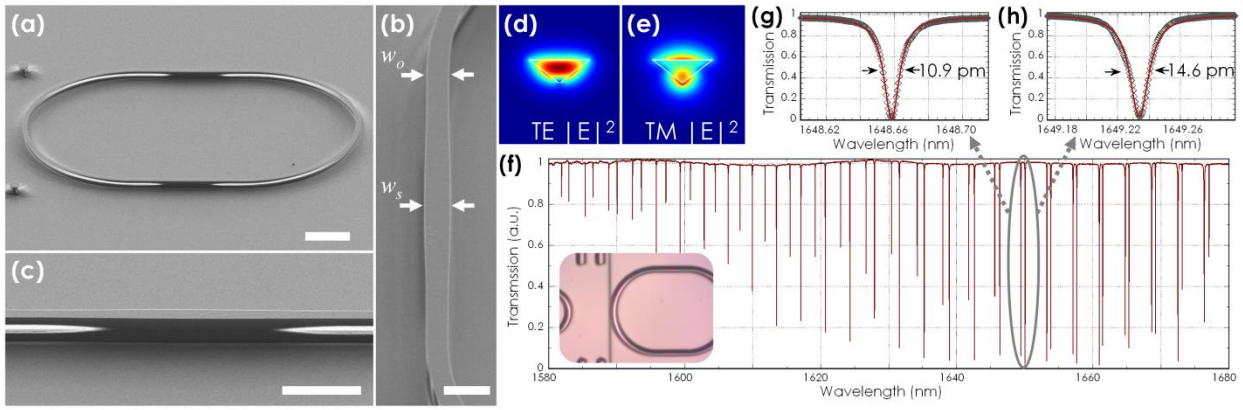

Figure 4.2 | High-Q diamond racetrack resonators. Scanning electron microscope (SEM) images of **(a)** 25 μm bend radius diamond racetrack resonator, with close-up **(b)** side and **(c)** top views. The nominal (w_o) and maximum (w_s) width (indicated on figure) of the tapered vertical are approximately 1.1 μm and 1.27 μm, respectively. Note, a ~ 50^o etch angle was used to fabricate devices shown. Scale bars for SEM images in **(a)**, **(b),** and **(c)** correspond to 10 μm, 5 μm, and 2 μm respectively. All SEM images were taken at a 60^o stage tilt. Simulated quasi- **(d)** transverse electric (TE-like) and **(e)** transverse magnetic (TM-like) mode profiles (λ = 1.55 μm, electric field norm) of a suspended 1.1 μm wide diamond waveguide. **(f)** Representative normalized broadband spectrum of a 1.1 μm wide and 37.5 μm bend radius diamond racetrack resonator collected by fiber taper measurement. Inset shows optical micrograph indicating the fiber taper coupling position. High-resolution spectra of near critically coupled (g) TE-like and (h) TM-like modes, with Lorentzian fits to the data also shown. Lorentzian fits in **(g)** and **(h)** yield loaded Q-factors of $Q_{L,TE}$ ~ 151,000 and $Q_{L,TM}$ ~ 113,000 respectively.

To illustrate how a vertically supported, triangular cross-section diamond nanobeam functions as a low loss optical waveguide, optical eigenmode solver software (MODE Solutions, Lumerical Solutions Inc.) was used to simulate the ideal vertical support cross-section. Figure 4.3 (a) and (b) show fundamental TE-like and TM-like mode profiles of the support cross-section, respectively, for a propagation wavelength of λ = 1550 nm. Here, the nanobeam width is increased 15 % from a nominal waveguide width of 1.1 μm, resulting in a 165 nm wide diamond 'fin' supporting the waveguide. The distance between the diamond substrate and the bottom of the diamond waveguide was varied from 1 to 2

microns. The optical loss estimated from simulation, which is plotted in Figure 4.3 (c), confirmed the ideal support cross-section can be well below 1 dB/cm for both supported modes, given the separation between the bottom of the waveguide and substrate exceeds ~ 1.8 μm. Additionally, increasing the relative width modulation to 25%, while keeping the width of diamond fin at 165 nm, lowers the optical loss slightly from the nominal design.

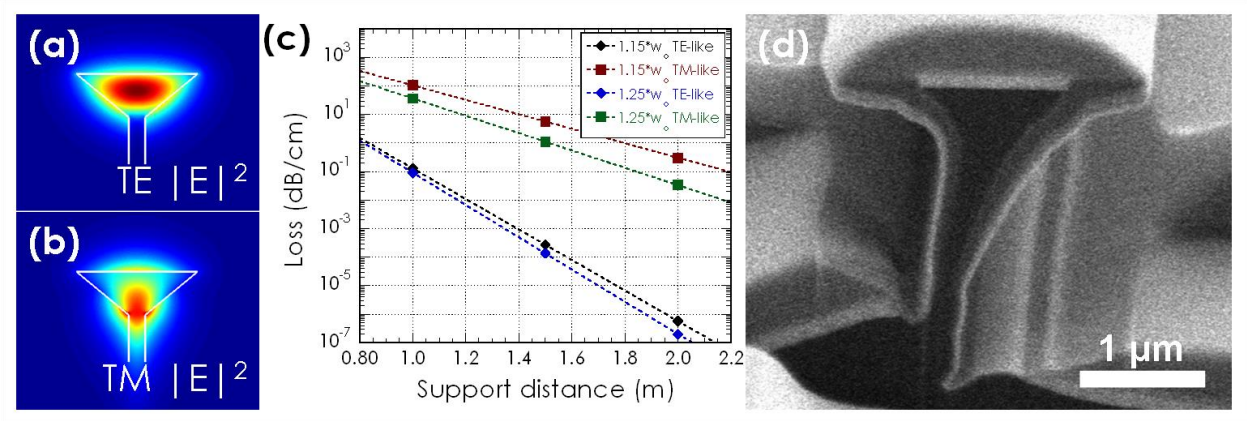

Figure 4.3 | Vertically supported diamond waveguide analysis. Simulated mode profiles (λ = 1.55 μm, electric field norm) of the 1.265 μm wide (a) transverse electric (TE-like) and (b) transverse magnetic (TM-like) vertical support waveguide modes. Here, the width of the diamond 'fin' region supporting the waveguide is 165 nm. (c) Plotted optical loss estimated from simulations for the TE/TM-like modes of a diamond vertical support structure as a function of separation between the bottom of the diamond waveguide and substrate (labeled 'Support distance'). (d) Scanning electron microscope (SEM) image of focused ion beam (FIB) cross-sectioned tapered vertical support near its maximum width (scale bare corresponds to 1 μm). All SEM images were taken at a 60° stage tilt.

Figure 4.3 (d) shows a FIB-milled cross-section of the pedestal-like structure achieved in the vicinity of the maximum width of the vertical support. Note this cross-section is taken from the diamond racetrack resonator which produced the data shown in Figure 4.2. The separation between diamond waveguide and the substrate for this structure is nearly 2 μm. While not detrimental to device performance (as confirmed experimentally), irregularity in the pedestal-like cross-section is clearly observed and attributed to an etch

rate anisotropy, where material was removed at a slightly faster rate from the right side of the support shown in Figure 4.3 (d).

With the demonstration of diamond racetrack resonators supporting high optical Q-factors, we have shown it is possible to vertically support angled-etched diamond waveguides, while not sustaining substantial optical losses. In order to demonstrate the flexibility and scalability of such vertically supported waveguides, we have also developed ultra-long optical path length, and thus small free spectral range (FSR), looped diamond waveguide resonators. Figure 4.4 shows several example devices fabricated with total path lengths of approximately 0.5 mm, 1 mm, 1.5 mm, and 2 mm. In order to produce such structures, a total of 8, 13, 23, and 28 support structures, respectively, were used along the waveguide path. We note that the linear density of support structures for these waveguides varies, and is fundamentally limited by the length of diamond waveguide which is not susceptible to snapping down (a parameter which varies with waveguide geometry, substrate separation, and whether critical point drying is used).

In such long optical path lengths, the projected FSR can easily reach sub-nm for these devices at telecom wavelengths. Narrow FSR resonators have applications in nonlinear optics [32, 165, 166], such as the generation of on-chip diamond Raman lasers where it is necessary to have a cavity resonance specifically positioned at both an incident laser pump wavelength and also the longer Raman-scattered (Stokes) wavelength. Smaller FSR greatly improves the probability of having such exactly placed cavity modes. To confirm that low loss waveguiding persists in this large looped diamond waveguide structures, fiber taper coupling was again used to collect transmission spectra in the telecom band. Figure 4.4 (e) shows a broad band spectrum (with the fiber taper coupling position displayed as the inset) taken from the device shown in Figure 4.4 (c). Three sets of modes are revealed, two of which are high-Q and attributed to the fundamental modes of TE-like and TM-like transverse polarization, while the third is likely a higher order transverse mode as per the low Q-factor. The estimated loaded Q-factor for one of the

fundamental looped waveguide modes was $Q_L \sim 99{,}000$, as shown in Figure 4.4 (f), which confirms angled-etched diamond waveguides are low loss, scalable photonic elements.

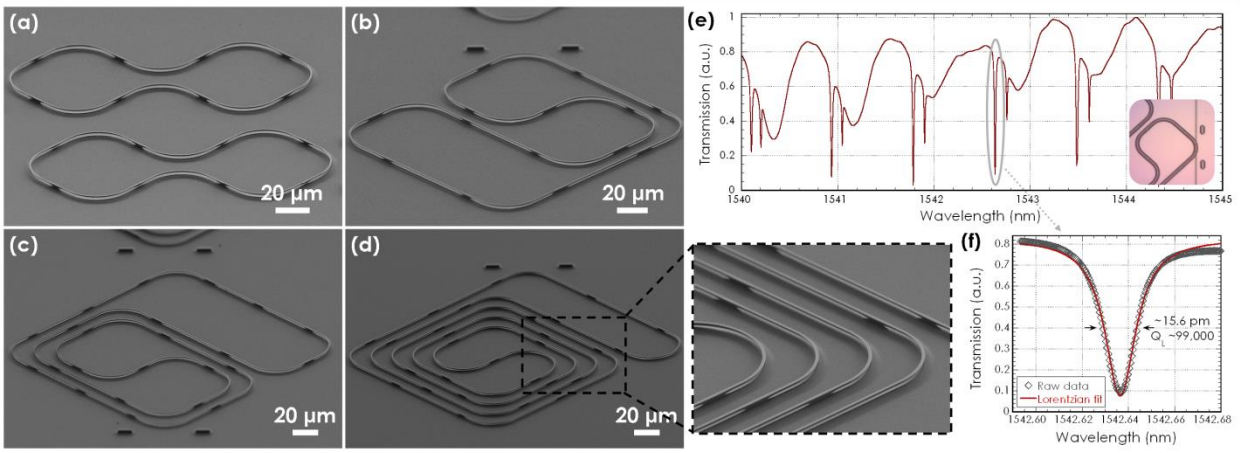

Figure 4.4 | Long optical path length, looped diamond waveguides. SEM images of several fabricated devices comprised of long, looped diamond waveguides with on-chip optical path lengths of approximately (a) 0.5 mm, (b) 1 mm, (c) 1.5 mm and (c) 2 mm long. The inset displays suspended, close packed curved waveguides with significant clearance. (e) Representative normalized broadband spectrum of the resonator shown in panel (c) collected by fiber taper measurement, with the fiber taper coupling position indicated by the inset. (f) Corresponding high-resolution spectra of a cavity resonance, with loaded Q-factors indicated.

4.3 DIAMOND OPTICAL NANOCAVITIES AT VISIBLE WAVELENGTHS

To utilize the broadband nature of diamond, we explored the potential of our angled-etching approach to realize optical cavities operating at visible wavelengths. Visible diamond cavities are of great interest

for the enhancement of emission properties of diamond's luminescent defects, such as the negatively SiV^- center (ZPL at $\lambda \sim 740$ nm) [59-61, 63, 167] and, in particular, the NV^- center, with its ZPL at $\lambda \sim 637$ nm [62, 69-72, 122]. To realize visible band optical cavities in diamond, all design parameters for devices operating at telecom wavelengths are scaled down by a factor of approximately 2.5, and no additional modeling was needed. This design flexibility is an inherent property of angled-etching in which device thickness is coupled to its width. The same is not true for the planar technologies where one dimension is always fixed by the thickness of the device layer (e.g. a 220 nm thick silicon device layer in the case of SOI). Therefore, angled-etching allows for the integration of devices operating over a wide wavelength range (UV to mid-IR) to be easily integrated on the same diamond chip [133].

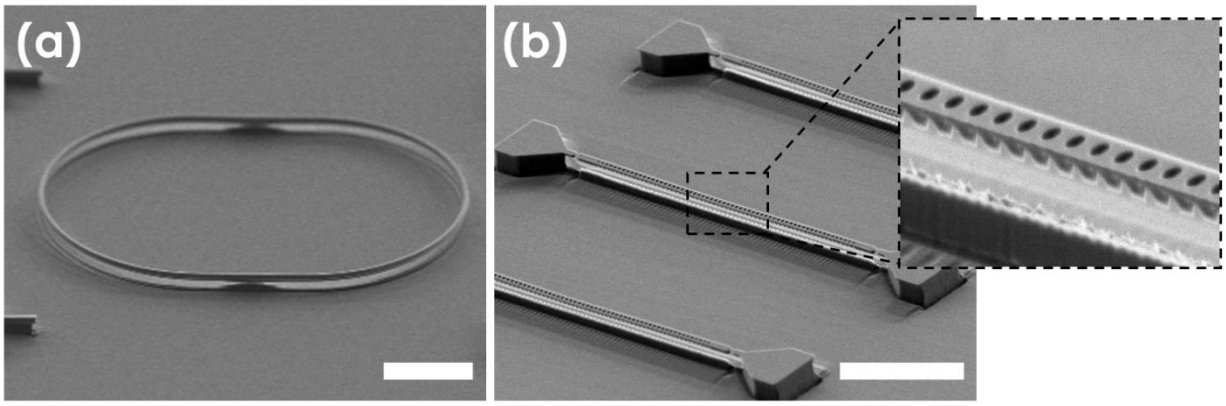

Figure 4.5 | Diamond optical nanocavities fabricated for operation at visible wavelengths. Scanning electron microscope (SEM) images of **(a)** a fabricated diamond racetrack resonator supported from the bottom and **(b)** a fabricated diamond nanobeam photonic crystal cavity operating at visible wavelengths. Scale bars for SEM images in **(a)** and **(b)** correspond to 10 μm and 5 μm respectively. All SEM images were taken at a 60° stage tilt.

Figure 4.5 (a) shows a fabricated visible band diamond racetrack resonators, with a ~ 500 nm wide suspended waveguide and 17.5 μm bend radius. In such devices, the material segment supporting the free-standing waveguide is estimated to be ~ 90 nm thick. A broadband normalized transmission spectrum,

shown in Figure 4.6 (a), is obtained again by fiber taper coupling, using a combination of tunable red laser (635 nm to 639 nm) and super-continuum source. For transmission measurements at visible wavelengths, fiber tapers were manufactured from commercial SM-600 fiber via wet etching in hydrofluoric acid [168]. Bare SM-600 fiber was again mounted in a U-shape configuration, followed by localized wet etching in hydrofluoric acid near the center. The hydrofluoric acid was covered with a thin layer of o-xylene on top in order to promote gradual taper formation via the oil/water interface meniscus. A two-step etch process which included ~ 30 minutes of etching in concentrated hydrofluoric acid, followed by ~ 30 to 50 minutes etching in 5:1 buffered oxide etch (BOE) was used to thin the final taper region to a diameter of ~ 500 to 700 nm. Following visible fiber taper formation, the mounted fiber was again spliced into the same physical set up as described for telecom band measurements. A fiber coupled supercontinuum laser source (EXW-4, NKT Photonics) and optical spectrum analyzer (OSA, HP 70950B, minimum resolution bandwidth of 0.08 nm) were used to collect broadband spectra in roughly the 680 to 800 nm band. To gauge the instrument resolution, a HeNe laser was connected directly to the OSA. Measurement of the resulting laser emission spectra yielded a line width ~ 70 pm, which is artificially broadened by the instrument resolution. As such, any measured Q-factor near and above 9,000 was deemed resolution limited. To avoid this resolution limitation, a tunable red laser (New Focus Velocity TLB 6304 laser, coarse tuning range of 634.8 to 638.9 nm and fine tuning range of 70 pm) and visible band photodetector (New Focus 1801) were also used to collect transmission spectra. The fine tuning range of the laser was used to accurately measure the Q-factors of cavity modes supported by the diamond racetrack resonators within the ~ 4 nm coarse laser tuning range.

The insets of Figure 4.6 (a) display the fiber taper coupling position with the laser tuned off and on resonance; the diamond race track resonator lights up due to scattered light when the laser is resonant with the optical cavity. We note that due to the small coupling gap necessary at visible wavelengths, van der Waals and or electrostatic attraction between the fiber taper and diamond device forced these measurements to be taken with the fiber taper touching the device. This ultimately limited coupling

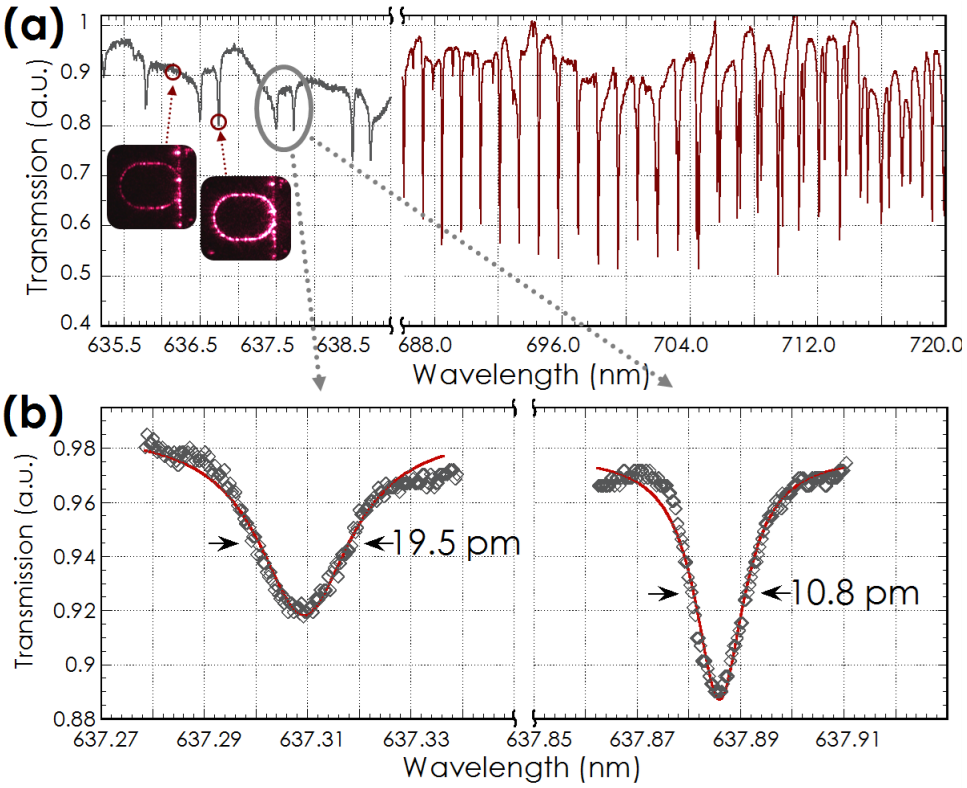

Figure 4.6 | Optical characterization of diamond racetrack resonators at visible wavelengths. (a) Normalized broadband transmission spectrum collected by fiber taper coupling from a diamond racetrack resonator (17.5 μm bend radius and ~ 500 nm beam width) using: i) a tunable red laser and photodiode in 635 nm to 639 nm range (grey curve), and ii) super-continuum source and spectrometer in 688 nm to 720 nm range (red curve). Two sets of supported resonances – the quasi- transverse electric (TE-like) and transverse magnetic (TM-like) waveguide modes – are again apparent. The insets reveal the fiber taper coupling position with a red laser tuned off and on resonance with the optical cavity. **(b)** Corresponding high resolution spectra of two cavity modes near ~ 637 nm collected via a tunable laser, with Lorentzian fits to the data also shown. Lorentzian fits to each resonance in **(b)** yield loaded Q-factors of ~ 33,000 and 59,000.

efficiency and measured cavity Q-factors. High resolution spectra, collected with the tunable laser, of racetrack resonator cavity modes located at approximately ~ 637 nm, are shown in Figure 4.6 (b). Measured loaded Q-factors of the cavity modes were ~ 33,000 and ~ 59,000. For cavity modes at longer wavelengths, accurate measurement of their Q-factors by a tunable laser was not possible. However, Q-factors for resonances near 800 nm estimated from spectra collected by super-continuum excitation

exceed the resolution limit of the spectrometer, and thus were at least 10^4. Therefore, free-standing diamond waveguides fabricated by angled-etching operate with low loss over a large, nearly 200 nm wide bandwidth that covers visible and near-infrared wavelengths.

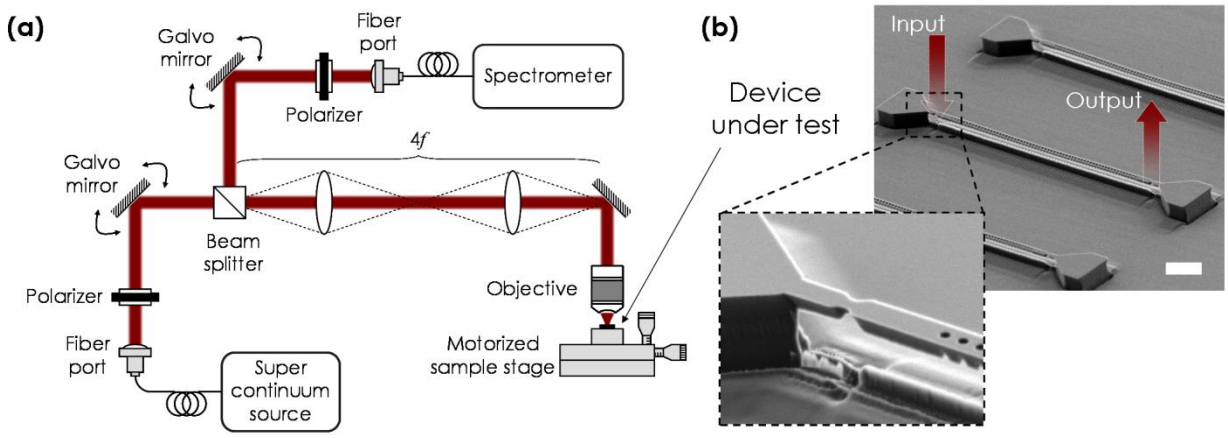

Figure 4.7 | Free-space transmission measurement details. (a) Schematic of the free-space transmission measurement setup used to characterize diamond nanobeam cavities operating at visible wavelengths. See the Methods section of the main text for a detailed description. (b) Scanning electron microscope (SEM) image of a diamond nanobeam cavity (same as Figure 1 (a) of the main text) with a zoomed in image of a specifically placed notch in the diamond nanobeam included as an inset (scale bar corresponds to 2 μm). The locations where light is in- and out-coupled from the diamond nanobeam cavity via notches are illustrated on the image. All SEM images were taken at a 60o stage tilt.

Figure 4.5 (b) shows a representative diamond nanobeam cavity fabricated using the same design as previously described in Section 4.1, with a target resonance for the fundamental TE-like cavity mode of λ_{TE} = 710 nm. In order to characterize such structures, a free-space coupling technique was used in lieu of fiber taper coupling, given the challenge of obtaining proper fiber alignment to small visible nanobeam cavities. The free-space measurement set up – shown in Figure 4.7 (a) – allowed for in- and out-coupling of light at opposite ends of the nanobeam (using specifically placed notches as local broadband couplers, illustrated in Figure 4.7 (b)), thus enabling the free-space transmission measurements. Transmission

measurements conducted by free-space coupling utilized a home built confocal microscope in which a high numerical aperture (NA = 0.95) objective was used to focus laser light onto the sample. The input laser optical path was scanned using a galvo mirror imaged onto the back of the objective with a pair of lenses comprising a 4f imaging system. Additionally, a beam splitter was placed between the input channel galvo mirror and the 4f imaging system in order to incorporate a collection channel with independent scanning control via its own set of galvo mirrors. The free-space coupling set up was thus able to pump and collect light at two spatially separated positions, which allowed for free-space transmission measurements. Positioning of a target device under the objective was accomplished by precision motorized stages. Light from a supercontinuum laser source (EXW-4, NKT Photonics) was coupled into the diamond nanobeam cavity, with light out-coupled from the structure sent to a spectrometer. Free-space polarizers were also included in both the input and collection channels.

A set of representative transmission spectra, collected via super-continuum excitation and spectrometer, taken from the same device but at different input/collection polarizations, are shown in Figure 4.8 (a). These spectra correspond to TM-like (green curve) and TE-like (blue curve) polarized light transmitted through the diamond nanobeam waveguide which contains the optical cavity. Stop band (no transmission) and pass bands (high transmission) of the photonic crystal are clearly seen (the approximate location of the transition indicated with a dashed grey line), with the sharp resonances in the stop band corresponding to cavity modes. High resolution spectra of the fundamental TM-like and TE-like cavity modes are shown in Figures 4.8 (d) and (e), revealing waveguide coupled Q-factors of $Q_{TM} \sim 4{,}400$ and $Q_{TE} \sim 5{,}100$, respectively. Of the fabricated visible band nanobeam cavities, our best device had a measured Q-factor of $Q_{TE} \sim 8{,}200$. The extremely small on-resonance transmission value (< 5%) recorded for both TE-like and TM-like cavity resonances is attributed to large fabrication-induced radiative losses (most likely scattering due to surface roughness and/or material absorption), as evident from the measured Q-factors being much smaller than Q-factors of the cavity design. As a result, the cavity losses into the feeding waveguide are minimal, preventing a large detected on-resonance signal in the transmission spectrum.

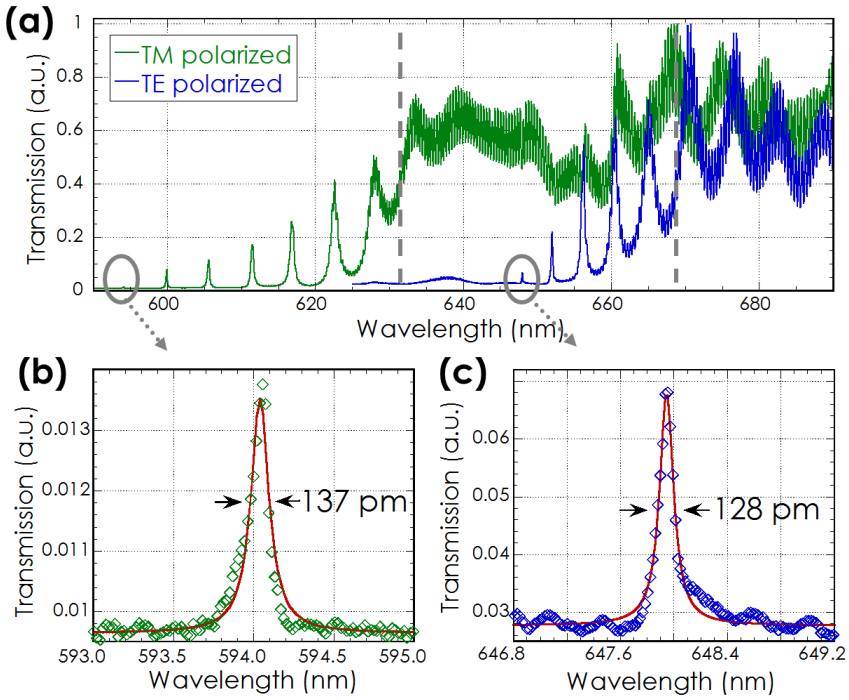

Figure 4.8 | Optical characterization of diamond nanobeam cavities at visible wavelengths. (a) Representative broadband transmission spectra of a fabricated diamond nanobeam photonic crystal cavity operating in visible collected via free space coupling at different input polarizations. High resolution spectra of the fundamental **(b)** TM-like and **(c)** TE-like cavity modes, with Lorentzian fits to the data also shown. Lorentzian fits in **(b)** and **(c)** yield waveguide coupled Q-factors of $Q_{TM} \sim 4{,}400$ and $Q_{TE} \sim 5{,}100$, respectively.

4.4 FIBER-INTEGRATED DIAMOND NANOPHOTONIC NETWORKS

By routing photons via vertically supported diamond waveguides which connect numerous optical elements (namely photonic resonators) and incorporating on-chip/off-chip coupling schemes, a truly integrated diamond nanophotonics platform may be realized. The main outstanding issue is how to

efficiently link off-chip fiber optics with on-chip diamond nanophotonic networks. To this end, we demonstrated such an integration scheme, as described in what follows.

In silicon nanophotonics, popular on-chip coupling schemes realized through conventional planar fabrication include grating couplers [101, 169] or mode-size converters for end-fire coupling from macroscopic fibers [100, 170]. However, the additional fabrication complexity necessary to realize such on-chip coupling structures make these schemes impractical (at the current time) for diamond nanophotonic networks fabricated by angled-etching. Nevertheless, off-chip/on-chip coupling to optical fiber networks may be adapted for diamond nanophotonics realized by angled-etching. Namely, by employing a single-ended conical optical fiber taper, physical contact between the fiber taper tip and a free-standing diamond waveguide taper would yield highly efficient coupling of light via adiabatic mode transfer. Such a scheme was originally proposed by T.G. Tiecke et al. [103], and developed for silicon nitride nanophotonic systems. Following this scheme, we demonstrate efficient coupling (> 90 % power coupling) with on-chip diamond nanophotonic networks.

Figure 4.9 displays a series of SEM images revealing a prototype diamond nanophotonic network for operation at telecom wavelengths, realized by angled-etching techniques. The on-chip nanophotonics consist of four key components: (1) free-standing diamond waveguides, (2) integrated diamond optical nanocavities (Figure 4.9 (b) and (c)), (2) vertical tapered supported structures (Figure 4.9 (d) and (e)), and finally, (4) free-standing diamond waveguide tapers (Figure 4.9 (f)). Of the diamond nanophotonic resonators we demonstrated previously [133], one-dimensional photonic crystal nanobeam cavities offer seamless integration with on-chip diamond waveguides, since the cavity architecture is built into a suspended nanobeam segment [153]. Additionally, the diamond nanobeam cavity design presented in Section 4.1 enables both high Q-factor and high on-resonance transmission by engineering cavity losses to the waveguide to dominate all other loss channels, such as radiation losses due to scattering and/or material absorption [154]. Thus, a diamond nanobeam cavity suspended by tapered vertical support structures on each end may be optically interfaced with via light transmitted through the feeding

waveguide. The relevant cavity design parameters are discussed in detail in the Appendix B. Moreover, the ability to couple light from off-chip optical fibers to such on-chip integrated diamond optical nanocavities may provide a preferred route for fiber-coupled, high bit-rate, all-optical QIP with diamond color centers.

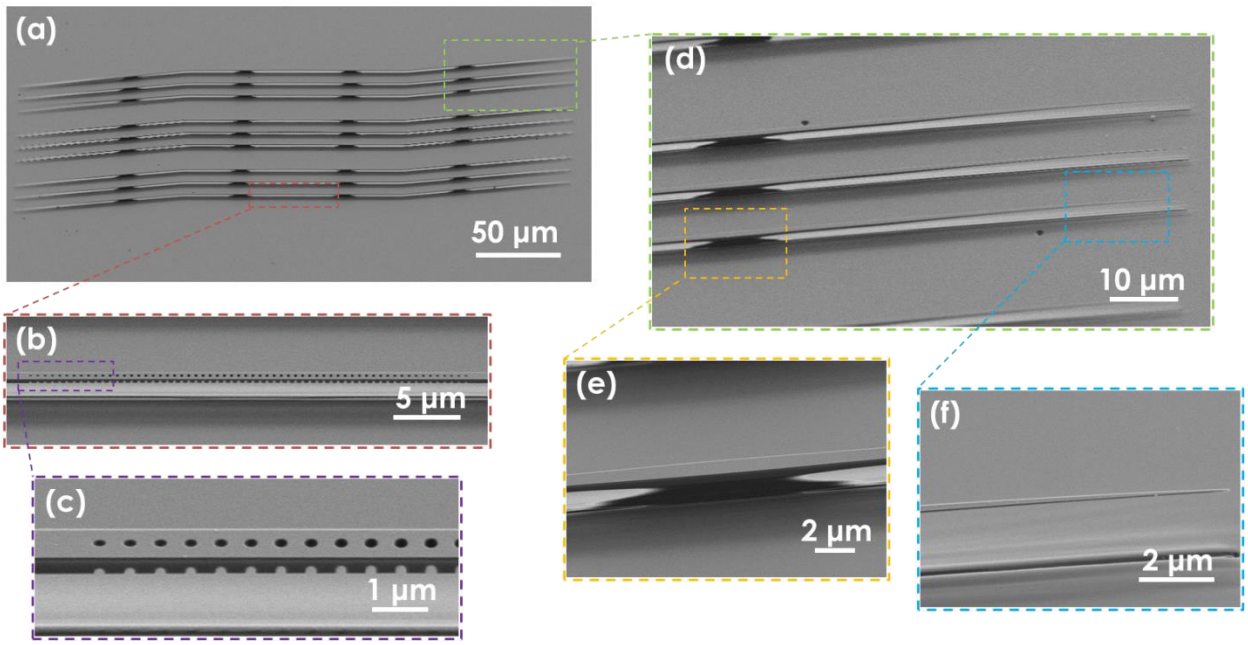

Figure 4.9 | Integrated diamond nanophotonic networks. SEM images of (a) an array of on-chip diamond nanophotonic systems designed for operation at telecom frequencies, each consisting of four key components: (1) free-standing diamond waveguides, (2) integrated diamond optical nanocavities (panels (b) and (c)), (3) vertical tapered supported structures (panels (d) and (e)), and finally, (4) free-standing diamond waveguide tapers (panels (d) and (f)).

Free-standing diamond tapers gradually change the effective refractive index of the waveguide mode along the propagation direction, such that all optical power remains in the target eigenmode. This minimizes coupling to other higher-order and radiation modes, enabling highly efficient adiabatic transfer. Generally, this slowly changing effective index is easily achieved by tapering the waveguide lateral dimensions over a length many times longer than the wavelength of propagating light. In the case

of silicon nanophotonics, waveguide tapers for telecom light reach lengths of several hundred microns [102]. However, as is the case for free-standing diamond nanobeam waveguides, the length of the taper is limited, since one that is too long will fail mechanically (snap down), touch the substrate and leak light into the bulk diamond. Therefore, it is important to determine the longest diamond waveguide taper length available via angled-etching fabrication techniques.

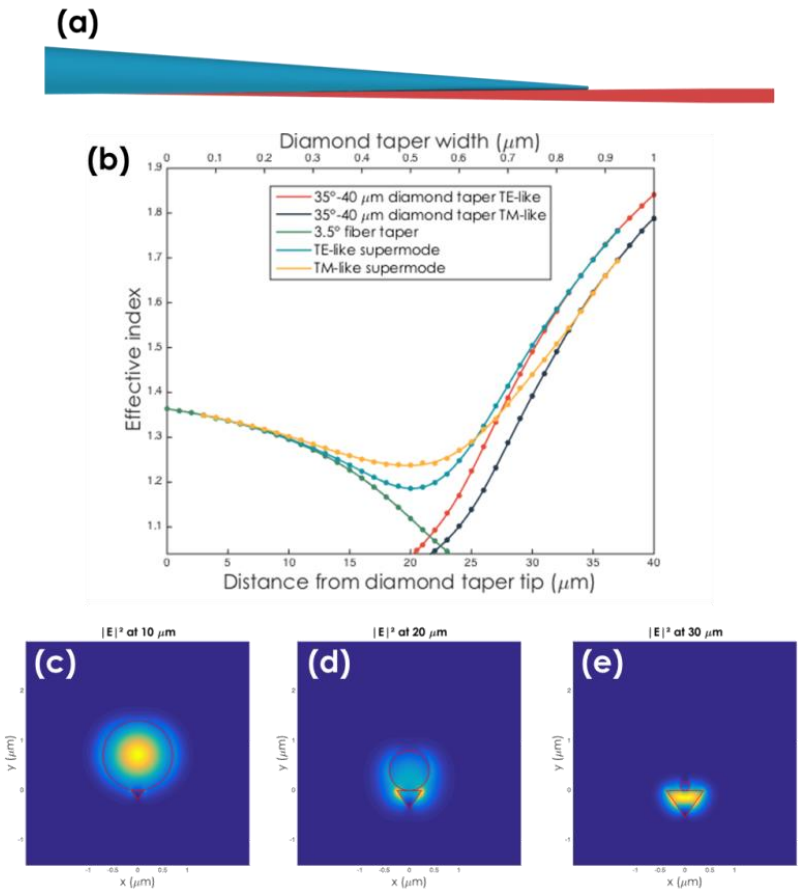

Figure 4.10 | Adiabatic transfer between fiber taper and diamond waveguide taper modes. (a) Schematic of fiber-waveguide coupling. The fiber (blue) has a conical shape and is attached to a tapered triangular cross-section diamond waveguide taper (red). (b) Effective index (n_{eff}) of the fiber and waveguide modes for an opening angle of the fiber (waveguide) of 3.5° (1.5°). (c) Cross sections of $|E|^2$ obtained from the FDTD simulation at various points along the coupler for the TE-like diamond waveguide mode polarization.

A linear taper was chosen for fabrication simplicity and the taper was designed to evolve from the standard diamond waveguide width, down to a sub < 100 nm point. Figure 4.9 (d) show SEM images vertically supported waveguide sections for operation in the telecom band (width ~ 1 μm), leading into diamond waveguide tapers. Diamond tapers with various lengths were fabricated to determine the maximal taper length that consistently resulted in a free-standing structure. Lengths of 25 μm to 65 μm, in steps of 5 μm, were tested. Following these tests, a taper length of 40 μm (as shown in Figure 4.9 (d)) was chosen to ensure a near unity fabrication yield of diamond tapers. Figure 4.9 (f) reveals a final taper tip radius < 100 nm. The final diamond taper angle is ~ 2 °.

Figure 4.10 (a) schematically represents the coupled diamond waveguide taper and single-ended optical fiber taper system. In the region of physical contact between the tapering waveguides and optical fiber, the propagating guided modes couple via their evanescent fields forming a hybridized "supermode". The efficiency of adiabatic conversion between the fundamental diamond waveguide mode and single-mode optical fiber is ultimately set by the fraction of optical energy which remains in this supermode throughout propagation in this region [103]. Via an eigenmode solver (MODE Solutions, Lumerical), we calculate the effective indices of our diamond waveguide taper design physically coupled to a single-ended optical fiber taper (with a taper angle of 3.5°), as shown in Figure 4.10 (b). Here, we consider both TE-like and TM-like fundamental waveguide modes, and plot the calculated effective indices of the fiber mode, waveguide mode, and hybridized supermode of the combined structure. With this geometry, the latter has an effective index of n_{eff} greater than ~ 1.2 over the entire length of the coupler, for both TE-like and TM-like diamond waveguide modes. To confirm adiabatic mode transfer, we employ FDTD simulations (Lumerical) to launch a propagating fundamental mode of either TE-like or TM-like polarization down the diamond waveguide, and monitor the power output in the HE_{11} optical fiber mode after the coupling region. A power transfer greater than 98 % was confirmed for both polarizations of the fundamental diamond waveguide mode. Also, while the combined structure supports propagation modes of two polarizations, they are orthogonal and thus do not couple. Figure 4.10 (c) to (e) display cross-

sectional field profiles obtained from the FDTD simulation at various points along the coupler for the TE-like diamond waveguide mode polarization.

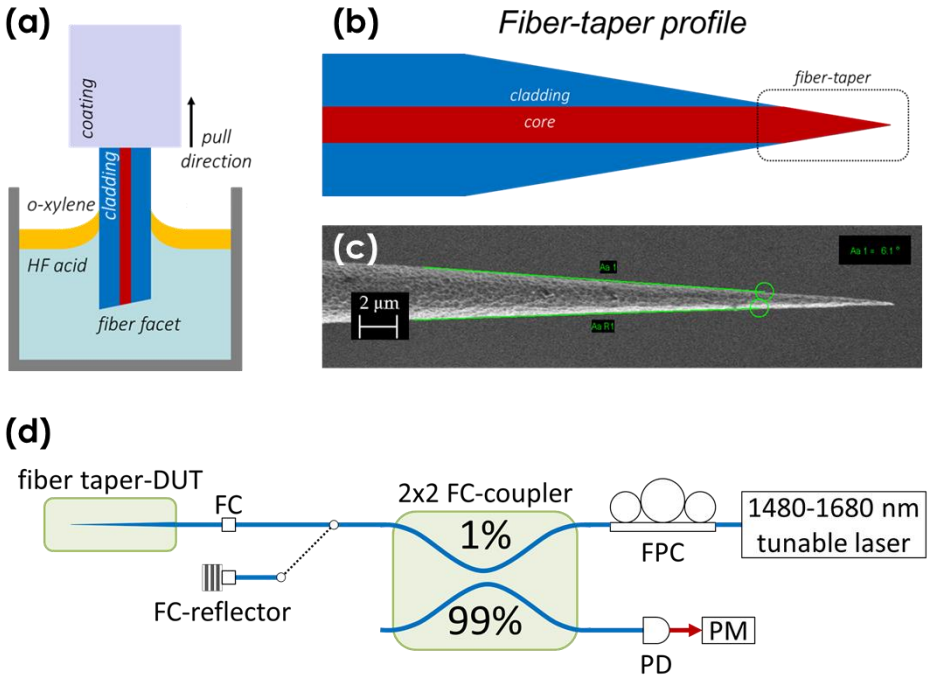

Figure 4.11 | Single-mode optical fiber taper fabrication and characterization. (a) Schematic of fabrication of single-ended conical fiber tapers by hydrofluoric acid etching. (b) Illustration of the fiber taper refractive index profile, with a corresponding (c) SEM image of a fabricated fiber taper tip. (d) Schematic of the fiber optical network used to the characterized on-chip diamond nanophotonic networks with single-ended optical fiber tapers.

Single-ended conical optical fiber tapers were fabricated by a wet etching technique, where commercial telecom single-mode optical fibers (SMF-28, Corning) were submerged in hydrofluoric acid (HF) to form the taper profile [168], as depicted in Figure 4.11 (a) and (b). Specifically, the HF was contained in a Teflon beaker and layer with a thin layer of o-xylene on top in order to promote gradual taper formation via an oil/water interface meniscus which wicks up the fiber. The meniscus height depends on the diameter of the fiber: as the diameter reduces with acid etching, the meniscus height decreases, naturally tapering the fiber diameter over a length defined by the etch rate and initial fiber

diameter. When the acid etches completely through the fiber diameter, the fiber taper tip has finished forming and the process self-terminates. By drawing the fiber out of the HF solution, the taper length can be extended, which enables full control over the final taper angle. In general, for taper angles less than ~ 5°, adiabatic transfer of the HE_{11} optical fiber mode over the length of the fiber taper tip is achieved, and coupling to radiation or higher order fiber modes is suppressed. Figure 4.11 (c) shows a SEM image of a representative fiber taper tip fabricated by HF etching, with a final taper angle of ~ 6°.

To characterized fabricated on-chip diamond nanophotonic networks, the single-ended optical fiber taper was installed into a custom set up, where its position with respect to the device under test (DUT) was precisely controlled via motorized stages. The optical fiber network used to collect optical spectra from the integrated diamond nanobeam cavities is shown in Figure 4.11 (d). Two tunable lasers (Santec TSL-510, tuning range from 1480 to 1680 nm) were used, along with an inline fiber polarizer, and high gain InGaAs photodetector (EO Systems, IGA1.9-010-H) and power meter to record reflection spectra. Laser light was sent to a 2x2 99:1 fiber coupler, with 1 % of input light sent to the optical fiber taper and DUT, and 99% of reflected light returned to the photodetector and power meter. All collected spectra were normalized by reflected data collected from a fiber-coupled retroflector (Thorlabs, P5-SMF28ER-P01-1) with > 98% reflection over the laser tuning bandwidth.

Figure 4.12 (a) displays an optical micrograph of the coupling region where the optical fiber taper tip is in physical contact with the diamond waveguide taper (the contact length is ~ 30 μm). A normalized reflection spectra collected from a representative device is shown in Figure 4.12 (b). A set of reflection dips attributed to localized resonances of the diamond nanobeam cavity with TE-like polarization. In Figure 4.12 (d), a high-resolution scan of the fundamental TE-like cavity mode at 1638.1 nm is shown, with a Lorentzian fit to the spectra yielding a total Q-factor of ~ 187,000, with nearly 20% on-resonance extinction. Higher order longitudinal modes of the cavity have much lower measured Q-factors, but are perfectly waveguide damped, yielding critically coupled resonances.

Figure 4.12 (d) to (g) show optical micrographs collected overhead of the cavities with an infrared camera. In each image, the laser position is tuned relative to the fundamental TE-like cavity mode, with light scattered by the cavity visible when the laser is tuned closed to resonance. With the laser tuned off-resonance, only a small amount of scattered light at the entrance to the cavity structure is visible, which is likely the result of insertion losses between the propagating waveguide mode and the perforated nanobeam cavity structure.

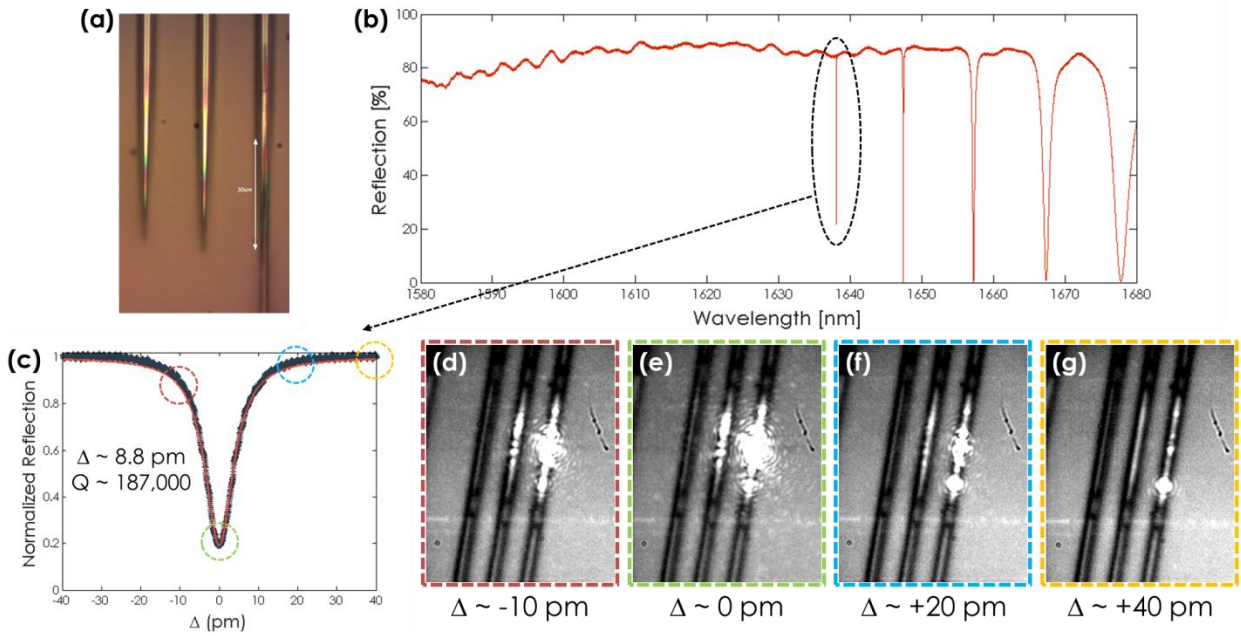

Figure 4.12 | Reflection spectra collected via fiber taper tip coupling. (a) Optical micrograph of the fiber-waveguide coupling region. (b) Normalized broadband reflection spectra of a diamond nanobeam cavity operating at telecom wavelengths. Reflection dips correspond to cavity modes, with a high-resolution spectra of the fundamental TE-like cavity mode included in (c). Corresponding overhead infrared camera images of the nanobeam cavity taken with the laser wavelength tuned (d) –10 pm, (e) 0 pm, (f) + 20 pm, and (g) + 40 pm from the cavity resonance. Light scattered out of the waveguide is visible when the laser is tuned close to the cavity resonance, confirming the spectral feature is a cavity mode.

Away from the localized resonances, we assume the diamond nanobeam cavity ideally reflects all the light, allowing for a calculation of the coupling efficiency. To do so, the laser is tuned just off-resonance from the second order TE-like cavity mode, and the input polarization is adjusted to maximize the reflected signal. The input power to the fiber taper tip (P_{in}) and the reflected powers after the 2x2 coupler (P_r) are measured with a calibrated power meter. The normalized reflection is thus given by $P_r/P_{in} = \eta_c^{\,2}\eta_{BS}\eta_m\eta_{FC}$, where η_c is the coupling efficiency of the fiber-waveguide tapers, η_{BS} is the calibrated coupling ratio of the 2x2 fiber coupler, η_m is the reflection of the nanobeam cavity Bragg mirror, and η_c is the coupling efficiency of the FC-FC fiber coupler immediately before the fiber taper tip (measured to be ~ 95 %). We assume $\eta_m \sim 1$ and neglect any losses of the propagating mode down the diamond nanobeam waveguides, and thus estimate a lower bound on the fiber taper tip coupling efficiency. For the measurement displayed in Figure 4.12, we estimate a coupling efficiency $\eta_c \sim 96$ % at a laser wavelength near 1650 nm. Note that the broadband spectrum in Figure 4.12 (b) plots a reflected signal normalized by the broadband fiber retroreflector, and is thus a secondary measurement of coupling efficiency. Here, the normalized reflection (assuming near unit reflection of the fiber retroreflector) is ~ $P_r/P_{in} = \eta_c^{\,2}$, since the fiber retroreflector and fiber taper experience the same system losses From the plot in Figure 4.12(b), an estimated coupling efficiency of ~ 94 % is extracted at ~ 1650 nm, in line with the measurement made with the power meter. The variable reflected signal in Figure 4.12 (b) is attributed to wavelength-dependent changes in fiber polarization.

Chapter 5

Diamond optomechanical crystals

Optomechanical crystals (OMCs), first demonstrated in silicon [171], and later in other materials like silicon nitride [172, 173] and gallium arsenide [174], have emerged as a fruitful optomechanics platform, wherein radiation pressure effects provide exquisitely sensitive optical control of mechanical vibrations. Such systems have enabled demonstrations of quantum ground state cooling [175], optomechanically induced transparency [176], squeezed light [177], and wavelength conversion [156]. Highly coherent photon-phonon interactions in OMCs is the direct result of the ability to engineer a large single-photon optomechanical coupling rate (g_o), while retaining sufficiently small optical (κ) and intrinsic mechanical (γ_i) dissipation rates. Similar structures realized in single-crystal diamond – which features a unique combination of superior mechanical, thermal, and optical properties [4] – are expected to exhibit pronounced optomechanical interactions, quantified by the cooperativity parameter $C = 4n_c g_o^2 / \kappa \gamma_i$ (where n_c is the intracavity photon number). Specifically, diamond's wide bandgap (~ 5.5 eV) precludes two- or multi-photon absorption over a wide wavelength range (from visible to infrared). This, combined with its high thermal conductivity and small thermal expansion, enables monolithic diamond optical cavities that can withstand significant optical power densities, while avoiding degradation in optical linewidth or drifts in resonance wavelength due to thermal lensing. Diamond's large intracavity photon capacity can thus result in large cooperativities necessary for either strong mechanical driving or effective laser cooling [175]. Moreover, diamond is among the stiffest materials known and possess extremely low thermoelastic mechanical damping, with recently demonstrated monolithic diamond cantilevers exhibiting mechanical Q-factors in excess of 10^6 at room temperature [80].

In this chapter, we make use of these features to demonstrate OMCs in single-crystal diamond with unique performance. Our diamond OMCs support a $\omega_m/2\pi \sim 6$ GHz mechanical cavity coupled to a co-resonant photon field at $\omega_o/2\pi \sim 200$ THz, with vacuum optomechanical coupling rate of $g_o \sim 100$ kHz. With an optical linewidth of $\kappa/2\pi \sim 2.5$ GHz, this diamond OMC system operates in the so-called resolved sideband regime ($\omega_m/\kappa > 1$), necessary for efficient radiation-pressure driven dynamic backaction. This enables our diamond OMCs to be optically driven to $C > 1$ at room temperature, highlighted by the observation of "phonon lasing" in our structures [178]. Section 5.1 describes the optimized diamond OMC design, as confirmed by optical and mechanical eigenmode simulations, followed by a discussion of fabricated devices in Section 5.2. Section 5.3 describes optical and mechanical mode spectroscopy of fabricated diamond OMCs. In section 5.4, we discuss the optomechanical transduction observed under high input laser power, where optomechanical self-oscillations were observed.

5.1 OPTIMIZED DIAMOND OPTOMECHANICAL CRYSTAL DESIGN

Diamond OMCs consist of a one dimensional nanobeam photonic crystal cavity fabricated in single-crystal diamond [133] (discussed previously in Chapter 4) using previously introduced 'angled-etching' techniques [130] (see Chapter 2). The nanobeam cavity is based on a triangular cross-section diamond waveguide perforated with a periodic lattice of elliptically shaped air holes. A photonic bandstructure of one unit cell in this waveguide (Figure 5.1 (a)), shown in Figure 5.1 (b), includes both transverse electric (TE-like, solid black lines) and transverse magnetic (TM-like, dashed blue lines) guided modes. In this work, we focus on TE-like modes near the X-point frequency of $\omega_o/2\pi \sim 200$ THz ($\lambda \sim 1550$ nm), since they can lead to the realization of very high Q-factor optical cavities[133]. Importantly, our photonic crystal waveguide also supports acoustic guided modes that are spatially overlapped with optical modes,

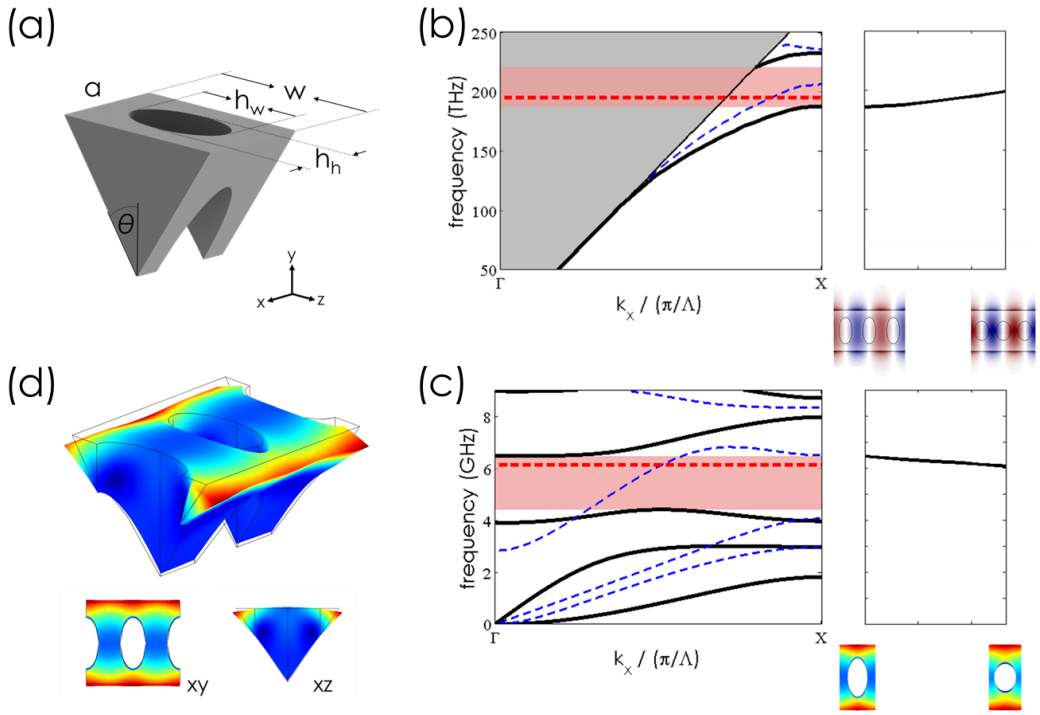

Figure 5.1 | Diamond optomechanical crystal optimized design. (a) Solid model representation of the triangular cross-section diamond unit cell as fabricated by angled-etching. The unit cell is parameterized by the etch angle (θ), width (w), lattice constant (a), and major and minor elliptical air hole diameters (h_w, h_h). Corresponding **(b)** optical and **(c)** mechanical band structures of a nominal unit cell with $\theta = 35^o$ and (a, w, h_w, h_h) = (540, 930, 590, 295) nm. In **(b)**, the grey shaded region indicates the continuum of radiation and leaky modes that exist above the light line for the structure. Below the light line, supported transverse electric (TE-like) and transverse magnetic (TM-like) guided modes are indicted by solid black and dashed blue lines, respectively. In **(c)**, mechanical guided modes shown are for propagation along the x-axis, with y-symmetric and y-antisymmetric vector symmetries again indicated by solid black and dashed blue lines, respectively. Mechanical simulations assume guided mode propagation is oriented with the in plane [110] crystallographic direction, with the z-axis is oriented with [001]. The red shaded regions in **(b)** and **(c)** highlight the optical and mechanical symmetry bandgaps of interest, respectively. **(d)** Three-dimensional mechanical displacement profile of the "flapping" guided mode originating from the Γ-point of the fourth band with y-symmetric vector symmetry – identified as the mechanical mode which yields large displacement and strain overlap with the optical guided mode originating from the X-point of the first (dielectric) TE-like band. Right panels in **(b)** and **(c)** show the tuning of the X-point optical and Γ-point mechanical modes of interest as the unit cell is transitioned smoothly from the nominal unit cell to a defect cell with reduced lattice constant and decreased y-axis air hole eccentricity, specifically (a_{defect}, $h_{w,defect}$, $h_{h,defect}$) = (481, 430, 328) nm.

and can couple to them via radiation pressure. The corresponding mechanical bandstructure (Figure 5.1 (c)) reveals a rich library of guided acoustic modes in the few to 10 GHz frequency range. The guided modes, categorized by even (solid black lines) and odd (dashed blue lines) vector symmetries about the *y*-axis, again yield symmetry based quasi-bandgaps. Following OMC design rules [179, 180], we identified the guided mode derived from the Γ-point of the fourth *y*-symmetric band (frequency of $\omega_m/2\pi \sim 6$ GHz) – referred hereafter as the "flapping" acoustic mode (Figure 1 (d)) – as the mechanical mode of interest for large optomechanical coupling. We also focused on this particular mode due to a large acoustic quasi-bandgap below its native band (indicated by the shaded pink region in Figure 5.1 (c)).

To supplement our discussion on the guided acoustic phonon modes of diamond optomechanical crystals (OMCs) fabricated by angled etching, we present normalized displacement profiles of the nominal unit cell at the Γ ($k_x = 0$) and X ($k_x = \pi/a$) of the mechanical bandstructure displayed in Figure 5.1 (c). Figure 5.2 and 5.3 reveal the guided acoustic modes categorized by even (solid black lines) and odd (dashed blue lines) vector symmetries about the *y*-axis, respectively, with displacement profiles originating from the indicated band edges shown as insets (prospective, top down and cross-section views included). Note, the unit cell lattice constant in the displacement profiles is displayed between the ($h_{w,n}$, $h_{h,n}$) and ($h_{w,n+1}$, $h_{h,n+1}$) center points, in order to clearly reveal displacement components within the air holes. Mechanical simulations included here and throughout the main text use the full anisotropic elasticity matrix of diamond [181], where (C_{11}, C_{12}, C_{44}) = (1076, 125, 578) GPa. However, due to considerations expanded upon in later in Section 5.2 of this chapter, devices characterized in this work were ultimately fabricated with their x-axis oriented with the in plane [110] crystallographic direction. Thus, a rotated version of anisotropic elasticity matrix ensured proper device orientation in our simulations, with guided mode propagation along the *x*-axis aligned with the [110] crystallographic direction, with the z-axis aligned with [001]. Only a small (< 10 %) change in the guide mode frequencies

was observed between simulations with unit cell x-axis alignment to the [100] and [110] in plane crystal directions.

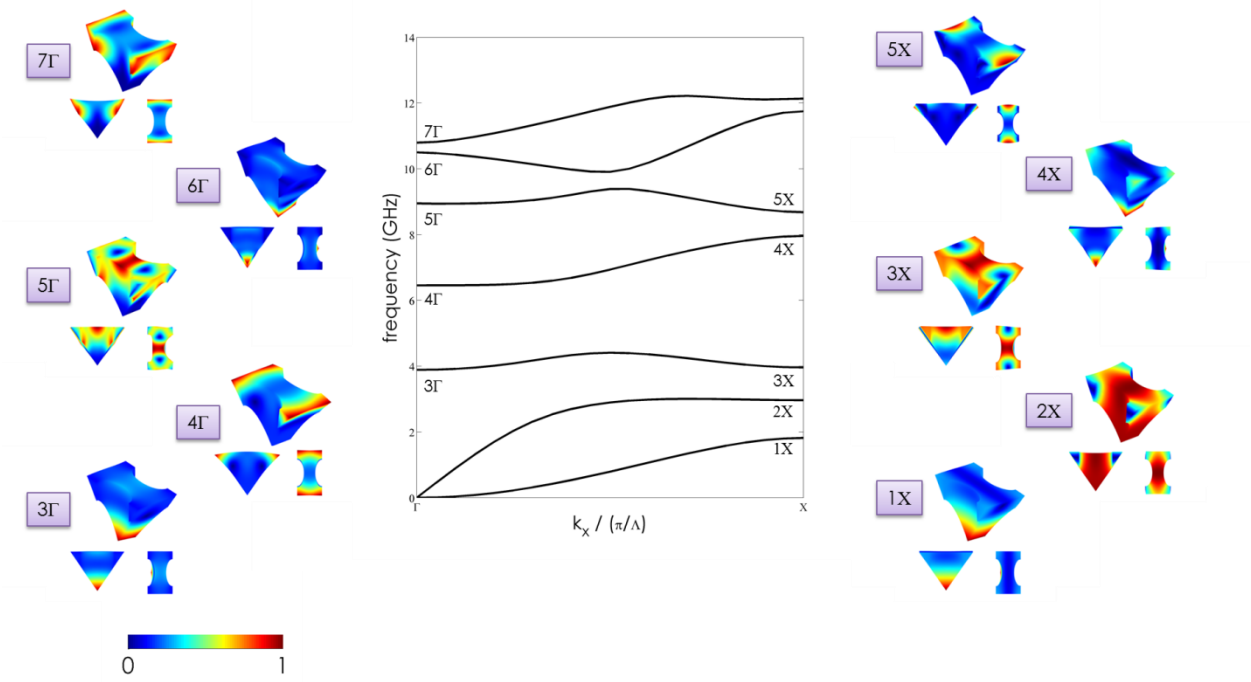

Figure 5.2 | Symmetric diamond OMC acoustic guided modes. Acoustic guided modes with *y*-symmetric vector symmetries supported by angled-etch diamond OMCs. Normalized three-dimensional mechanical displacement profiles of the guided modes originating from the Γ-point and X-point are included as insets.

While the mechanical bandstructures reveal a rich library of guided acoustic modes in the few to 14 GHz frequency range, only guided modes originating from y-symmetric bands ultimately couple to the optical cavity [180]. Additionally, modes originating from the Γ-point ensure large optomechanical coupling rates in the final design [179]. With this in mind, two modes from the Γ-point of y-symmetric bands enable design of diamond OMCs with large single-photon optomechanical coupling rates, g_o. Specifically, the Γ-point modes from the 4th and 7th *y*-symmetric bands, referred to as the "flapping" and "breathing" modes, respectively, were both investigated. However, due to its higher guided mode

frequency, fabricated structures based on designs optimized for the diamond OMC breathing mode were not studied in this work, however remain of interest for future investigations.

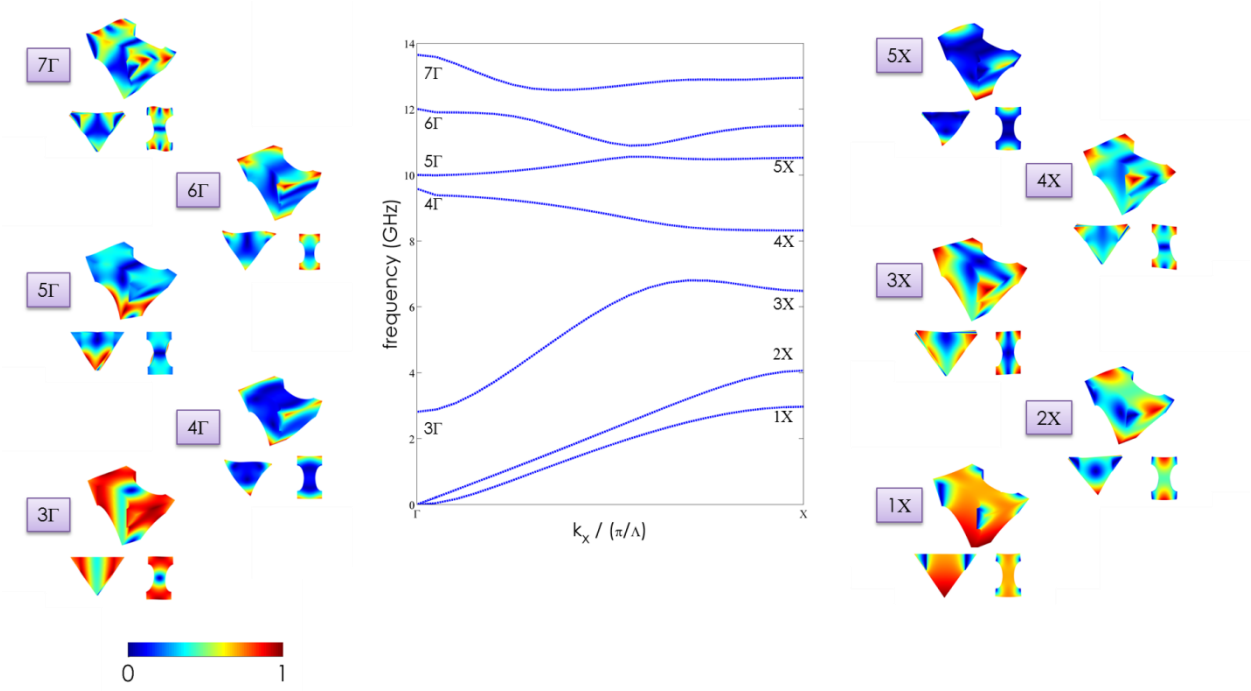

Figure 5.3 | Antisymmetric diamond OMC acoustic guided modes. Acoustic guided modes with *y*-antisymmetric vector symmetries supported by angled-etch diamond OMCs. Normalized three-dimensional mechanical displacement profiles of the guided modes originating from the Γ-point and X-point are included as insets.

The final diamond OMC design relies on transitioning from a "mirror" region formed by the base unit cell in Figure 5.1 (a) to a "defect" cell, with its dimensions selected to simultaneously raise and lower the frequencies of the target optical and mechanical modes of interest, respectively, into their respective quasi-bandgaps. Gradually reducing the unit cell lattice constant while also decreasing the air hole aspect ratio (h_w/h_h) achieves the necessary band edge tuning (see insets of Figure 5.1 (b) and (c)). Out-of-plane scattering losses in the optical cavity were then minimized by transitioning from the mirror region to defect cell over seven lattice periods. This "defect region" is parameterized by the maximum change in lattice constant in the defect region, $d = (1 - a_{defect}/a_{nominal})$, the aspect ratio of the center hole, and

curvature of the transition. Figure 5.4 illustrates the mirror to defect cell transition of our optimized diamond OMC design.

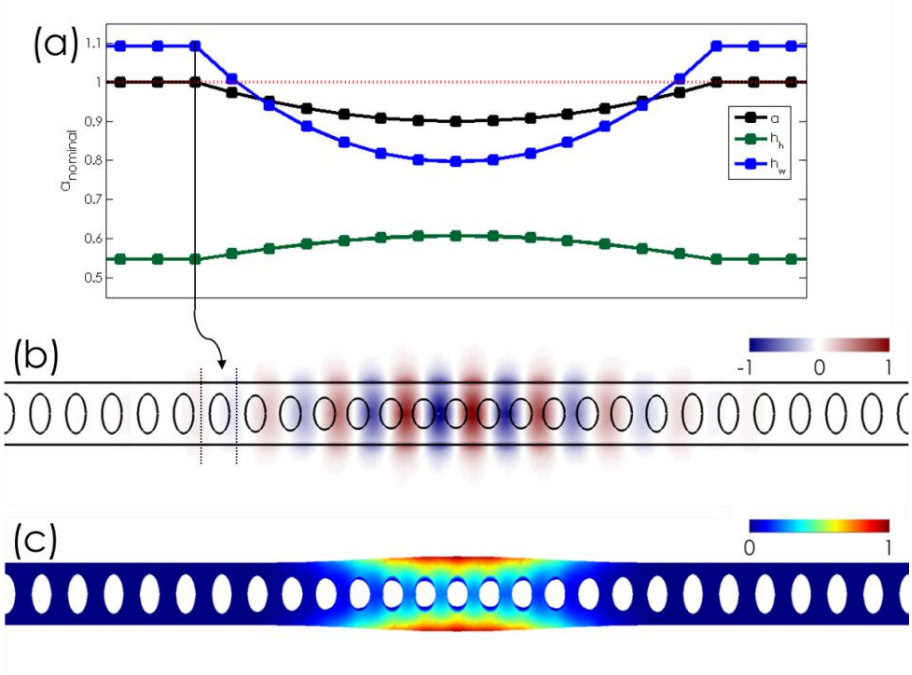

Figure 5.4 | Mirror-to-defect cell transition (a) Plot of the diamond optomechanical crystal defect region unit cell parameters along the length of the nanobeam, in units of $a_{nominal}$. Normalized **(b)** optical E_y field and **(c)** mechanical displacement profile of the optical and mechanical modes localized by the defect region.

The optimized design was determined via previously described numerical optimization methods, based upon FEM simulations (COMSOL) to calculate the optical and mechanical cavity resonance frequencies, ω_o and ω_m, the optical Q-factor, Q_o, and the single-photon optomechanical-coupling rate, g_o. In the optimization, the mirror region unit cell geometry (w, a, h_w, h_h) and the aforementioned defect region parameters were varied, and a fitness function for the optimization was set such as to converge on a design with the largest g_o. Both moving boundary ($g_{o,MB}$) and photo-elastic contributions ($g_{o,PE}$) to the single-photon optomechanical coupling rate were considered [174, 179], with $g_{o,MB}$ given by:

$$g_{o,MB} = -\frac{\omega_o}{2}\frac{\oint(\mathbf{Q}\cdot\hat{\mathbf{n}})(\Delta\varepsilon\mathbf{E}_{\parallel}^2 - \Delta\varepsilon^{-1}\mathbf{D}_{\perp}^2)dS}{\int\varepsilon|\mathbf{E}|^2 dV} \tag{5.1}$$

where **Q** is the normalized displacement field, $\hat{\mathbf{n}}$ is the outward facing surface normal, **E** and **D** are the electric and displacement fields respectively, the subscripts $\parallel$ and $\perp$ subscripts designate field components parallel and perpendicular to the surface respectively, ε is the material permittivity, $\Delta\varepsilon = \varepsilon_{diamond} - \varepsilon_{air}$, and $\Delta\varepsilon^{-1} = \varepsilon_{diamond}^{-1} - \varepsilon_{air}^{-1}$. The photo-elastic contribution to the optomechanical coupling rate, $g_{o,PE}$, for a cubic crystal with *m3m* point symmetry and the x-axis and y-axis aligned to the [100] and [010] crystal directions, respectively, is given by:

$$\begin{aligned} g_{o,PE} = &-\frac{\omega_o\varepsilon_o n^4}{2}\frac{\int\sum\left(4\,\mathrm{Re}\{E_x^* E_y\}p_{44}S_{xy}\right)dV}{\int\varepsilon|\mathbf{E}|^2 dV} \\ &-\frac{\omega_o\varepsilon_o n^4}{2}\frac{\int\sum\left(|E_x|^2\left(p_{11}S_{xx} + p_{12}\left(S_{yy}+S_{zz}\right)\right)\right)dV}{\int\varepsilon|\mathbf{E}|^2 dV} \end{aligned} \tag{5.2}$$

where Σ is a summation, according to Einstein notation x → y → z → x. S_{ij} are the stain tensor components, and p_{ij} are the photoelastic coefficients of diamond [182]: (p_{11}, p_{12}, p_{44}) = (-0.25, 0.043, -0.172).

As mentioned previously, diamond OMCs were fabricated with their x-axis aligned with the [110] crystallographic direction. In the calculation of $g_{o,MB}$ this was taken into account by using a rotated

version of the elasticity matrix. To determine, $g_{o,PE}$, a rotated version of the photo-elastic tensor (p'_{ij}) was used, where:

$$p'_{11} = p'_{22} = \frac{1}{4}\left(p_{11}\left(3+\cos(4\theta)\right)+\left(p_{12}+2p_{44}\right)\left(1-\cos(4\theta)\right)\right) \tag{5.3}$$

$$p'_{33} = p_{11} \tag{5.4}$$

$$p'_{12} = p'_{21} = \frac{1}{4}\left(p_{12}\left(3+\cos(4\theta)\right)+\left(p_{11}-2p_{44}\right)\left(1-\cos(4\theta)\right)\right) \tag{5.5}$$

$$p'_{13} = p'_{23} = p'_{31} = p'_{32} = p_{12} \tag{5.6}$$

$$p'_{44} = p'_{55} = p_{44} \tag{5.7}$$

$$p'_{66} = \frac{1}{4}\left(2p_{44}+\left(1+\cos(4\theta)\right)+\left(p_{11}-p_{12}\right)\left(1-\cos(4\theta)\right)\right) \tag{5.8}$$

$$p'_{16} = p'_{61} = \frac{1}{4}\sin(4\theta)\left(2p_{44}+p_{12}-p_{11}\right) \tag{5.9}$$

$$p'_{26} = p'_{62} = \frac{1}{4}\sin(4\theta)\left(p_{11}-p_{12}+2p_{44}\right) \tag{5.10}$$

with $\theta = 45^{o}$. The final expression for $g_{o,PE}$ is then:

$$g_{o,PE} = -\frac{\omega_o \varepsilon_o n^4}{2} \frac{\int \begin{bmatrix} E_x^* & E_y^* & E_z^* \end{bmatrix} \begin{bmatrix} pS_1 & pS_6 & pS_5 \\ pS_6 & pS_2 & pS_4 \\ pS_5 & pS_4 & pS_3 \end{bmatrix} \begin{bmatrix} E_x \\ E_y \\ E_z \end{bmatrix} dV}{\int \varepsilon |\mathbf{E}|^2 dV} \tag{5.11}$$

where:

$$\begin{bmatrix} pS_1 \\ pS_2 \\ pS_3 \\ pS_4 \\ pS_5 \\ pS_6 \end{bmatrix} = \begin{bmatrix} p'_{11} & p'_{12} & p'_{13} & 0 & 0 & p'_{16} \\ p'_{21} & p'_{22} & p'_{23} & 0 & 0 & p'_{26} \\ p'_{31} & p'_{32} & p'_{33} & 0 & 0 & 0 \\ 0 & 0 & 0 & p'_{44} & 0 & 0 \\ 0 & 0 & 0 & 0 & p'_{55} & 0 \\ p'_{61} & p'_{62} & 0 & 0 & 0 & p'_{66} \end{bmatrix} \begin{bmatrix} S_1 = S_{xx} \\ S_2 = S_{yy} \\ S_3 = S_{zz} \\ S_4 = 2S_{yz} \\ S_5 = 2S_{xz} \\ S_6 = 2S_{xy} \end{bmatrix} \tag{5.12}$$

Normalized electric field (E_y) and mechanical displacement profiles (xz-plane) of the final optimized diamond OMC design are shown in Figure 5.21 (b) and (c), respectively. The optimized design – which assumes x-axis orientation aligned with the in plane [110] crystallographic direction – has an optical resonance at $\omega_o/2\pi$ = 195 THz (λ_o = 1539 nm), radiation-limited optical Q-factor of 1.02 x 10^6, mode volume of $0.75(\lambda/n)^3$, mechanical resonance at $\omega_m/2\pi$ = 6.11 GHz, effective mass of 607 fg, and zero-point motion of x_{zpf} = 3.1 fm. The final coupling rate for this design was go/2π = 116 kHz, and included a moving boundary and photo-elastic contribution of $g_{o,MB}/2\pi$ = 53 kHz and $g_{o,PE}/2\pi$ = 63 kHz, respectively.

5.2 FABRICATED DIAMOND OPTOMECHANICAL CRYSTALS

Fabrication of diamond OMCs utilized angled-etching techniques [130] (described in Chapter 2). The final fabricated structures, displayed in Figure 5.5 (a) to (c), reveal excellent reproduction of the intended design. Evidently, a unique consideration of angled-etched structures is their triangular cross-section symmetry [130, 132]. For instance, uneven sample mounting during the angled-etching step or diamond substrate wedge tolerances will lead to a distribution of effective etch angles across the sample, breaking symmetry in the final device cross-section. Because of such asymmetry, localized mechanical and optical cavity modes will inevitably couple to anti-symmetric guided modes, which exist in their respective quasi-bandgaps, bringing about potentially significant loss. To circumvent this, periodic sample rotation was implemented during angled-etching to average the effective etch angle across the substrate.

We investigated this problem further by stamping angled-etch diamond optomechanical crystals onto a smooth silver-coated silicon wafer (discussed previously in Chapter 2). High-resolution SEM images shown in Figure 5.6 (a) and (b), respectively, reveal diamond OMCs (oriented upside down) fabricated without and with sample rotation during angled-etching, with insets displaying a tilted cross-sectional view. Sample rotation appears to reduce the degree of asymmetry (defined as the offset in the bottom apex of the triangular cross-section from its centerline) considerably. However, even minimal asymmetry significantly reduces the simulated optical and mechanical Q-factors, as illustrate in Figure 5.6 (c) and (d) respectively, depending on the in-plane orientation of the device relative to the [100] crystal direction. Optical Q-factors of asymmetric diamond OMCs were performed by FDTD simulations (Lumerical Solutions, Inc.), while mechanical Q-factors were simulated by FEM simulations (COMSOL) using

previously described techniques [180]. Interestingly, symmetry breaking in devices with their x-axis is oriented along the [110] crystal direction couple more weakly to guided modes of antisymmetric character, and thus, are likely more robust to fabrication imperfections (beyond cross-sectional asymmetry alone). Therefore, fabricated diamond optomechanical crystals characterized in this work were oriented along the [110] crystallographic direction.

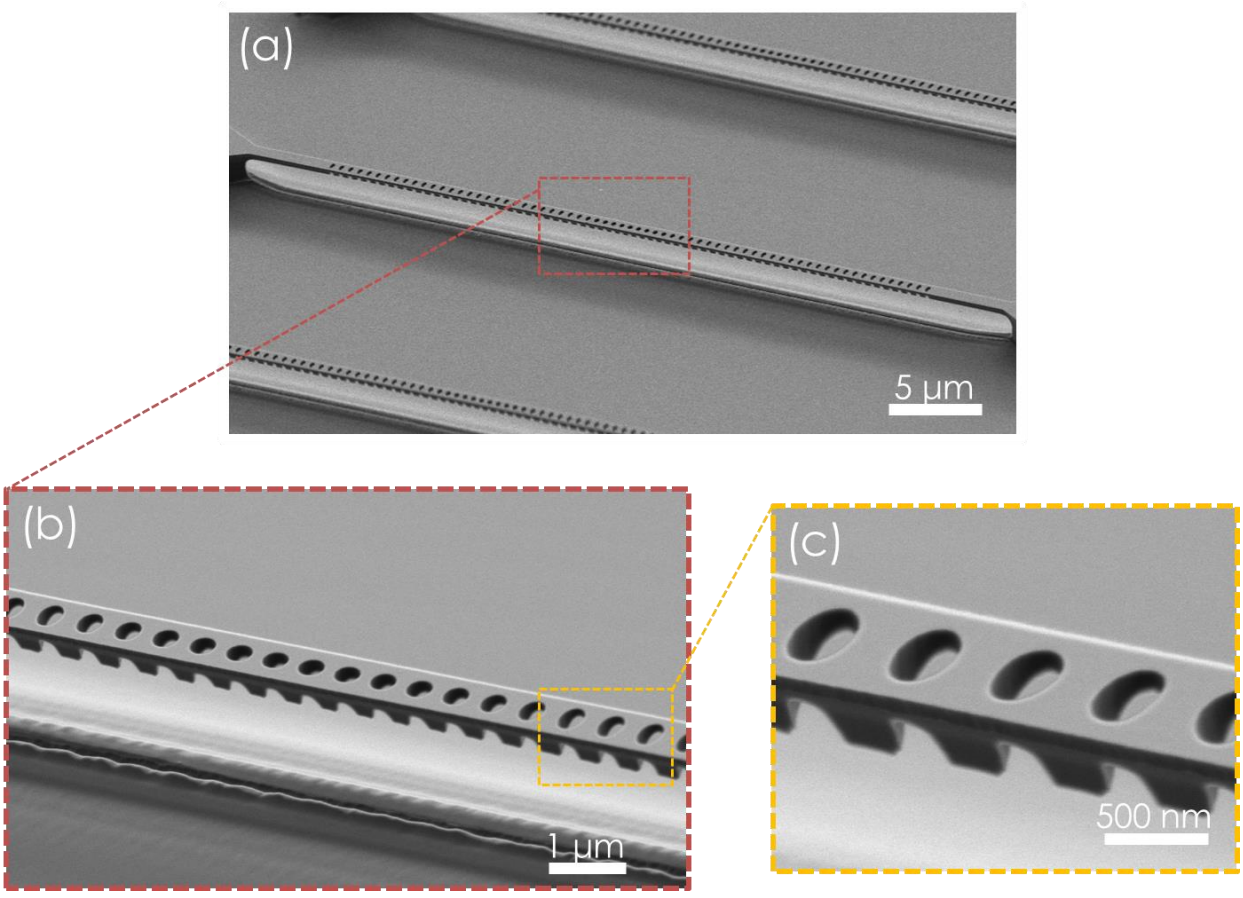

Figure 5.5 | Fabricated diamond optomechanical crystals. SEM images of **(a)** a fabricated diamond optomechanical crystal, **(b)** zoomed in view of the defect region, and **(c)** high-resolution image of fabricated air holes comprising the Bragg mirror region. **(d)** SEM image of an (inverted) diamond optomechanical crystal, liberated from the diamond substrate via stamping on a silver-coated silicon wafer. Inset shows a tilted (60º) SEM image of a broken diamond optomechanical crystal, revealing the triangular cross-section.

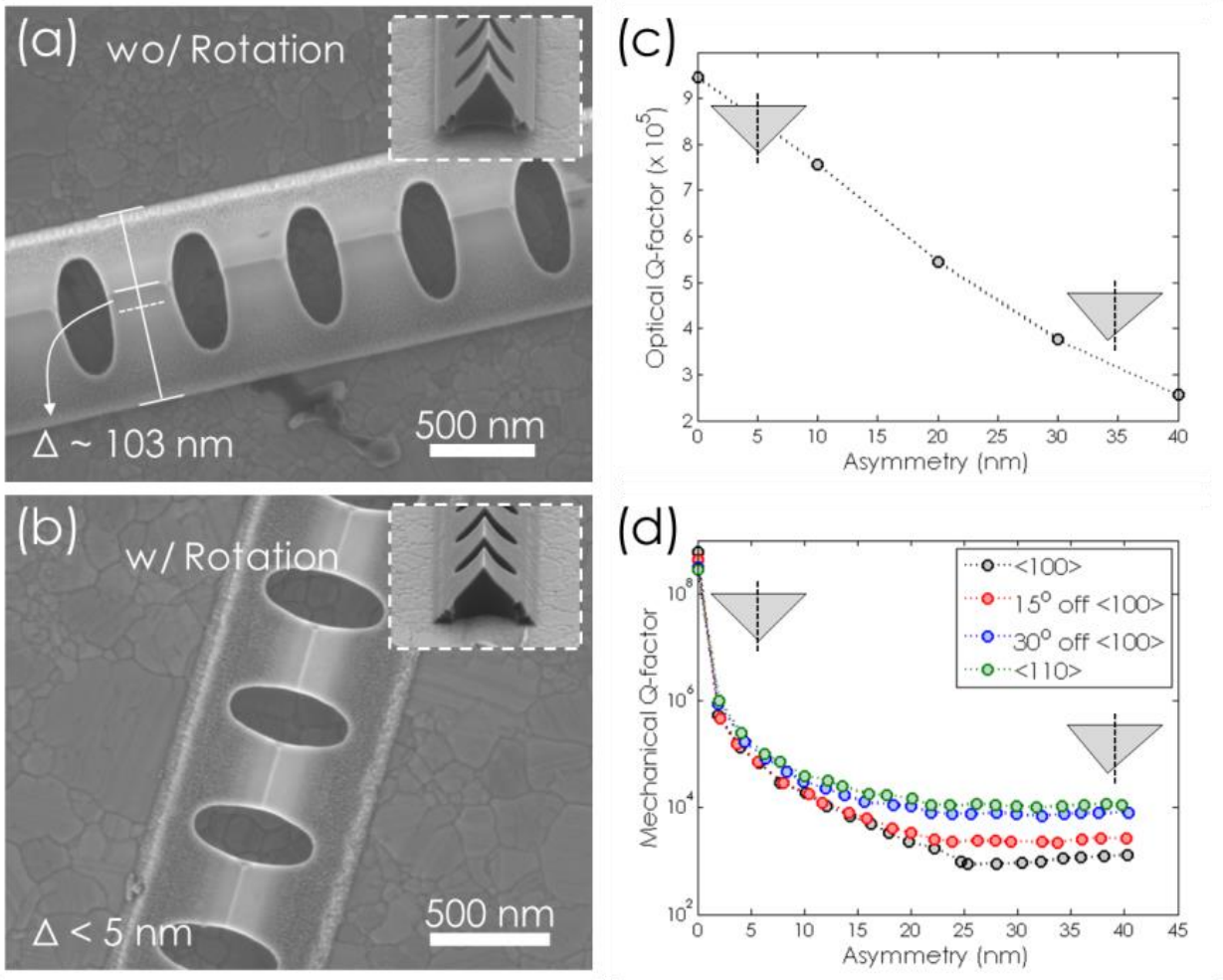

Figure 5.6 | Fabricated diamond optomechanical crystal cross-sectional symmetry. High resolution SEM images of the backside of diamond optomechanical crystals fabricated **(a)** without and **(b)** with sample rotation during angled-etching. A significant improvement in the cross-section asymmetry (Δ) is observed. Insets tilted SEM images of broken diamond nanobeams, revealing the diamond optomechanical crystal cross-section. The influence of cross-sectional asymmetry on the optical and mechanical Q-factors (as a function of in-plane nanobeam orientation with the major crystallographic directions) is plotted in **(c)** and **(d)** respectively. Optical Q-factor simulations were performed using finite difference time domain simulations, while mechanical Q-factor simulations were performed by finite element method using previously described techniques [180].

5.3 OPTICAL AND MECHANICAL MODE SPECTROSCOPY

A normalized optical transmission spectrum – characterization set up shown in Figure 5.7 (a) – of a representative diamond OMC with its resonance at λ_o = 1532.6 nm ($\omega_o/2\pi$ = 196 THz), is shown in Figure 5.7 (b). Characterization of fabricated diamond OMCs, performed under ambient conditions, used a dimpled fiber taper (schematically displayed in Figure 5.7 (a)) to evanescently couple to the device under test (as illustrated by the optical micrograph included as the inset). A tunable telecom laser diode (New Focus Velocity TLB-6328, C-band) was used locate the optical cavity resonance. A small percentage of the input laser sent to a wavelength meter (λ-meter) via a 90:10 coupler (BS) enabled a stabilized laser frequency position. For measurements displayed in Figure 3, the laser was coupled directly to a variable optical attenuator (VOA), while high power measurements displayed in Figure 4 used an erbium doped fiber amplifier (EDFA) to boost the input power. A tunable filter placed after the EDFA removed the majority of amplified spontaneous emission (ASE) from the transmitted signal. After the VOA, the laser light was first sent through a fiber polarization controller (FPC) to maximize coupling with the device under test, and then into the dimpled fiber taper. The dimpled fiber taper position with respect to the device under test was precisely controlled via motorized stages with 50 nm encoder resolution. Optical scans of the device under test were initially collected with the dimpled fiber taper hovering above the device, to evaluate the optical cavity parameters under weak fiber coupling. For final measurements, the dimpled fiber was placed in direct contact with the device under test, in a position such as to maximize coupling while minimizing parasitic losses due to dielectric loading of the cavity by the silica fiber taper. A 2 x 2 fiber switch (SW2) was used to control the direction of light through the device region and allow for precise calibration of insertion and bidirectional coupling losses. After passing the device, the

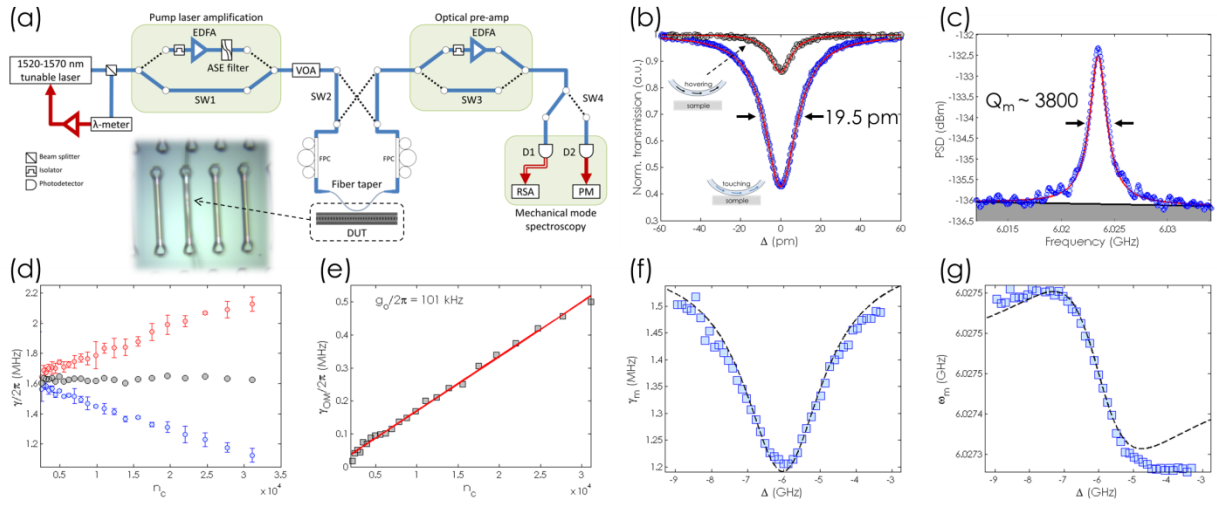

Figure 5.7 | Optical and mechanical mode spectroscopy. (a) Schematic of the fiber-optical set up for optical and mechanical mode spectroscopy (see *Methods* for description of symbols), with an optical micrograph of the dimpled fiber taper in contact with the diamond optomechanical crystal device under test. **(b)** Normalized optical transmission spectrum, centered at λ_o = 1532.4 nm ($\omega_o/2\pi$ = 196 THz), of a diamond optomechanical crystal measured with the dimpled fiber taper hovering (black circles) and touching (blue circles) the device, with corresponding Lorentzian fits indicated by solid red lines. With the dimpled fiber taper in contact with the device, the Lorentzian fit yields an optical linewidth of 19.5 pm and ~ 57% on-resonance transmission, corresponding to a measured total and intrinsic optical Q-factor of 7.85 x 10^4 and 1.20 x 10^5, respectively. **(c)** Optically transduced power spectral density of the fundamental 'flapping' mode at $\omega_m/2\pi$ = 6.023 GHz. Note, this mechanical spectrum was collected at low input laser powers and reveals the thermal Brownian motion of the cavity. The Lorentzian fit, indicated by the solid red curve, estimates a mechanical Q-factor of ~ 3800. **(d)** Measured mechanical linewidth (γ) collected at laser detuning of $\Delta = +\omega_m$ (red circles) and $\Delta = -\omega_m$ (blue circles). Black circles indicate the intrinsic mechanical linewidth values (γ_i) obtained by taking the average of the detuned data. An average value of $\gamma_i/2\pi$ = 1.63 +/- 0.012 MHz is estimated from the plot. **(e)** The optomechanically induced damping (γ_{OM}, black squares), calculated by subtracting γ_i from the blue-detuned mechanical linewidths, plotted versus intracavity photon number. A linear fit (red line) yields $g_o/2\pi$ = 101 kHz. The **(f)** optically amplified mechanical loss rate and **(g)** optical spring shifted mechanical frequency measured as a function of laser frequency blue detuned from the cavity, at an constant intercavity photon number of n_c = 2.5 x 10^4. Fits to **(f)** and **(g)** yield $\gamma_i/2\pi$ = 1.60 MHz and $g_o/2\pi$ = 102 kHz, consistent with values estimated from mechanical linewidths versus intercavity photon number.

transmitted signal was switched between a low speed and high speed path, in order to collect the optical cavity spectrum and mechanical cavity spectrum respectively. In the high speed path, transmitted laser light is optically amplified by a second EDFA and then detected by a high-speed photodetector (D1, New Focus 1554-B, 12 GHz bandwidth). The high speed detector is connected to a real-time spectrum analyzer (RSA) to measure photocurrent electronic power spectrum and monitor the mechanical cavity response. In the low speed path, transmitted laser light is sent to a nanosecond photodetector (D2) used to measure the DC transmission response of the optical cavity.

A Lorentzian fit to the optical cavity resonance gives a measured total and intrinsic optical Q-factor of 7.85 x 10^4 and 1.20 x 10^5, respectively. The corresponding total cavity decay rate, fiber taper coupling rate, and intrinsic optical decay rate are $\kappa/2\pi$ = 2.49 GHz, $\kappa_e/2\pi$ = 0.86 GHz, and $\kappa_i/2\pi$ = 1.63 GHz, respectively. With the expected diamond OMC mechanical resonance at ~ 6 GHz, the optical cavity decay rate places the optomechanical system into the resolved sideband regime, with $\omega_m/\kappa \sim 2.42$. In this regime, while the input laser is either red- or blue-detuned from the optical cavity position by a mechanical frequency ($\Delta = (\omega_o - \omega_l) = \pm \omega_m$), mechanical motion of the acoustic mode modulates transmitted light, giving rise to a sideband of the input laser resonant with the optical cavity. The other first-order motional sideband (which is not resonant with the optical cavity) is suppressed in this scenario. As a result, mechanical motion produces an intensity modulation in the radio frequency (RF) power spectrum of the photodetector. The RF spectrum of thermally excited mechanical mode at room temperature (i.e., thermal Brownian motion) is shown in Figure 5.7 (c), and reveals a Lorentzian mechanical resonance of the diamond OMC centered at $\omega_m/2\pi$ = 6.023 GHz with a $Q_m \sim 3800$. This corresponds to a $f \cdot Q$ product of ~ 2.3 x 10^{13} Hz, which is among the highest demonstrated for either a bulk or small-scale diamond mechanical oscillator at room temperature [16, 80, 86, 183].

With the aforementioned laser detuning conditions, optomechanical backaction causes an additional damping rate in the resolved-sideband limit [184]:

$$\gamma_{OM} = \mp 4 n_c g_o^2 / \kappa \tag{5.13}$$

for $\Delta = \pm \omega_m$, where n_c is the intracavity photon number, calculated from the input laser power (P_i) by the relation:

$$n_c = P_i \left(\kappa_e / 2\hbar\omega_l \left((\kappa/2)^2 + \Delta^2 \right) \right) \tag{5.14}$$

Figure 5.7 (d) plots a series of mechanical linewidth taken with both red- and blue-sideband laser detuning as a function of input power, to the maximum output of the laser (n_c ~ 31,000 photons). The effects of backaction are clearly visible, and from the mean value extracted from γ_{red} and γ_{blue} data points, the estimated intrinsic mechanical linewidth is γ_i = 1.63 +/- 0.01 MHz. The optomechanical coupling rate, calculated as $\gamma_{OM} = \gamma_i - \gamma_{blue}$, is plotted versus n_c in Figure 5.7 (e), where a linear fit yields a single-photon optomechanical coupling rate of $g_o/2\pi$ = 101 kHz. This estimate differs only slightly from our design, which we attribute to uncertainty in the photo-elastic constants of diamond at telecom frequencies. To verify our estimate of γ_i and g_o, the laser frequency was first blue-detuned and then swept between $\Delta = \omega_m \pm \kappa$ while maintaining a constant n_c, thus tracing the optically amplified mechanical damping rate (Figure 5.7 (f)) and the optical spring shifted mechanical frequency (Figure 5.7 (g)). Fits to this data followed expressions for the optical springing and damping terms [184], given by:

$$\delta\omega_m = \left| G^2 \right| \mathrm{Im}\left[\frac{1}{i(\Delta - \omega_m) + \kappa/2} - \frac{1}{-i(\Delta + \omega_m) + \kappa/2} \right] \tag{5.15}$$

and

$$\gamma_{OM} = 2\left|G^2\right| \mathrm{Re}\left[\frac{1}{i(\Delta - \omega_m) + \kappa/2} - \frac{1}{-i(\Delta + \omega_m) + \kappa/2}\right] \tag{5.16}$$

These fits yielded a second estimate of γ_i = 1.60 MHz and g_o = 102 kHz, in close agreement with the previously stated values. A static thermal softening of the diamond material likely causes the slight deviation of data in Figure 5.7 (g) from a pure radiation-pressure driven back-action optical spring effect. As the detuning approaches zero and the laser enters the cavity resonance, the diamond OMC temperature is raised due to non-negligible linear optical absorption, resulting in thermal expansion and a reduction in Young's modulus [185].

5.4 HIGH POWER OPTOMECHANICAL TRANSDUCTION AND PHONON LASING

To drive γ_{OM} beyond the level reached with the tunable laser output alone, an erbium doped fiber amplifier (EDFA) was inserted after the pump laser to enable large n_c. Figure 4 (a) plots the mechanical linewidth at high input powers, with the laser blue-detuned by a mechanical frequency, while Figure 4 (b) plots corresponding cooperativity values, $C = \gamma_{OM}/\gamma_i$, calculated with the previously determined γ_i. At an input power corresponding to approximately $n_c \sim 10^5$, the diamond OMC reached C ~ 1, exciting the mechanical cavity into large amplitude optomechanical self-oscillations, so-called "phonon lasing" [178].

Mechanical spectra of the diamond OMC taken below, at, and above this phonon lasing threshold (shown in Figure 5.8 (c)) show an over 60 dB increase in peak amplitude, with a threshold input power of $n_{c,thr} \sim 10^5$.

For a second diamond OMC device, a similar measurement scheme was carried out, with n_c increased beyond the observed phonon lasing threshold. The relevant parameters experimentally extracted for this device (λ_o Q_i, $\kappa/2\pi$, $\omega_m/2\pi$, $\gamma_i/2\pi$, $g_o/2\pi$) = (1544.5 nm, 1.54 x 10^5, 2.62 GHz, 6.13 GHz, 1.74 MHz, 106 kHz), yielded a $n_{c,thr} > 9.0 \times 10^4$ (as represented by the vertical dashed blue line in Figure 5.8 (e)). By increasing n_c beyond this value with the laser tuned to the red motional sideband, a final cooperativity value $C \sim 1.8$ was reached at an optical cavity occupation of $n_c \sim 1.7 \times 10^5$ photons (see Figure 5.8 (f)). Beyond this input power level, thermal-optic bistability shifts (likely originating from surface absorption) made it difficult to achieve precise laser detuning equal to the mechanical frequency, resulting in measured mechanical linewidths that deviate from the linear fit of the data. This established a second maximum power threshold ($n_{c,max}$), indicated by the vertical dashed grey line. In relation to previous reported limits, diamond OMCs have an intracavity photon capacity over twice as large as OMC structures realized in silicon nitride [172, 173].

With this result, we have demonstrated resolved sideband cavity-optomechanics in single-crystal diamond, where optomechanical coupling via radiation pressure was sufficient to exceed a cooperativity of ~ 1 for an intracavity photon population on the order of 10^5. Present devices also offer a promising platform for reaching much larger cooperativities when, for instance, operated at cryogenic temperatures, where mechanical Q-factors of diamond resonators have been shown to improve significantly [80]. Moreover, incorporating diamond color centers with monolithic OMCs is an interesting route to applications in quantum-nonlinear optomechanics. Diamond is rich in optically active defects (color centers), such as the nitrogen-vacancy (NV) center, which behave as atom-like systems in the solid state [40]. Recent experiments [84-88] exploring coherent coupling of the NV electronic spin to phonons in

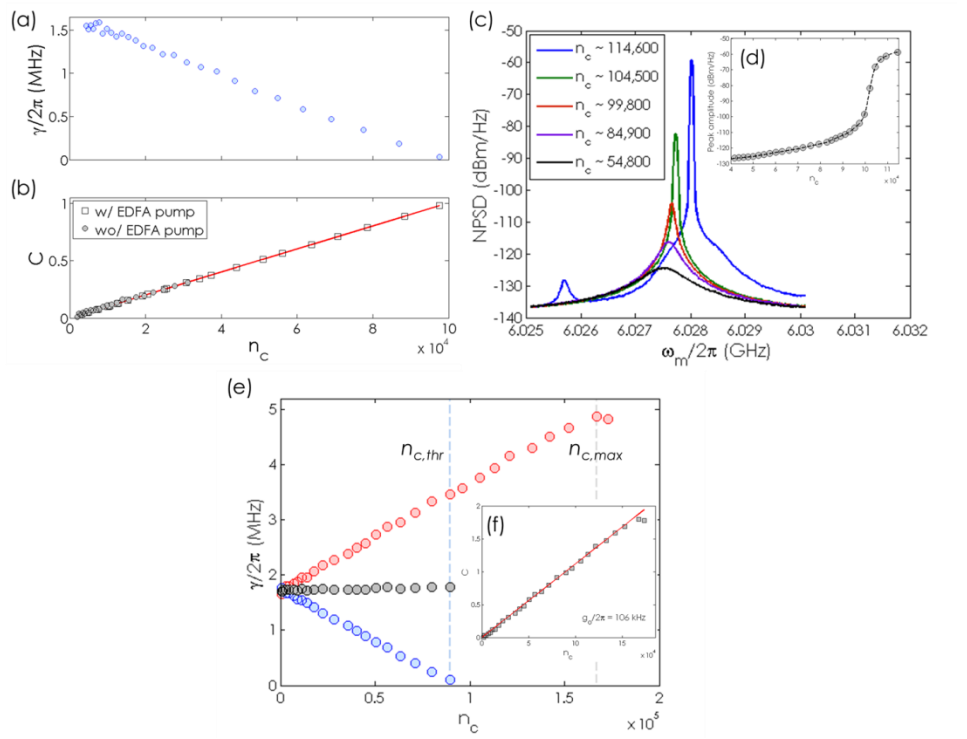

Figure 5.8 | High power optomechanical transduction and phonon lasing. **(a)** Measured mechanical linewidths and **(b)** corresponding cooperativity values collected with the amplified pump laser resonant with the blue detuned motional sideband ($\Delta = -\omega_m$), as a function of intracavity photon number (n_c). Data points collected with (open squares) and without (black circles) the amplified pump laser are included. Note, the cooperativity values measured without the amplified pump were calculated using γ_{OM} data plotted in Figure 3 (e), using the previously measured intrinsic mechanical linewidth, $\gamma_i/2\pi \sim 1.63$ MHz. **(c)** Noise power spectral densities (NSPD) collected below, at, and above the input power threshold for phonon lasing. The large shoulder feature and small satellite peak in the above-threshold mechanical spectrum correspond to beating of the phonon laser line with low-frequency modes of the nanobeam structure. The inset **(d)** plots the peak NSPD amplitude versus input optical power, indicating the intracavity photon threshold for phonon lasing is at $n_c \sim 10^5$. **(e)** Measured mechanical linewidths (γ) collected at laser detuning of $\Delta = +\omega_m$ (red circles) and $\Delta = -\omega_m$ (blue circles) as a function of input photon number for a second diamond optomechanical crystal device. Black circles indicate the intrinsic mechanical linewidth values (γ_i) obtained by taking the average of the detuned data, up to the phonon lasing threshold, $n_{c,thr}$ (indicated by the vertical blue dashed line). An average value of $\gamma_i/2\pi = 1.74$ MHz is estimated from the plot for this device. The onset of thermo-optically induced bistability shifts of the cavity resonance due to high intracavity photon population is indicated in **(f)** by the vertical grey dashed line. The inset shows the corresponding optomechanical cooperativity ($C = \gamma_{OM}/\gamma_i$, black squares) plotted versus intercavity photon number. A linear fit (red line) to the cooperativity values yields $g_o/2\pi = 106$ kHz for this device.

mechanical resonators via lattice strain have demonstrated manipulation of the NV spin state at large driven mechanical amplitudes, but remain far below the strong spin-phonon coupling regime. One way to boost this interaction would be to engineer truly nanoscale resonators, with feature sizes of a few hundred nm, and with frequencies in the hundreds of MHz to few GHz range – such mechanical modes would provide a large change in local strain per phonon [88]. The localized phononic modes of OMCs not only satisfy these requirements [186], but also are conveniently actuated and transduced with optical fields in the well-established telecom wavelength range. Diamond OMCs with integrated color centers may ultimately be used to map non-classical spin qubit states as well as quantum states of light onto phonons and vice-versa [89], and will enable fundamentally new ways to prepare, control, and read out the quantum states of diamond qubits. Lastly, individual diamond OMCs integrated into larger arrays coupled through phononic waveguides [187] could enable long-range spin-spin interactions mediated by phonons [188].

Chapter 6

Outlook

With the angled-etching nanofabrication scheme presented in this thesis, we have shown single-crystal diamond to be a viable nanophotonics platform, which will enable further breakthroughs in both classical and quantum optics. For instance, when fabricated around spectrally stable color centers, diamond nanobeam cavities will enable large enhancement of zero-phonon line emission via the Purcell effect, as well as efficient collection of emitted photons. As well, monolithic single-crystal diamond nanophotonic structures are ultimately compatible with post-growth color center incorporation techniques (high energy implantation) and post processing techniques needed to stabilize implantation-defined color centers, which often include high temperature (~ 1200^{o}C) annealing [124-126]. In this outlook chapter, we describe recent experiments [189] conducted by the team of A. Sipahigil, R.E. Evans, and D.D. Sukachev, which we have collaborated with to realize efficient coupling of a SiV^{-}color center to a diamond nanophotonic device fabricated by angled-etching. In this work, SiV^{-} centers are deterministically positioned in fabricated diamond nanobeam cavities via targeted silicon implantation, followed by high temperature annealing. Substantial attenuation of resonant optical transmission by individual SiV^{-} centers is observed, with the resonant scattering saturating at less than one photon per system's bandwidth. This result represents an important step forward to the realization of fully integrated, scalable nanophotonic quantum devices.

6.1 SILICON VACANCY CENETERS COUPLED TO DIAMOND NANOBEAM CAVITIES

The SiV^- color center in diamond [55] boasts a unique set of properties for solid-state emitters. Specifically, its optical transitions are consistently near lifetime-broadened and the inhomogeneous distribution of an ensemble can be on the order of the lifetime-limited linewidth [59]. These properties originate from the inversion symmetry of the SiV^- center, which results in a vanishing permanent electric dipole moment for the SiV^- orbitals and a reduced sensitivity to external electric fields [60]. Optical transitions of the SiV^- center are therefore protected from the charge dynamics in the solid-state environment that in typical systems result in broadened inhomogeneous distributions and spectral diffusion [190, 191]. This allows for integration of SiV^- center in nanostructures while maintaining their spectral stability [61, 126].

To leverage the robust optical transitions of the diamond SiV^- center, individual emitters are deterministically positioned inside diamond nanobeam cavities fabricated by angled-etching (see Chapter 4) with small mode volumes and large quality factors. Fabricated diamond nanobeam cavities (shown in Figures 6.1 (a) and (d)) consist of an anchor for mechanical support, a notch for free space-waveguide coupling, a waveguide section (no holes) on each side and a cavity defined by a gradually tapered set of holes. The cavity is designed [189] such that the cavity photons decay predominantly to the waveguide and the system has high transmission on resonance (see Appendix B for more details). To characterize the mode volumes of the diamond nanobeam cavities, a diamond substrate with a high and uniform density of SiV^- centers across the nanocavity was studied. The cavity mode profiles in such samples were experimentally measured by monitoring the SiV^- center fluorescence rate into the waveguide mode as a 700 nm excitation laser was spatially scanned across the nanocavity. The resulting emission rates are shown in Figure 6.1 (c), for the cases when the fundamental (blue), and second order (red) mode of the

cavity were tuned on resonance with the SiV^- center ensemble (achieved by gas condensation tuning). In this approach, the photon detection rate is proportional to the local intensity of the cavity mode resonant with the SiV^- center ensemble. Using this technique, we infer a cavity mode volume of $V \sim (\lambda/n)^3$ for the fundamental mode used in the experiment [189].

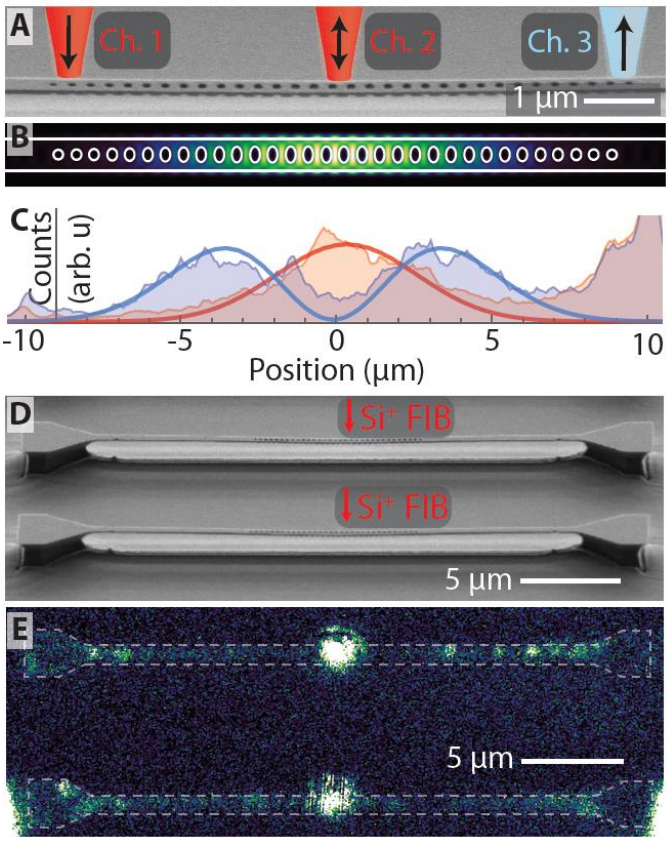

Figure 6.1 | Diamond nanocavities with deterministically positioned SiV^- centers. (a) SEM image of nanophotonic crystal cavity and **(b)** simulated energy density profile of the cavity mode. **(c)** Experimental measurement of the cavity mode profile using a high and uniform density SiV^- sample. Fluorescence in the waveguide mode (Ch. 3) is monitored as the excitation laser is spatially scanned across the nanocavity for first- (red) and second-order (blue) cavity resonances tuned to the SiV^- transition. (d) After cavity fabrication, SiV^- centers are deterministically positioned at the center of each cavity using focused Si^+ ion beam implantation. (e) Fluorescence image using resonant excitation demonstrates near-resonant SiV^- creation at the center of multiple cavities. Figure adapted with permission from Ref. [189].

To obtain optimal coupling between the individual quantum emitter and the cavity mode in the integrated devices, the emitters are positioned at a field antinode using a focused Si^+ ion beam to implant Si at the center of the cavity as shown in Figure 6.1 (c). The targeted implantation was followed by annealing of the sample at ~ 1175 ^oC in ultra-high vacuum to form SiV^- defects and mitigate crystal damage from fabrication and implantation steps [124-126]. Targeted Si^+ implantation allows arbitrary three-dimensional positioning of the emitters inside the cavity with sub-wavelength (close to ~ 40 nm) accuracy [189], in a highly flexible process that also allows for control over the isotope and number of implanted Si ions. Unlike approaches where nanophotonic structures are fabricated around pre-characterized or randomly positioned solid-state emitters [167, 192, 193], targeted implantation allows scalable fabrication of thousands of SiV^--cavity nodes on a single diamond sample. As an example, Figure 6.1 (d) and (e) show an SEM with corresponding fluorescence image using a narrowband resonant excitation laser at frequency 406.706 THz. The observation of SiV^- center fluorescence in different nanostructures demonstrates the presence of near resonant emitters in all SiV^--cavity nodes. A three-channel confocal microscope is used to characterize the response of the coupled SiV^--cavity system. Using a high numerical aperture (NA = 0.95) objective, three spatially separated optical beams are focused on the nanostructure (as illustrated in Figures 6.1 (a)) and are used, respectively, to excite the waveguide mode (Ch. 1), to detect fluorescence and control the SiV^- center (Ch. 2), and to detect transmission (Ch. 3). The excitation laser frequency (v) is scanned across the SiV^- resonance (v_o) while we monitor the transmission and fluorescence field intensities (Figure 6.2 (a)). Three peaks are observed in fluorescence, corresponding to three SiV^- centers in a single cavity [189]. Each of these three resonances results in strong extinction of the cavity transmission indicating that all three SiV^- centers couple to the cavity mode.

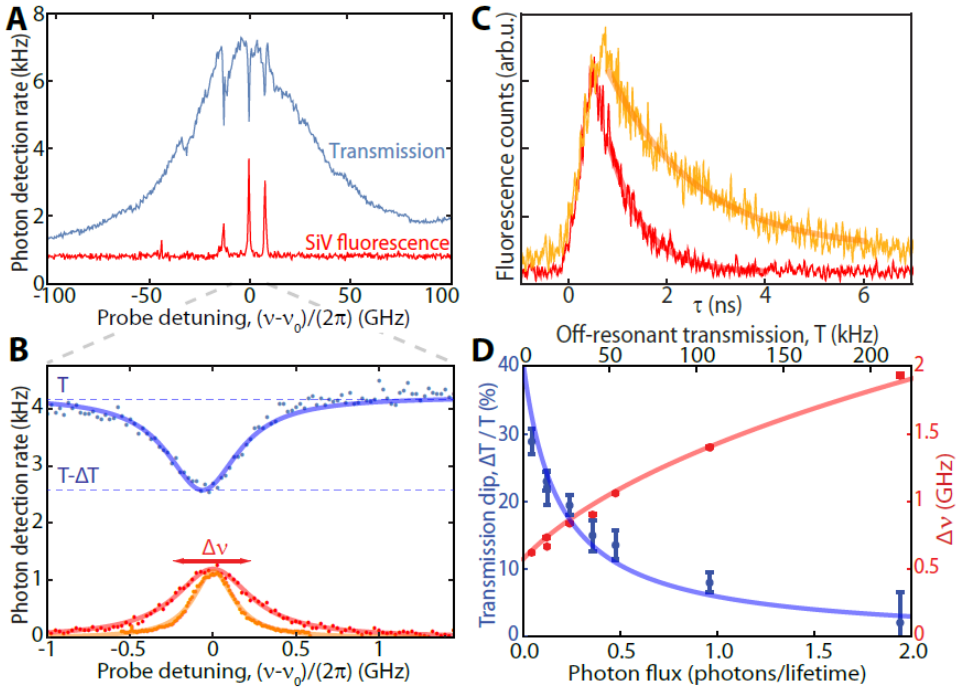

Figure 6.2 | Response of the coupled SiV⁻-cavity system. (a) Transmission (blue) and SiV⁻ fluorescence (red) are simultaneously measured as the excitation laser frequency, ν, is scanned across the SiV⁻ resonance at $\nu_o/2\pi$ = 406.706 THz. Three SiV⁻ centers are resonantly coupled to the cavity, resulting in suppressed transmission at the corresponding frequencies. (b) Optical transition linewidths with the cavity detuned (orange) and on resonance (red) with the atomic transition. On resonance, the transition is radiatively broadened from 298(5) to 590(30) MHz (c) with a corresponding lifetime reduction from 1.8(1) to 0.6(1) ns due to the enhanced radiative decay. A single SiV⁻ center results in strong extinction, ΔT/T = 38(3) %, in transmission. (d) Transmission and fluorescence response is nonlinear at the level of a single-photon per emitter lifetime. Atomic saturation at the single-photon level power broadens fluorescence (increased Δν) and reduces ΔT/T. Figure adapted with permission from Ref. [189].

The strength of the SiV⁻-cavity coupling can be directly evaluated using the data presented in Figures. 6.2 (b) and (c). When the cavity is off-resonant with the emitter, the transition linewidth is γ = 298(5) MHz and the excited state has a lifetime of τ_e = 1.8(1) ns (yellow curves in Figures 6.2 (b) and 6.2 (c)). This is close to the lifetime-broadening limit with additional non-radiative broadening likely due to a combination of finite-temperature effects [64] and residual spectral diffusion. When the cavity is tuned on resonance, the optical transition linewidth is radiatively broadened to 590(30) MHz with a corresponding

reduction in lifetime τ_e as shown by the red curves in Figures 6.2 (b) and (c). At the same time, we find that a single SiV^- center results in $\Delta T/T = 38(3)$ % extinction of the probe field in transmission. Based on the radiative broadening shown in Figure 6.2 (b), we infer a cooperativity of $C = 4g^2/\kappa\gamma \sim 1$ for the SiV^--cavity system with cavity QED parameters $(g, \kappa, \gamma) = 2\pi(2.1, 57, 0.30)$ GHz. This cooperativity estimate is consistent with the transmission extinction measured in Figure 6.2 (b) when effects associated with the multi-level structure of SiV^- are accounted for [189]. To probe the nonlinear response of the system, the experiment in Figure 6.2 (b) was repeated at increasing probe intensities. As expected, we find that the atomic and system transmission response saturates at a level less than a single-photon per emitter lifetime (Figure 6.2 (d)), resulting in power broadening in fluorescence ($\Delta\nu$) and reduced extinction in transmission ($\Delta T/T$) [189, 194].

Having demonstrated an efficient interface between photons and a coherent solid-state quantum emitter, this SiV^--cavity coupled system was also used to implement a quantum optical switch controlled by switching the metastable state of an individual SiV^- with an optical field. Photon correlation measurements were used to verify optical switching at a single photon level [189]. These observations open up unique possibilities for realizing scalable systems involving multiple emitters strongly coupled to nanoscale cavities with a number of potential applications in quantum information processing, quantum nonlinear optics and quantum communication. Specifically, efficient generation of indistinguishable single-photons with GHz bandwidth, realization of deterministic two-photon gates [195] and photonic Bell-state analyzers [196] become possible in an integrated solid-state platform. Moreover, systems involving multiple emitters per cavity as well as multiple atom-cavity nodes can be realized using our deterministic fabrication approach. Our observations in Figure 6.2 (a) already demonstrate that strong coupling of three emitters to the same cavity mode is possible. This, coupled with further advances in photon collection efficiency (such as that demonstrated in Chapter 4) and improved diamond nanobeam cavity design and fabrication, will ultimately yield fully integrated, scalable quantum photonic networks.

Appendix A

Diamond one-dimensional photonic crystal "nanobeam cavity" design

The one dimensional diamond photonic crystal cavity structure (referred to simply as "nanobeam cavity") discussed in Chapter 4 was conceived using previously developed design principles [153, 154]. Our nanobeam cavity design consists of a triangular cross-section diamond waveguide perforated with a chirped lattice of elliptically-shaped air holes. The base triangular cross-section unit cell (Figure B.1 (a)), is parameterized by the etch angle (θ), width (w), lattice constant (a), and major and minor elliptical air hole diameters (d_z, d_x). Note, based on optimized fabrication processes (see Chapter 2), the unit cell etch angle (designated as the semi angle at the bottom apex of the triangular cross-section) was fixed at either $\theta = 35^o$ or $\theta = 50^o$ in our design.

Figure A.1 (b) displays a representative photonic bandstructure for a nominal unit cell with $\theta = 50^o$ and (a, w, d_z, d_x) = (260, 470, 140, 140) nm. Here, quasi-transverse electric (TE-like, solid black lines) and quasi-transverse magnetic (TM-like, dashed blue lines) guided modes exist below a continuum of leaky and radiation modes bounded the light line (grey shaded region), and give rise to symmetry based bandgaps sufficient to realize highly localized resonances. In our convention, the TE-like modes have odd vector symmetry with respect to the reflection across the $y = 0$ longitudinal symmetry plane of the nanobeam (see Figure B.1 (a) for coordinate conventions). With the chosen unit cell dimensions, a large TE-like bandgap spanning ~ 390 to 460 THz exists (indicated by the pink shaded region in Figure A.1).

Therefore, these particular unit cell dimensions are suitable for localizing TE-like cavity modes at visible wavelengths.

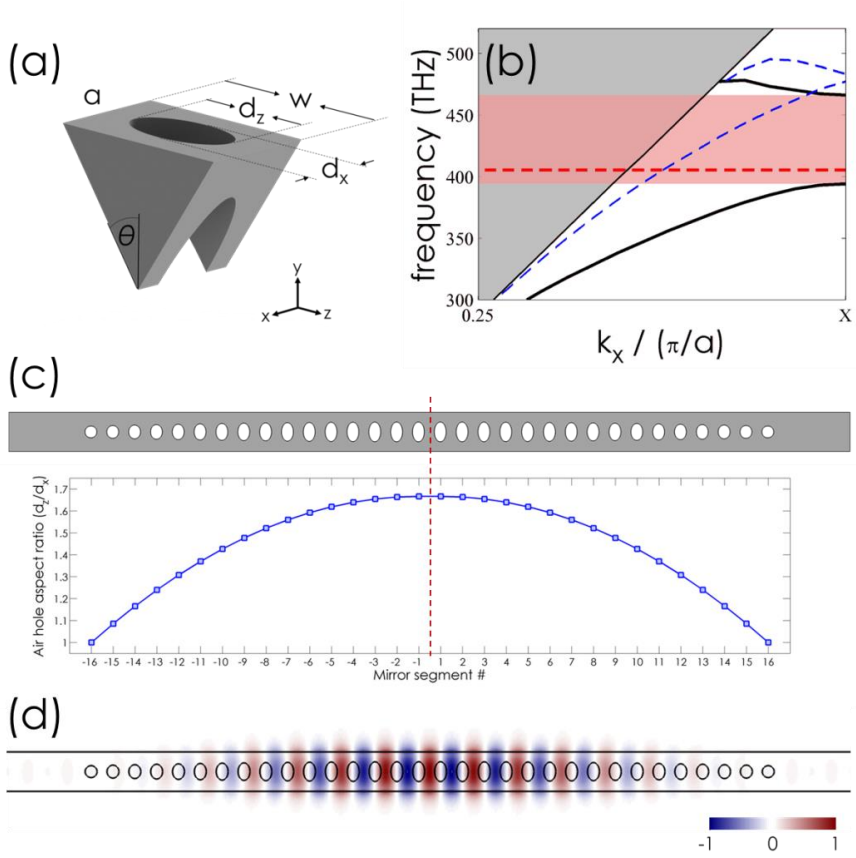

Figure A.1 | Diamond nanobeam cavity design. (a) Schematic representation of a nominal triangular cross-section diamond unit cell as fabricated by angled-etching. The unit cell is parameterized by the etch angle (θ), width (w), lattice constant (a), and major and minor elliptical air hole diameters (d_z, d_x). Corresponding (b) photonic bandstructure of a nominal unit cell with $\theta = 50^o$ and (a, w, d_z, d_x) = (260, 470, 140, 140) nm. In (b), the grey shaded region indicates the continuum of radiation and leaky modes that exist above the light line for the structure. Below the light line, supported transverse electric (TE-like) and transverse magnetic (TM-like) guided modes are indicted by solid black and dashed blue lines, respectively. A quasi-bandgap based on symmetry for the TE-like guide modes is indicated by the pink shaded region. (c) Schematic of the air hole 16-hole array cavity design with the air hole aspect ratio (d_z/d_x) plotted as a function of mirror segment number. (d) Normalized optical E_y field profile of the fundamental localized cavity mode of diamond nanobeam cavity design in (c). The fundamental cavity resonance for this design with the unit cell dimensions used to calculate the photonic bandstructure in (b) is at λ_{TE} = 743 nm, designated by the dashed red line in (b).

In our design, hole-to-hole spacing ("periodicity") is kept constant throughout the lattice of air holes, and the optical cavity is localized by quadratically tapering the major elliptical air hole diameter, d_z, as depicted in Figure A.1 (c) for a 16-hole array on each side of the x-axis mirror plane. Specifically, the major elliptical air hole diameter is $d_z = d_x$ at the ends of the air hole array, and is scaled to $d_z = 1.67d_x$ at the array center. This gradual tapering gives rise to linearly increasing mirror strength (from the $x = 0$ plane outward) along the waveguide (symmetric about the cavity x-axis mirror plane), thus achieving a Gaussian-like attenuation profile of the localized cavity mode. As was demonstrated elsewhere, a Gaussian-like attenuation minimizes the spatial Fourier harmonics of the cavity mode inside the lightcone, thereby maximizing its radiation Q-factor (Q_{rad}) [154]. The total cavity loss is comprised of both radiation losses into free-space (denoted Q_{rad}) and coupling losses to the feeding waveguide (denoted Q_{wg}). Conveniently, Q_{wg} may be independently increased by simply adding more mirror segments along the waveguide.

To calculate the cavity design optical resonances and losses, we employed finite-difference time-domain methods (FDTD, Lumerical Solutions Inc.). For the unit cell dimensions used to calculate the bandstructure in Figure B.1 (a), the fundamental TE-like cavity resonance is located at λ_{TE} = 743 nm, which is designated by the dashed red line in Figure A.1 (b). By the angled-etching process, the diamond nanobeam thickness (t) is intrinsically linked to its width (w) by the etch angle (θ), via the relationship $t = w/(2\tan\theta)$. Thus, with the scale (conformal) invariance of Maxwell's equations, global scaling of the nanobeam cavity dimensions (with a fixed etch angle) results in tuning of the cavity resonance while maintaining all cavity figures of merit (i.e. Q-factor and mode volume). For this reason, we parameterized the nanobeam cavity design by the target fundamental TE-like cavity mode resonance wavelength, λ_{TE}. Diamond nanobeam cavity design parameters (as confirmed by FDTD simulations) are summarized in Table B.1 for etch angles of $\theta = 35^o$ or $\theta = 50^o$.

Table A.1 | Diamond nanobeam cavity design parameters. Design parameters parameterized by the target fundamental TE-like cavity mode resonance wavelength, λ_{TE}, as confirmed by FDTD simulations. The major elliptical air hole diameter is $d_z = d_x$ at the ends of the air hole array, and is scaled to $d_z = 1.67 d_x$ at the array center.

Etch angle (θ)	**Lattice constant (a)**	**Width (w)**	**Minor diameter (d_x)**
35^o	$0.319\lambda_{TE}$	$0.580\lambda_{TE}$	$0.174\lambda_{TE}$
50^o	$0.349\lambda_{TE}$	$0.653\lambda_{TE}$	$0.191\lambda_{TE}$

The cavity figures of merit generated from FDTD simulations were the cavity mode volume (V), and the partial optical Q-factors (Q_{rad}, Q_{wg}). From the partial optical Q-factors, the total cavity loss (Q_{tot}) is given by the relation:

$$Q_{tot} = \left(\frac{1}{Q_{rad}} + \frac{1}{Q_{wg}} \right)^{-1} \tag{B.1}$$

Additionally, the on-resonance transmission of the fundamental cavity mode was calculated by the relation [153]:

$$T = \left(\frac{Q_{tot}}{Q_{wg}} \right)^2 \tag{B.2}$$

Table A.2 summarizes the cavity figures of merit for our quadratically tapered cavity design (assuming an etch angle of $\theta = 50^o$) with an 11-hole, 16-hole, 21-hole, and 31-hole array (symmetric about the $x = 0$ mirror plane). Note, the length of air hole array has minimal effect of the location of the fundamental TE-like cavity resonance position. Since radiation losses of the fabricated structure are typically limited by scattering due to fabrication imperfections (primarily surface roughness), the number of mirror segments in the final cavity design is generally chosen to fix Q_{wg} to the same order as the Q_{tot}, thus achieving a waveguide damped cavity where the majority of optical energy leaks into the feeding diamond waveguide (preferred for integrated nanophotonic networks). With currently optimized angled-etching fabrication parameters [133], this corresponded to a cavity design with a 31-hole array for devices operating telecom frequencies, and 16-hole array operating at visible frequencies. Devices intended for operation at shorter wavelengths suffer from increased fabrication induced scattering losses and greater discrepancy between final structure and design dimensions due to limits of electron beam lithography.

Table A.2 | Diamond nanobeam cavity design figures of merit. Mode volume, partial Q-factors, and on-resonance transmission for the fundamental TE-like resonance of a diamond nanobeam cavity with an etch angle of $\theta = 50^o$, as confirmed by FDTD simulations.

Array length (#)	Mode volume (V)	Radiation losses (Q_{rad})	Waveguide losses (Q_{wg})	Total losses (Q_{tot})	On-resonance transmission (T)
31	$2.37(\lambda/n)^3$	$3.7\text{x}10^7$	$3.3\text{x}10^6$	$3.3\text{x}10^6$	83%
21	$2.06(\lambda/n)^3$	$1.9\text{x}10^6$	$6.3\text{x}10^4$	$6.1\text{x}10^4$	92%
16	$1.8(\lambda/n)^3$	$3.2\text{x}10^5$	$9.8\text{x}10^3$	$1.0\text{x}10^4$	94%
11	$2.49(\lambda/n)^3$	$5.8\text{x}10^4$	$1.5\text{x}10^3$	$1.1\text{x}10^3$	95%

Appendix B

Transmission electron microscopy study of angled-etched diamond nanobeams

In Chapter 2 (Section 2.4), the post-fabrication device inspection methods were describe, including the destructive stamping of angled-etched diamond nanobeams onto silver coated substrates. With diamond nanobeams liberated on a silver film, it is also possible to individually manipulate a nanobeam via a tungsten probe tip controlled by a micromanipulator (i.e. an Omniprobe system). Since the diamond nanobeams are already broken off from their host diamond substrate, large forces are not necessary to remove a targeted specimen. As such, diamond nanobeams were prepared for imaging in a transmission electron microscope (TEM), in order to reveal additional nanoscale aspects of the angled-etched structures. Preparation of diamond nanobeams for TEM imaging began by locating selected nanobeams under the electron probe of a dual beam SEM-FIB (Zeiss NVision) loaded with an Omniprobe system and local ion/electron assisted deposition. Next, the Omniprobe tungsten probe tip was lowered next to one edge of the structure (as seen in Figure B.1 (a)). All monitoring of the probe position was done under the electron probe, so as to not induce any crystal damage by exposure to high energy Ga^+ of the FIB. As well, extended exposure of the full nanobeam structure to the electron probe was minimized in order to avoid excess redeposition of amorphous carbon on the diamond surface. Once the tungsten probe tip was next to the diamond structure, it was used to first un-adhere the diamond nanobeam from the silver film (i.e. break the strong van der Waals interaction). Surprisingly, this required several steps as the diamond nanobeam was strongly adhered to the silver. First, the probe was used to release one side of the structure, bending it almost to ~ 15^o from the nanobeam long axis. Further bending would cause a sudden release of

the beam and it would be lost to the chamber vacuum. The second step was to bend the nanobeam from the opposite edge, again about 15°. By doing so, the full nanobeam structure would rotate and completely un-adhere from the silver, thus being free and ready to pick off by the tungsten probe tip. Without this initial manipulation, the diamond nanobeam could not be picked off and transferred to a suitable TEM lift-out grid. Though the diamond nanobeam structure is significantly deformed through bending with the tungsten probe tip, any plastic strain and dislocations introduced are likely concentrated to the small linkages at the top and bottom of the air holes, and not in the large triangular dielectric slabs in between. As well, the deformation is localized to the edges of the nanobeam and not the center, where TEM imaging can take place.

Once the diamond nanobeam was freed from the silver, it was removed entirely from the substrate by attachment to the tungsten probe tip. This was done by localized platinum deposition using electron beam assisted deposition from a metal-organic source vapor bleed into the chamber near the sample (Figure B.1 (b)). The electron beam was again used to facilitate this deposition to avoid Ga^+ beam exposure and milling of the diamond nanobeam. Once a sufficiently sized platinum weld between the tungsten probe tip and diamond nanobeam was deposited, the diamond nanobeam was picked off the substrate and transferred to a post of a copper TEM lift-out grid. To attach the diamond nanobeam to the copper TEM lift-out grid post, a similar platinum weld was deposited with the electron beam (Figure B.1 (c)). Care was taken to avoid running the diamond nanobeam into the copper structure, so that excessive bends/twists and further plastic strain would not be introduced into the diamond structure. Once the diamond nanobeam was successfully attached to the copper grid, it was then released from the tungsten probe tip using the Ga^+ ion beam (Figure B.1 (d)). A quick single pass raster scan of the FIB at low current was done to locate the beam and tungsten tip, followed by localized milling at the tip-nanobeam attachment point. Once the attachment point was removed by FIB milling, the nanobeam transfer was complete (Figure B.1 (e)). The total time for this process was ~ 1 to 2 hours per beam. Despite best efforts, redeposition of carbon and platinum was significant near the ends of the beam. However, given the long

nanobeam length, a large region in the center of the structure was virtually clear of any foreign material introduced during sample prep.

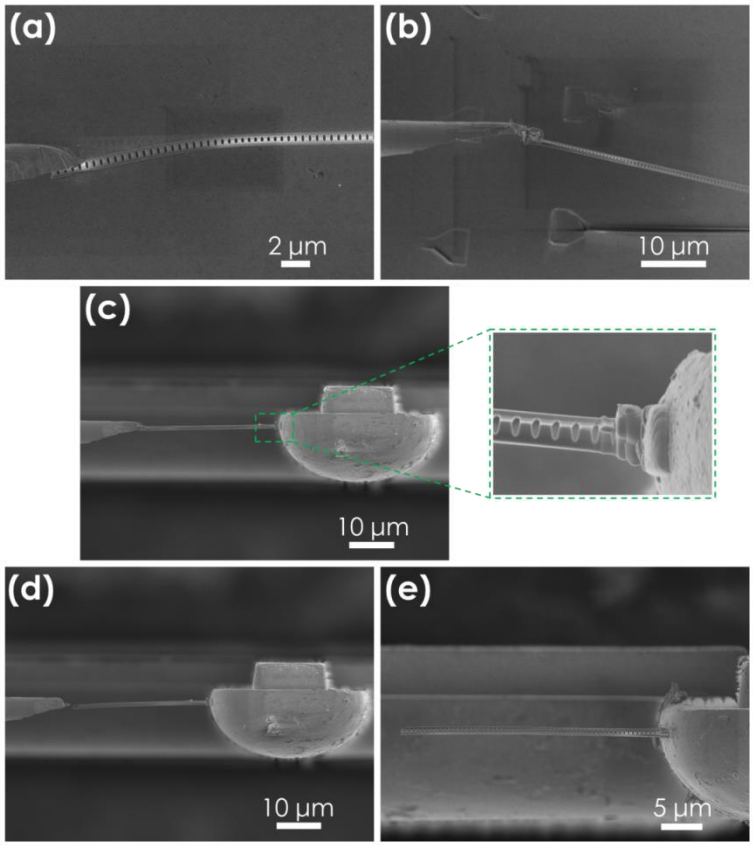

Figure B.1 | Preparation of diamond nanobeams for TEM imaging. (a) The micromanipulator controlled tungsten tip (Omniprobe) installed within the SEM-FIB dual beam system is used to first dislodge a selected diamond nanobeam by bending it up to ~ 15^{o} laterally at one end. This is repeated on the opposite end of the diamond nanobeam to achieve a specimen fully un-adhered from the supporting silver substrate. **(b)** The diamond nanobeam is attached to the tungsten tip via localized electron beam assisted platinum deposition. Following deposition of the platinum weld, the diamond nanobeam is transported to the copper TEM lift-out grid. **(c)** The diamond nanobeam is attached to a post of the copper TEM lift-out grid via a second platinum weld. The call out shows a zoomed in image of localized electron beam assisted platinum deposit. **(d)** The tungsten tip is removed from the diamond nanobeam by localized milling with the focused Ga^{+} ion beam. **(e)** After removing the tungsten tip, the diamond nanobeam is securely fastened to the copper TEM lift-out grid post.

Figure B.2 reveals a series of TEM images (taken at 200 kV in a JEOL 2100 TEM) of the prepared diamond nanobeams previously described. Figure B.2 (a) shows a bright-field TEM image of a single unit cell of the diamond nanobeam cavity, taken near the middle of the structure. A corresponding electron diffraction pattern is shown in Figure B.2 (b) confirming the single-crystal nature of the diamond specimen. Immediately, significant thickness fringes are observed in the bright-field TEM image, attributed to the triangular cross-section. However, a second interesting feature which was not obvious during SEM analysis is now apparent. In the vicinity of the bottom apex of the diamond nanobeam cross-section – refer to the close up bright-field image shown in Figure B.2 (c) – the distinct thickness fringes are no longer visible, indicating there is a large region of extremely thin diamond (or potentially graphite). As well, there appears to be a beveled nature to the side-profile of this region of diamond. High-magnification images at the immediate edge of the bottom apex region indicate the triangular cross-section reaches an extremely fine tip, with an edge roughness < 5 nm. This extremely thin region of diamond at the bottom apex of the diamond nanobeam cross-section suggests that angled-etching of this particular structure was actually incomplete, and an excess of diamond remains on the structure. The true bottom apex of the structure is likely located at the point where the dominant thickness fringes end. It is possible that this extra material due to incomplete angled-etching has a significant impact on the optical mode supported by the entire structure, and may actually contribute to optical losses in the device. Further confirmation that this region of thin diamond at the bottom of the structure resulted from incomplete etching is given by dark-field images show in Figures B.2 (f) and (g). Here, different placement of the TEM objective aperture allows two sets of fringes to be illuminated in the structure. In Figure B.2 (f), a set of illuminated thickness fringes which are very closely spaced and localized to the region of extremely thin diamond are apparent. However, slight adjustment of the objective aperture yields the dark-field image in Figure B.2 (g), which reveals illuminated fringes similar to those apparent in the bright-field image in Figure B.2 (c). Therefore, the region of extremely thin diamond in the immediate vicinity of the bottom apex of the triangular cross-section likely has a different slope than the angled-etched surfaces of the diamond structure. This again confirms our suspicion that there is excess diamond material at the

bottom of the structure resulting from incomplete angled-etching. Removal of this thin material in future device fabrication may also yield improved optical losses in diamond nanobeam cavities.

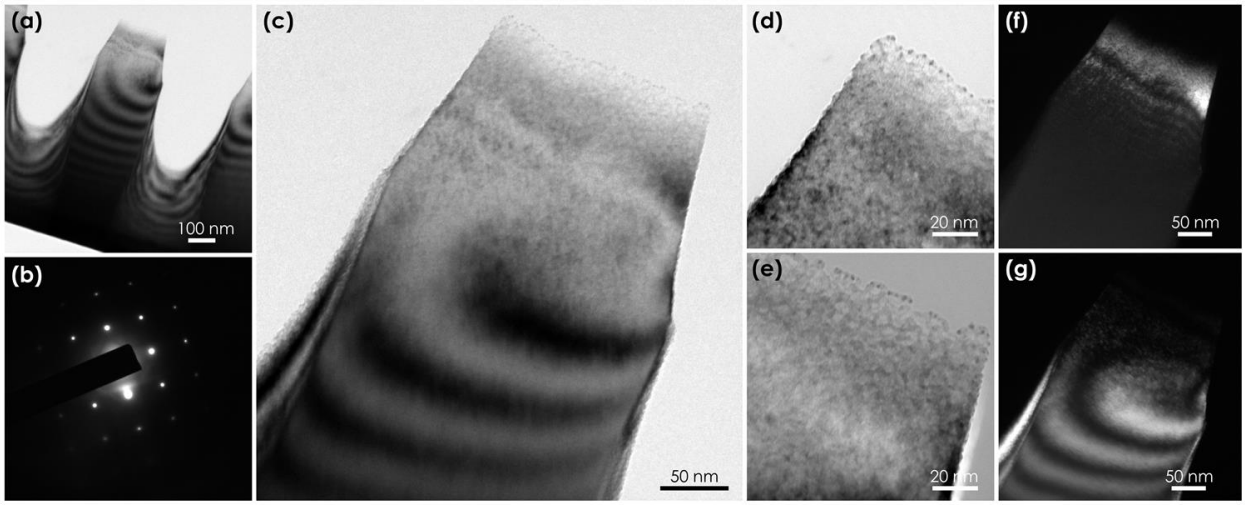

Figure B.2 | Transmission electron microscopy and electron diffraction of diamond nanobeam photonic crystal cavities. (a) Bright-field TEM image of a diamond nanobeam photonic crystal unit cell, with **(b)** corresponding electron diffraction. **(c)** Zoomed in bright-field TEM image of the triangular cross-section bottom apex, with high-resolution images of the thinnest regions shown in **(d)** and **(e)**. Dark-field TEM images of the triangular cross-section bottom apex revealing two different regions of thickness fringes.

References

[1] G. Campbell, *Blood Diamonds, Revised Edition: Tracing the Deadly Path of the World's Most Precious Stones.* Basic Books, 2012.

[2] K. Nassau and J. Nassau, "The history and present status of synthetic diamond," *Journal of Crystal Growth*, vol. 46, no. 2, p. 157-172, 1979.

[3] P. Zimnisky, "What It Will Take For The Synthetic Diamond Industry to be (Un)Successful," *London Mining Journal*, p. 28-29, 2015.

[4] S.E. Coe and R.S. Sussmann, "Optical, thermal and mechanical properties of CVD diamond," *Diamond and Related Materials*, vol. 9, no. 9–10, p. 1726-1729, 2000.

[5] D.E. Scott, "The history and impact of synthetic diamond cutters and diamond enhanced inserts on the oil and gas industry," *Industrial Diamond Review*, vol. 1, p. 48-55, 2006.

[6] R.S. Balmer, J.R. Brandon, S.L. Clewes, H.K. Dhillon, J.M. Dodson, I. Friel, P.N. Inglis, T.D. Madgwick, M.L. Markham, T.P. Mollart, N. Perkins, G.A. Scarsbrook, D.J. Twitchen, A.J. Whitehead, J.J. Wilman, and S.M. Woollard, "Chemical vapour deposition synthetic diamond: materials, technology and applications," *Journal of Physics: Condensed Matter*, vol. 21, no. 36, p. 364221, 2009.

[7] D.J. Twitchen, C.S.J. Pickles, S.E. Coe, R.S. Sussmann, and C.E. Hall, "Thermal conductivity measurements on CVD diamond," *Diamond and Related Materials*, vol. 10, no. 3–7, p. 731-735, 2001.

[8] I. Friel, S.L. Geoghegan, D.J. Twitchen, and G.A. Scarsbrook. *Development of high quality single crystal diamond for novel laser applications*. in *Proc. SPIE 7838, Optics and Photonics for Counterterrorism and Crime Fighting VI and Optical Materials in Defence Systems Technology VII*, 2010.

[9] A.M. Bennett and E. Anoikin. *CVD diamond for high power laser applications*. in *Proc. SPIE 8603, High-Power Laser Materials Processing: Lasers, Beam Delivery, Diagnostics, and Applications II*, 2013.

[10] J.M. Dodson, J.R. Brandon, H.K. Dhillon, I. Friel, S.L. Geoghegan, T.P. Mollart, P. Santini, G.A. Scarsbrook, D.J. Twitchen, A.J. Whitehead, J.J. Wilman, and H. de Wit. *Single crystal and polycrystalline CVD diamond for demanding optical applications*. in *Proc. SPIE 8016, Window and Dome Technologies and Materials XII*, 2011.

[11] F. Ejeckam, D. Francis, F. Faili, J. Dodson, D.J. Twitchen, B. Bolliger, and D. Babic. *Diamond for enhanced GaN device performance*. in *2014 IEEE Intersociety Conference on Thermal and Thermomechanical Phenomena in Electronic Systems (ITherm)*, 2014.

[12] G.H. Jessen, J.K. Gillespie, G.D. Via, A. Crespo, D. Langley, J. Wasserbauer, F. Faili, D. Francis, D. Babic, F. Ejeckam, S. Guo, and I. Eliashevich. *AlGaN/GaN HEMT on Diamond Technology Demonstration*. in *IEEE Compound Semiconductor Integrated Circuit Symposium, 2006.*, 2006.

[13] J.G. Felbinger, M.V.S. Chandra, Y. Sun, L.F. Eastman, J. Wasserbauer, F. Faili, D. Babic, D. Francis, and F. Ejeckam, "Comparison of GaN HEMTs on Diamond and SiC Substrates," *Electron Device Letters, IEEE*, vol. 28, no. 11, p. 948-950, 2007.

[14] G. Balasubramanian, P. Neumann, D. Twitchen, M. Markham, R. Kolesov, N. Mizuochi, J. Isoya, J. Achard, J. Beck, J. Tissler, V. Jacques, P.R. Hemmer, F. Jelezko, and J. Wrachtrup, "Ultralong spin coherence time in isotopically engineered diamond," *Nat Mater*, vol. 8, no. 5, p. 383-387, 2009.

[15] M.L. Markham, J.M. Dodson, G.A. Scarsbrook, D.J. Twitchen, G. Balasubramanian, F. Jelezko, and J. Wrachtrup, "CVD diamond for spintronics," *Diamond and Related Materials*, vol. 20, no. 2, p. 134-139, 2011.

[16] P. Rath, S. Ummethala, C. Nebel, and W.H.P. Pernice, "Diamond as a material for monolithically integrated optical and optomechanical devices," *physica status solidi (a)*, vol. 212, no. 11, p. 2385-2399, 2015.

[17] A.M. Zaitsev, *Optical Properties of Diamond: A Data Handbook*. Springer, 2001.

[18] D.H. Douglas-Hamilton, E.D. Hoag, and J.R.M. Seitz, "Diamond as a high-power-laser window," *Journal of the Optical Society of America*, vol. 64, no. 1, p. 36-38, 1974.

[19] J.S. Levy, A. Gondarenko, M.A. Foster, A.C. Turner-Foster, A.L. Gaeta, and M. Lipson, "CMOS-compatible multiple-wavelength oscillator for on-chip optical interconnects," *Nat Photon*, vol. 4, no. 1, p. 37-40, 2010.

[20] L. Razzari, D. Duchesne, M. Ferrera, R. Morandotti, S. Chu, B.E. Little, and D.J. Moss, "CMOS-compatible integrated optical hyper-parametric oscillator," *Nat Photon*, vol. 4, no. 1, p. 41-45, 2010.

[21] B. Jalali, V. Raghunathan, R. Shori, S. Fathpour, D. Dimitropoulos, and O. Stafsudd, "Prospects for Silicon Mid-IR Raman Lasers," *Selected Topics in Quantum Electronics, IEEE Journal of*, vol. 12, no. 6, p. 1618-1627, 2006.

[22] R. Espinola, J. Dadap, J.R. Osgood, S. McNab, and Y. Vlasov, "Raman amplification in ultrasmall silicon-on-insulator wire waveguides," *Optics Express*, vol. 12, no. 16, p. 3713-3718, 2004.

[23] A.A. Kaminskii, V.G. Ralchenko, and V.I. Konov, "CVD-diamond – a novel χ (3) - nonlinear active crystalline material for SRS generation in very wide spectral range," *Laser Physics Letters*, vol. 3, no. 4, p. 171, 2006.

[24] M.D. Levenson and N. Bloembergen, "Dispersion of the nonlinear optical susceptibility tensor in centrosymmetric media," *Physical Review B*, vol. 10, no. 10, p. 4447-4463, 1974.

[25] B.J.M. Hausmann, I. Bulu, V. Venkataraman, P. Deotare, and M. Loncar, "Diamond nonlinear photonics," *Nat Photon*, vol. 8, no. 5, p. 369-374, 2014.

[26] R.P. Mildren, J.E. Butler, and J.R. Rabeau, "CVD-diamond external cavity Raman laser at 573 nm," *Optics Express*, vol. 16, no. 23, p. 18950-18955, 2008.

[27] S.M. Spillane, T.J. Kippenberg, and K.J. Vahala, "Ultralow-threshold Raman laser using a spherical dielectric microcavity," *Nature*, vol. 415, no. 6872, p. 621-623, 2002.

[28] H. Rong, S. Xu, O. Cohen, O. Raday, M. Lee, V. Sih, and M. Paniccia, "A cascaded silicon Raman laser," *Nat Photon*, vol. 2, no. 3, p. 170-174, 2008.

[29] S. Blair and K. Zheng, "Microresonator-enhanced Raman amplification," *Journal of the Optical Society of America B*, vol. 23, no. 6, p. 1117-1123, 2006.

[30] A.A. Savchenkov, A.B. Matsko, D. Strekalov, M. Mohageg, V.S. Ilchenko, and L. Maleki, "Low Threshold Optical Oscillations in a Whispering Gallery Mode CaF2 Resonator," *Physical Review Letters*, vol. 93, no. 24, p. 243905, 2004.

[31] Y. Wu, X. Yang, and P.T. Leung, "Theory of microcavity-enhanced Raman gain," *Optics Letters*, vol. 24, no. 5, p. 345-347, 1999.

[32] P. Latawiec, V. Venkataraman, M.J. Burek, B.J.M. Hausmann, I. Bulu, and M. Lončar, "On-chip diamond Raman laser," *Optica*, vol. 2, no. 11, p. 924-928, 2015.

[33] J.-P.M. Feve, K.E. Shortoff, M.J. Bohn, and J.K. Brasseur, "High average power diamond Raman laser," *Optics Express*, vol. 19, no. 2, p. 913-922, 2011.

[34] E. Granados, D.J. Spence, and R.P. Mildren, "Deep ultraviolet diamond Raman laser," *Optics Express*, vol. 19, no. 11, p. 10857-10863, 2011.

[35] W. Lubeigt, G.M. Bonner, J.E. Hastie, M.D. Dawson, D. Burns, and A.J. Kemp, "An intra-cavity Raman laser using synthetic single-crystal diamond," *Optics Express*, vol. 18, no. 16, p. 16765-16770, 2010.

[36] W. Lubeigt, G.M. Bonner, J.E. Hastie, M.D. Dawson, D. Burns, and A.J. Kemp, "Continuous-wave diamond Raman laser," *Optics Letters*, vol. 35, no. 17, p. 2994-2996, 2010.

[37] R.P. Mildren and A. Sabella, "Highly efficient diamond Raman laser," *Optics Letters*, vol. 34, no. 18, p. 2811-2813, 2009.

[38] I. Aharonovich and E. Neu, "Diamond Nanophotonics," *Advanced Optical Materials*, vol. 2, no. 10, p. 911-928, 2014.

[39] C. Kurtsiefer, S. Mayer, P. Zarda, and H. Weinfurter, "Stable Solid-State Source of Single Photons," *Physical Review Letters*, vol. 85, no. 2, p. 290-293, 2000.

[40] I. Aharonovich, S. Castelletto, D.A. Simpson, C.H. Su, A.D. Greentree, and S. Prawer, "Diamond-based single-photon emitters," *Reports on Progress in Physics*, vol. 74, no. 7, p. 076501, 2011.

[41] D.M. Toyli, D.J. Christle, A. Alkauskas, B.B. Buckley, C.G. Van de Walle, and D.D. Awschalom, "Measurement and Control of Single Nitrogen-Vacancy Center Spins above 600 K," *Physical Review X*, vol. 2, no. 3, p. 031001, 2012.

[42] F. Jelezko and J. Wrachtrup, "Single defect centres in diamond: A review," *physica status solidi (a)*, vol. 203, no. 13, p. 3207-3225, 2006.

[43] M.W. Doherty, N.B. Manson, P. Delaney, F. Jelezko, J. Wrachtrup, and L.C.L. Hollenberg, "The nitrogen-vacancy colour centre in diamond," *Physics Reports*, vol. 528, no. 1, p. 1-45, 2013.

[44] A. Gruber, A. Dräbenstedt, C. Tietz, L. Fleury, J. Wrachtrup, and C.v. Borczyskowski, "Scanning Confocal Optical Microscopy and Magnetic Resonance on Single Defect Centers," *Science*, vol. 276, no. 5321, p. 2012-2014, 1997.

[45] E. Togan, Y. Chu, A.S. Trifonov, L. Jiang, J. Maze, L. Childress, M.V.G. Dutt, A.S. Sorensen, P.R. Hemmer, A.S. Zibrov, and M.D. Lukin, "Quantum entanglement between an optical photon and a solid-state spin qubit," *Nature*, vol. 466, no. 7307, p. 730-734, 2010.

[46] P.C. Maurer, G. Kucsko, C. Latta, L. Jiang, N.Y. Yao, S.D. Bennett, F. Pastawski, D. Hunger, N. Chisholm, M. Markham, D.J. Twitchen, J.I. Cirac, and M.D. Lukin, "Room-Temperature Quantum Bit Memory Exceeding One Second," *Science*, vol. 336, no. 6086, p. 1283-1286, 2012.

[47] H. Bernien, L. Childress, L. Robledo, M. Markham, D. Twitchen, and R. Hanson, "Two-Photon Quantum Interference from Separate Nitrogen Vacancy Centers in Diamond," *Physical Review Letters*, vol. 108, no. 4, p. 043604, 2012.

[48] A. Sipahigil, M.L. Goldman, E. Togan, Y. Chu, M. Markham, D.J. Twitchen, A.S. Zibrov, A. Kubanek, and M.D. Lukin, "Quantum Interference of Single Photons from Remote Nitrogen-Vacancy Centers in Diamond," *Physical Review Letters*, vol. 108, no. 14, p. 143601, 2012.

[49] H. Bernien, B. Hensen, W. Pfaff, G. Koolstra, M.S. Blok, L. Robledo, T.H. Taminiau, M. Markham, D.J. Twitchen, L. Childress, and R. Hanson, "Heralded entanglement between solid-state qubits separated by three metres," *Nature*, vol. 497, no. 7447, p. 86-90, 2013.

[50] W. Pfaff, B.J. Hensen, H. Bernien, S.B. van Dam, M.S. Blok, T.H. Taminiau, M.J. Tiggelman, R.N. Schouten, M. Markham, D.J. Twitchen, and R. Hanson, "Unconditional quantum teleportation between distant solid-state quantum bits," *Science*, vol. 345, no. 6196, p. 532-535, 2014.

[51] B. Hensen, H. Bernien, A.E. Dreau, A. Reiserer, N. Kalb, M.S. Blok, J. Ruitenberg, R.F.L. Vermeulen, R.N. Schouten, C. Abellan, W. Amaya, V. Pruneri, M.W. Mitchell, M. Markham, D.J. Twitchen, D. Elkouss, S. Wehner, T.H. Taminiau, and R. Hanson,

"Loophole-free Bell inequality violation using electron spins separated by 1.3 kilometres," *Nature*, vol. 526, no. 7575, p. 682-686, 2015.

[52] M. Lončar and A. Faraon, "Quantum photonic networks in diamond," *MRS Bulletin*, vol. 38, no. 02, p. 144-148, 2013.

[53] B.J.M. Hausmann, J.T. Choy, T.M. Babinec, B.J. Shields, I. Bulu, M.D. Lukin, and M. Lončar, "Diamond nanophotonics and applications in quantum science and technology," *physica status solidi (a)*, vol. 209, no. 9, p. 1619-1630, 2012.

[54] I. Aharonovich, A.D. Greentree, and S. Prawer, "Diamond photonics," *Nat Photon*, vol. 5, no. 7, p. 397-405, 2011.

[55] J.P. Goss, R. Jones, S.J. Breuer, P.R. Briddon, and S. Öberg, "The Twelve-Line 1.682 eV Luminescence Center in Diamond and the Vacancy-Silicon Complex," *Physical Review Letters*, vol. 77, no. 14, p. 3041-3044, 1996.

[56] N. Elke, S. David, R.-M. Janine, G. Stefan, F. Martin, S. Matthias, and B. Christoph, "Single photon emission from silicon-vacancy colour centres in chemical vapour deposition nano-diamonds on iridium," *New Journal of Physics*, vol. 13, no. 2, p. 025012, 2011.

[57] L.J. Rogers, K.D. Jahnke, M.W. Doherty, A. Dietrich, L.P. McGuinness, C. Müller, T. Teraji, H. Sumiya, J. Isoya, N.B. Manson, and F. Jelezko, "Electronic structure of the negatively charged silicon-vacancy center in diamond," *Physical Review B*, vol. 89, no. 23, p. 235101, 2014.

[58] C. Hepp, T. Müller, V. Waselowski, J.N. Becker, B. Pingault, H. Sternschulte, D. Steinmüller-Nethl, A. Gali, J.R. Maze, M. Atatüre, and C. Becher, "Electronic Structure of the Silicon Vacancy Color Center in Diamond," *Physical Review Letters*, vol. 112, no. 3, p. 036405, 2014.

[59] L.J. Rogers, K.D. Jahnke, T. Teraji, L. Marseglia, C. Müller, B. Naydenov, H. Schauffert, C. Kranz, J. Isoya, L.P. McGuinness, and F. Jelezko, "Multiple intrinsically identical single-photon emitters in the solid state," *Nat Commun*, vol. 5, 2014.

[60] A. Sipahigil, K.D. Jahnke, L.J. Rogers, T. Teraji, J. Isoya, A.S. Zibrov, F. Jelezko, and M.D. Lukin, "Indistinguishable Photons from Separated Silicon-Vacancy Centers in Diamond," *Physical Review Letters*, vol. 113, no. 11, p. 113602, 2014.

[61] T. Müller, C. Hepp, B. Pingault, E. Neu, S. Gsell, M. Schreck, H. Sternschulte, D. Steinmüller-Nethl, C. Becher, and M. Atatüre, "Optical signatures of silicon-vacancy spins in diamond," *Nat Commun*, vol. 5, 2014.

[62] A. Faraon, C. Santori, Z. Huang, V.M. Acosta, and R.G. Beausoleil, "Coupling of Nitrogen-Vacancy Centers to Photonic Crystal Cavities in Monocrystalline Diamond," *Physical Review Letters*, vol. 109, no. 3, p. 033604, 2012.

[63] L.J. Rogers, K.D. Jahnke, M.H. Metsch, A. Sipahigil, J.M. Binder, T. Teraji, H. Sumiya, J. Isoya, M.D. Lukin, P. Hemmer, and F. Jelezko, "All-Optical Initialization, Readout, and Coherent Preparation of Single Silicon-Vacancy Spins in Diamond," *Physical Review Letters*, vol. 113, no. 26, p. 263602, 2014.

[64] D.J. Kay, S. Alp, M.B. Jan, W.D. Marcus, M. Mathias, J.R. Lachlan, B.M. Neil, D.L. Mikhail, and J. Fedor, "Electron–phonon processes of the silicon-vacancy centre in diamond," *New Journal of Physics*, vol. 17, no. 4, p. 043011, 2015.

[65] L. Marseglia, J.P. Hadden, A.C. Stanley-Clarke, J.P. Harrison, B. Patton, Y.-L.D. Ho, B. Naydenov, F. Jelezko, J. Meijer, P.R. Dolan, J.M. Smith, J.G. Rarity, and J.L. O'Brien, "Nanofabricated solid immersion lenses registered to single emitters in diamond," *Applied Physics Letters*, vol. 98, no. 13, p. 133107, 2011.

[66] J.P. Hadden, J.P. Harrison, A.C. Stanley-Clarke, L. Marseglia, Y.-L.D. Ho, B.R. Patton, J.L. O'Brien, and J.G. Rarity, "Strongly enhanced photon collection from diamond defect centers under microfabricated integrated solid immersion lenses," *Applied Physics Letters*, vol. 97, no. 24, p. 241901, 2010.

[67] T.M. Babinec, J.M. HausmannBirgit, M. Khan, Y. Zhang, J.R. Maze, P.R. Hemmer, and M. Loncar, "A diamond nanowire single-photon source," *Nat Nano*, vol. 5, no. 3, p. 195-199, 2010.

[68] L. Robledo, L. Childress, H. Bernien, B. Hensen, P.F.A. Alkemade, and R. Hanson, "High-fidelity projective read-out of a solid-state spin quantum register," *Nature*, vol. 477, no. 7366, p. 574-578, 2011.

[69] A. Faraon, P.E. Barclay, C. Santori, K.-M.C. Fu, and R.G. Beausoleil, "Resonant enhancement of the zero-phonon emission from a colour centre in a diamond cavity," *Nat Photon*, vol. 5, no. 5, p. 301-305, 2011.

[70] B.J.M. Hausmann, B.J. Shields, Q. Quan, Y. Chu, N.P. de Leon, R. Evans, M.J. Burek, A.S. Zibrov, M. Markham, D.J. Twitchen, H. Park, M.D. Lukin, and M. Loncăr,

"Coupling of NV Centers to Photonic Crystal Nanobeams in Diamond," *Nano Letters*, vol. 13, no. 12, p. 5791-5796, 2013.

[71] J.C. Lee, D.O. Bracher, S. Cui, K. Ohno, C.A. McLellan, X. Zhang, P. Andrich, B. Alemán, K.J. Russell, A.P. Magyar, I. Aharonovich, A. Bleszynski Jayich, D. Awschalom, and E.L. Hu, "Deterministic coupling of delta-doped nitrogen vacancy centers to a nanobeam photonic crystal cavity," *Applied Physics Letters*, vol. 105, no. 26, p. 261101, 2014.

[72] L. Li, T. Schröder, E.H. Chen, M. Walsh, I. Bayn, J. Goldstein, O. Gaathon, M.E. Trusheim, M. Lu, J. Mower, M. Cotlet, M.L. Markham, D.J. Twitchen, and D. Englund, "Coherent spin control of a nanocavity-enhanced qubit in diamond," *Nat Commun*, vol. 6, 2015.

[73] D.E. Chang, V. Vuletic, and M.D. Lukin, "Quantum nonlinear optics - photon by photon," *Nat Photon*, vol. 8, no. 9, p. 685-694, 2014.

[74] K.L. Ekinci and M.L. Roukes, "Nanoelectromechanical systems," *Review of Scientific Instruments*, vol. 76, no. 6, p. 061101, 2005.

[75] C.T.C. Nguyen, "MEMS technology for timing and frequency control," *Ultrasonics, Ferroelectrics, and Frequency Control, IEEE Transactions on*, vol. 54, no. 2, p. 251-270, 2007.

[76] M. Bagheri, M. Poot, M. Li, W.P.H. Pernice, and H.X. Tang, "Dynamic manipulation of nanomechanical resonators in the high-amplitude regime and non-volatile mechanical memory operation," *Nat Nano*, vol. 6, no. 11, p. 726-732, 2011.

[77] R.L. Badzey and P. Mohanty, "Coherent signal amplification in bistable nanomechanical oscillators by stochastic resonance," *Nature*, vol. 437, no. 7061, p. 995-998, 2005.

[78] K.L. Ekinci, X.M.H. Huang, and M.L. Roukes, "Ultrasensitive nanoelectromechanical mass detection," *Applied Physics Letters*, vol. 84, no. 22, p. 4469-4471, 2004.

[79] H.B. Peng, C.W. Chang, S. Aloni, T.D. Yuzvinsky, and A. Zettl, "Ultrahigh Frequency Nanotube Resonators," *Physical Review Letters*, vol. 97, no. 8, p. 087203, 2006.

[80] Y. Tao, J.M. Boss, B.A. Moores, and C.L. Degen, "Single-crystal diamond nanomechanical resonators with quality factors exceeding one million," *Nat Commun*, vol. 5, 2014.

[81] U. Gysin, S. Rast, P. Ruff, E. Meyer, D.W. Lee, P. Vettiger, and C. Gerber, "Temperature dependence of the force sensitivity of silicon cantilevers," *Physical Review B*, vol. 69, no. 4, p. 045403, 2004.

[82] K.Y. Yasumura, T.D. Stowe, E.M. Chow, T. Pfafman, T.W. Kenny, B.C. Stipe, and D. Rugar, "Quality factors in micron- and submicron-thick cantilevers," *Microelectromechanical Systems, Journal of*, vol. 9, no. 1, p. 117-125, 2000.

[83] E. Kohn, P. Gluche, and M. Adamschik, "Diamond MEMS — a new emerging technology," *Diamond and Related Materials*, vol. 8, no. 2–5, p. 934-940, 1999.

[84] P. Ovartchaiyapong, K.W. Lee, B.A. Myers, and A.C.B. Jayich, "Dynamic strain-mediated coupling of a single diamond spin to a mechanical resonator," *Nat Commun*, vol. 5, 2014.

[85] E.R. MacQuarrie, T.A. Gosavi, A.M. Moehle, N.R. Jungwirth, S.A. Bhave, and G.D. Fuchs, "Coherent control of a nitrogen-vacancy center spin ensemble with a diamond mechanical resonator," *Optica*, vol. 2, no. 3, p. 233-238, 2015.

[86] E.R. MacQuarrie, T.A. Gosavi, N.R. Jungwirth, S.A. Bhave, and G.D. Fuchs, "Mechanical Spin Control of Nitrogen-Vacancy Centers in Diamond," *Physical Review Letters*, vol. 111, no. 22, p. 227602, 2013.

[87] J. Teissier, A. Barfuss, P. Appel, E. Neu, and P. Maletinsky, "Strain Coupling of a Nitrogen-Vacancy Center Spin to a Diamond Mechanical Oscillator," *Physical Review Letters*, vol. 113, no. 2, p. 020503, 2014.

[88] S. Meesala, Y.-I.A. Sohn, Haig A., S. Kim, M.J. Burek, J.T. Choy, and M. Lončar, "Enhanced strain coupling of nitrogen vacancy spins to nanoscale diamond cantilevers," *arXiv:1511.01548*, 2015.

[89] S.D. Bennett, N.Y. Yao, J. Otterbach, P. Zoller, P. Rabl, and M.D. Lukin, "Phonon-Induced Spin-Spin Interactions in Diamond Nanostructures: Application to Spin Squeezing," *Physical Review Letters*, vol. 110, no. 15, p. 156402, 2013.

[90] J.D. Joannopoulos, S.G. Johnson, J.N. Winn, and R.D. Meade, *Photonic Crystals: Molding the Flow of Light, 2nd ed*. Princeton University Press, 2008.

[91] M. Lončar, D. Nedeljković, T. Doll, J. Vučković, A. Scherer, and T.P. Pearsall, "Waveguiding in planar photonic crystals," *Applied Physics Letters*, vol. 77, no. 13, p. 1937-1939, 2000.

[92] D.W. Carr, S. Evoy, L. Sekaric, H.G. Craighead, and J.M. Parpia, "Measurement of mechanical resonance and losses in nanometer scale silicon wires," *Applied Physics Letters*, vol. 75, no. 7, p. 920-922, 1999.

[93] Y.T. Yang, K.L. Ekinci, X.M.H. Huang, L.M. Schiavone, M.L. Roukes, C.A. Zorman, and M. Mehregany, "Monocrystalline silicon carbide nanoelectromechanical systems," *Applied Physics Letters*, vol. 78, no. 2, p. 162-164, 2001.

[94] L. Sekaric, D.W. Carr, S. Evoy, J.M. Parpia, and H.G. Craighead, "Nanomechanical resonant structures in silicon nitride: fabrication, operation and dissipation issues," *Sensors and Actuators A: Physical*, vol. 101, no. 1–2, p. 215-219, 2002.

[95] W. Bogaerts, D. Taillaert, B. Luyssaert, P. Dumon, J. Van Campenhout, P. Bienstman, D. Van Thourhout, R. Baets, V. Wiaux, and S. Beckx, "Basic structures for photonic integrated circuits in Silicon-on-insulator," *Optics Express*, vol. 12, no. 8, p. 1583-1591, 2004.

[96] W. Bogaerts, P. Dumon, D. Van Thourhout, D. Taillaert, P. Jaenen, J. Wouters, S. Beckx, V. Wiaux, and R.G. Baets, "Compact Wavelength-Selective Functions in Silicon-on-Insulator Photonic Wires," *Selected Topics in Quantum Electronics, IEEE Journal of*, vol. 12, no. 6, p. 1394-1401, 2006.

[97] W. Bogaerts, R. Baets, P. Dumon, V. Wiaux, S. Beckx, D. Taillaert, B. Luyssaert, J. Van Campenhout, P. Bienstman, and D. Van Thourhout, "Nanophotonic waveguides in silicon-on-insulator fabricated with CMOS technology," *Lightwave Technology, Journal of*, vol. 23, no. 1, p. 401-412, 2005.

[98] W. Bogaerts, P. De Heyn, T. Van Vaerenbergh, K. De Vos, S. Kumar Selvaraja, T. Claes, P. Dumon, P. Bienstman, D. Van Thourhout, and R. Baets, "Silicon microring resonators," *Laser & Photonics Reviews*, vol. 6, no. 1, p. 47-73, 2012.

[99] P.B. Deotare, M.W. McCutcheon, I.W. Frank, M. Khan, and M. Lončar, "High quality factor photonic crystal nanobeam cavities," *Applied Physics Letters*, vol. 94, no. 12, p. 121106, 2009.

[100] Q. Fang, J. Song, X. Luo, M. Yu, G. Lo, and Y. Liu, "Mode-size converter with high coupling efficiency and broad bandwidth," *Optics Express*, vol. 19, no. 22, p. 21588-21594, 2011.

[101] D. Taillaert, P. Bienstman, and R. Baets, "Compact efficient broadband grating coupler for silicon-on-insulator waveguides," *Optics Letters*, vol. 29, no. 23, p. 2749-2751, 2004.

[102] J. Cardenas, K. Luke, L. Lian Wee, C.B. Poitras, P.A. Morton, and M. Lipson. *High coupling efficiency etched facet tapers in silicon*. in *2012 Conference on Lasers and Electro-Optics (CLEO)*, 2012.

[103] T.G. Tiecke, K.P. Nayak, J.D. Thompson, T. Peyronel, N.P. de Leon, V. Vuletić, and M.D. Lukin, "Efficient fiber-optical interface for nanophotonic devices," *Optica*, vol. 2, no. 2, p. 70-75, 2015.

[104] O. Auciello and A.V. Sumant, "Status review of the science and technology of ultrananocrystalline diamond (UNCD™) films and application to multifunctional devices," *Diamond and Related Materials*, vol. 19, no. 7–9, p. 699-718, 2010.

[105] P. Rath, N. Gruhler, S. Khasminskaya, C. Nebel, C. Wild, and W.H.P. Pernice, "Waferscale nanophotonic circuits made from diamond-on-insulator substrates," *Optics Express*, vol. 21, no. 9, p. 11031-11036, 2013.

[106] E. Kohn, M. Adamschik, P. Schmid, S. Ertl, and A. Flöter, "Diamond electro-mechanical micro devices — technology and performance," *Diamond and Related Materials*, vol. 10, no. 9–10, p. 1684-1691, 2001.

[107] A. Orlando, B. James, A.C. John, E.G. Jennifer, X. Xingcheng, P. Bei, and D.E. Horacio, "Materials science and fabrication processes for a new MEMS technology based on ultrananocrystalline diamond thin films," *Journal of Physics: Condensed Matter*, vol. 16, no. 16, p. R539, 2004.

[108] J. Riedrich-Moller, L. Kipfstuhl, C. Hepp, E. Neu, C. Pauly, F. Mucklich, A. Baur, M. Wandt, S. Wolff, M. Fischer, S. Gsell, M. Schreck, and C. Becher, "One- and two-dimensional photonic crystal microcavities in single crystal diamond," *Nat Nano*, vol. 7, no. 1, p. 69-74, 2012.

[109] M. Liao, S. Hishita, E. Watanabe, S. Koizumi, and Y. Koide, "Suspended Single-Crystal Diamond Nanowires for High-Performance Nanoelectromechanical Switches," *Advanced Materials*, vol. 22, no. 47, p. 5393-5397, 2010.

[110] M.K. Zalalutdinov, M.P. Ray, D.M. Photiadis, J.T. Robinson, J.W. Baldwin, J.E. Butler, T.I. Feygelson, B.B. Pate, and B.H. Houston, "Ultrathin Single Crystal Diamond Nanomechanical Dome Resonators," *Nano Letters*, vol. 11, no. 10, p. 4304-4308, 2011.

[111] C.F. Wang, E.L. Hu, J. Yang, and J.E. Butler, "Fabrication of suspended single crystal diamond devices by electrochemical etch," *Journal of Vacuum Science & Technology B*, vol. 25, no. 3, p. 730-733, 2007.

[112] B.A. Fairchild, P. Olivero, S. Rubanov, A.D. Greentree, F. Waldermann, R.A. Taylor, I. Walmsley, J.M. Smith, S. Huntington, B.C. Gibson, D.N. Jamieson, and S. Prawer, "Fabrication of Ultrathin Single-Crystal Diamond Membranes," *Advanced Materials*, vol. 20, no. 24, p. 4793-4798, 2008.

[113] P. Olivero, S. Rubanov, P. Reichart, B.C. Gibson, S.T. Huntington, J. Rabeau, A.D. Greentree, J. Salzman, D. Moore, D.N. Jamieson, and S. Prawer, "Ion-Beam-Assisted Lift-Off Technique for Three-Dimensional Micromachining of Freestanding Single-Crystal Diamond," *Advanced Materials*, vol. 17, no. 20, p. 2427-2430, 2005.

[114] L. Meiyong, L. Chun, H. Shunichi, and K. Yasuo, "Batch production of single-crystal diamond bridges and cantilevers for microelectromechanical systems," *Journal of Micromechanics and Microengineering*, vol. 20, no. 8, p. 085002, 2010.

[115] M.P. Hiscocks, K. Ganesan, B.C. Gibson, S.T. Huntington, F. Ladouceur, and S. Prawer, "Diamond waveguides fabricated by reactive ion etching," *Optics Express*, vol. 16, no. 24, p. 19512-19519, 2008.

[116] A.P. Magyar, J.C. Lee, A.M. Limarga, I. Aharonovich, F. Rol, D.R. Clarke, M. Huang, and E.L. Hu, "Fabrication of thin, luminescent, single-crystal diamond membranes," *Applied Physics Letters*, vol. 99, no. 8, p. 081913, 2011.

[117] N.R. Parikh, J.D. Hunn, E. McGucken, M.L. Swanson, C.W. White, R.A. Rudder, D.P. Malta, J.B. Posthill, and R.J. Markunas, "Single-crystal diamond plate liftoff achieved by ion implantation and subsequent annealing," *Applied Physics Letters*, vol. 61, no. 26, p. 3124-3126, 1992.

[118] I. Aharonovich, J.C. Lee, A.P. Magyar, B.B. Buckley, C.G. Yale, D.D. Awschalom, and E.L. Hu, "Homoepitaxial Growth of Single Crystal Diamond Membranes for Quantum Information Processing," *Advanced Materials*, vol. 24, no. 10, p. OP54-OP59, 2012.

[119] P. Ovartchaiyapong, L.M.A. Pascal, B.A. Myers, P. Lauria, and A.C. Bleszynski Jayich, "High quality factor single-crystal diamond mechanical resonators," *Applied Physics Letters*, vol. 101, no. 16, p. 163505, 2012.

[120] Y. Tao and C. Degen, "Facile Fabrication of Single-Crystal-Diamond Nanostructures with Ultrahigh Aspect Ratio," *Advanced Materials*, vol. 25, no. 29, p. 3962-3967, 2013.

[121] B.J.M. Hausmann, I.B. Bulu, P.B. Deotare, M. McCutcheon, V. Venkataraman, M.L. Markham, D.J. Twitchen, and M. Lončar, "Integrated High-Quality Factor Optical Resonators in Diamond," *Nano Letters*, vol. 13, no. 5, p. 1898-1902, 2013.

[122] B.J.M. Hausmann, B. Shields, Q. Quan, P. Maletinsky, M. McCutcheon, J.T. Choy, T.M. Babinec, A. Kubanek, A. Yacoby, M.D. Lukin, and M. Lončar, "Integrated Diamond Networks for Quantum Nanophotonics," *Nano Letters*, vol. 12, no. 3, p. 1578-1582, 2012.

[123] F. Andrei, S. Charles, H. Zhihong, C.F. Kai-Mei, M.A. Victor, F. David, and G.B. Raymond, "Quantum photonic devices in single-crystal diamond," *New Journal of Physics*, vol. 15, no. 2, p. 025010, 2013.

[124] Y. Chu, N.P. de Leon, B.J. Shields, B. Hausmann, R. Evans, E. Togan, M.J. Burek, M. Markham, A. Stacey, A.S. Zibrov, A. Yacoby, D.J. Twitchen, M. Loncar, H. Park, P. Maletinsky, and M.D. Lukin, "Coherent Optical Transitions in Implanted Nitrogen Vacancy Centers," *Nano Letters*, vol. 14, no. 4, p. 1982-1986, 2014.

[125] T. Yamamoto, T. Umeda, K. Watanabe, S. Onoda, M.L. Markham, D.J. Twitchen, B. Naydenov, L.P. McGuinness, T. Teraji, S. Koizumi, F. Dolde, H. Fedder, J. Honert, J. Wrachtrup, T. Ohshima, F. Jelezko, and J. Isoya, "Extending spin coherence times of diamond qubits by high-temperature annealing," *Physical Review B*, vol. 88, no. 7, p. 075206, 2013.

[126] R.E. Evans, A. Sipahigil, D.D. Sukachev, A.S. Zibrov, and M.D. Lukin, "Coherent optical emitters in diamond nanostructures via ion implantation," *arXiv:1512.03820*, 2015.

[127] T.M. Babinec, J.T. Choy, K.J.M. Smith, M. Khan, and M. Lončar, "Design and focused ion beam fabrication of single crystal diamond nanobeam cavities," *Journal of Vacuum Science & Technology B*, vol. 29, no. 1, p. 010601, 2011.

[128] B. Igal, M. Boris, S. Joseph, and K. Rafi, "Triangular nanobeam photonic cavities in single-crystal diamond," *New Journal of Physics*, vol. 13, no. 2, p. 025018, 2011.

[129] I. Bayn, B. Meyler, A. Lahav, J. Salzman, R. Kalish, B.A. Fairchild, S. Prawer, M. Barth, O. Benson, T. Wolf, P. Siyushev, F. Jelezko, and J. Wrachtrup, "Processing of photonic crystal nanocavity for quantum information in diamond," *Diamond and Related Materials*, vol. 20, no. 7, p. 937-943, 2011.

[130] M.J. Burek, N.P. de Leon, B.J. Shields, B.J.M. Hausmann, Y. Chu, Q. Quan, A.S. Zibrov, H. Park, M.D. Lukin, and M. Lončar, "Free-Standing Mechanical and Photonic Nanostructures in Single-Crystal Diamond," *Nano Letters*, vol. 12, no. 12, p. 6084-6089, 2012.

[131] M. Loncar, M.D. Lukin, M.J. Burek, N. de Leon, and B. Shields, *Small-scale fabrication systems and methods,* US Patent 8,999,105, 2015.

[132] M.J. Burek, D. Ramos, P. Patel, I.W. Frank, and M. Lončar, "Nanomechanical resonant structures in single-crystal diamond," *Applied Physics Letters*, vol. 103, no. 13, p. 131904, 2013.

[133] M.J. Burek, Y. Chu, M.S.Z. Liddy, P. Patel, J. Rochman, S. Meesala, W. Hong, Q. Quan, M.D. Lukin, and M. Lončar, "High quality-factor optical nanocavities in bulk single-crystal diamond," *Nat Commun*, vol. 5, 2014.

[134] M.J. Burek, J.D. Cohen, S.M. Meenehan, T. Ruelle, S. Meesala, J. Rochman, H.A. Atikian, M. Markham, D.J. Twitchen, M.D. Lukin, O. Painter, and M. Lončar, "Diamond optomechanical crystals," *arXiv:1512.04166*, 2015.

[135] H.A. Atikian, A. Eftekharian, A. Jafari Salim, M.J. Burek, J.T. Choy, A. Hamed Majedi, and M. Lončar, "Superconducting nanowire single photon detector on diamond," *Applied Physics Letters*, vol. 104, no. 12, p. 122602, 2014.

[136] S.E. Grillo and J.E. Field, "The polishing of diamond," *Journal of Physics D: Applied Physics*, vol. 30, no. 2, p. 202, 1997.

[137] B.J.M. Hausmann, M. Khan, Y. Zhang, T.M. Babinec, K. Martinick, M. McCutcheon, P.R. Hemmer, and M. Lončar, "Fabrication of diamond nanowires for quantum information processing applications," *Diamond and Related Materials*, vol. 19, no. 5–6, p. 621-629, 2010.

[138] G.D. Boyd, L.A. Coldren, and F.G. Storz, "Directional reactive ion etching at oblique angles," *Applied Physics Letters*, vol. 36, no. 7, p. 583-585, 1980.

[139] J.-K. Lee, S.-H. Lee, J.-H. Min, I.-Y. Jang, C.-K. Kim, and S.H. Moon, "Oblique-Directional Plasma Etching of Si Using a Faraday Cage," *Journal of The Electrochemical Society*, vol. 156, no. 7, p. D222-D225, 2009.

[140] S. Takahashi, K. Suzuki, M. Okano, M. Imada, T. Nakamori, Y. Ota, K. Ishizaki, and S. Noda, "Direct creation of three-dimensional photonic crystals by a top-down approach," *Nat Mater*, vol. 8, no. 9, p. 721-725, 2009.

[141] D.W. Carr, L. Sekaric, and H.G. Craighead, "Measurement of nanomechanical resonant structures in single-crystal silicon," *Journal of Vacuum Science & Technology B*, vol. 16, no. 6, p. 3821-3824, 1998.

[142] T. Kouh, D. Karabacak, D.H. Kim, and K.L. Ekinci, "Diffraction effects in optical interferometric displacement detection in nanoelectromechanical systems," *Applied Physics Letters*, vol. 86, no. 1, p. 013106, 2005.

[143] D. Karabacak, T. Kouh, C.C. Huang, and K.L. Ekinci, "Optical knife-edge technique for nanomechanical displacement detection," *Applied Physics Letters*, vol. 88, no. 19, p. 193122, 2006.

[144] W. Weaver, S.P. Timoshenko, and D.H. Young, *Vibration Problems in Engineering, 5th ed.* Wiley, 1990.

[145] W.K. Hiebert, D. Vick, V. Sauer, and M.R. Freeman, "Optical interferometric displacement calibration and thermomechanical noise detection in bulk focused ion beam-fabricated nanoelectromechanical systems," *Journal of Micromechanics and Microengineering*, vol. 20, no. 11, p. 115038, 2010.

[146] J.S. Chan, X.M.H. Huang, M. Manolidis, C.A. Zorman, M. Mehregany, and J. Hone, "Electrothermal tuning of Al–SiC nanomechanical resonators," *Nanotechnology*, vol. 17, no. 5, p. 1506, 2006.

[147] T. Ikehara, R.A.F. Zwijze, and K. Ikeda, "New method for an accurate determination of residual strain in polycrystalline silicon films by analysing resonant frequencies of micromachined beams," *Journal of Micromechanics and Microengineering*, vol. 11, no. 1, p. 55, 2001.

[148] X. Li, T. Ono, Y. Wang, and M. Esashi, "Ultrathin single-crystalline-silicon cantilever resonators: Fabrication technology and significant specimen size effect on Young's modulus," *Applied Physics Letters*, vol. 83, no. 15, p. 3081-3083, 2003.

[149] R.I. Pratt, G.C. Johnson, R.T. Howe, and J.C. Chang. *Micromechanical structures for thin film characterization*. in *Solid-State Sensors and Actuators, 1991. Digest of Technical Papers, TRANSDUCERS '91., 1991 International Conference on*, 1991.

[150] M. Imboden, P. Mohanty, A. Gaidarzhy, J. Rankin, and B.W. Sheldon, "Scaling of dissipation in megahertz-range micromechanical diamond oscillators," *Applied Physics Letters*, vol. 90, no. 17, p. 173502, 2007.

[151] A.B. Hutchinson, P.A. Truitt, K.C. Schwab, L. Sekaric, J.M. Parpia, H.G. Craighead, and J.E. Butler, "Dissipation in nanocrystalline-diamond nanomechanical resonators," *Applied Physics Letters*, vol. 84, no. 6, p. 972-974, 2004.

[152] V.P. Adiga, A.V. Sumant, S. Suresh, C. Gudeman, O. Auciello, J.A. Carlisle, and R.W. Carpick, "Mechanical stiffness and dissipation in ultrananocrystalline diamond microresonators," *Physical Review B*, vol. 79, no. 24, p. 245403, 2009.

[153] Q. Quan, P.B. Deotare, and M. Loncar, "Photonic crystal nanobeam cavity strongly coupled to the feeding waveguide," *Applied Physics Letters*, vol. 96, no. 20, p. 203102, 2010.

[154] Q. Quan and M. Loncar, "Deterministic design of wavelength scale, ultra-high Q photonic crystal nanobeam cavities," *Optics Express*, vol. 19, no. 19, p. 18529-18542, 2011.

[155] M.W. McCutcheon, P.B. Deotare, Y. Zhang, and M. Lončar, "High-Q transverse-electric/transverse-magnetic photonic crystal nanobeam cavities," *Applied Physics Letters*, vol. 98, no. 11, p. 111117, 2011.

[156] J.T. Hill, A.H. Safavi-Naeini, J. Chan, and O. Painter, "Coherent optical wavelength conversion via cavity optomechanics," *Nat Commun*, vol. 3, p. 1196, 2012.

[157] Y. Zhang, M.W. McCutcheon, I.B. Burgess, and M. Loncar, "Ultra-high-Q TE/TM dual-polarized photonic crystal nanocavities," *Optics Letters*, vol. 34, no. 17, p. 2694-2696, 2009.

[158] M. Cai, O. Painter, and K.J. Vahala, "Observation of Critical Coupling in a Fiber Taper to a Silica-Microsphere Whispering-Gallery Mode System," *Physical Review Letters*, vol. 85, no. 1, p. 74-77, 2000.

[159] R. Rivière, O. Arcizet, A. Schliesser, and T.J. Kippenberg, "Evanescent straight tapered-fiber coupling of ultra-high Q optomechanical micro-resonators in a low-vibration helium-4 exchange-gas cryostat," *Review of Scientific Instruments*, vol. 84, no. 4, p. 043108, 2013.

[160] C.P. Michael, M. Borselli, T.J. Johnson, C. Chrystal, and O. Painter, "An optical fiber-taper probe for wafer-scale microphotonic device characterization," *Optics Express*, vol. 15, no. 8, p. 4745-4752, 2007.

[161] G.S. Wiederhecker, L. Chen, A. Gondarenko, and M. Lipson, "Controlling photonic structures using optical forces," *Nature*, vol. 462, no. 7273, p. 633-636, 2009.

[162] G. Anetsberger , R. Riviere, A. Schliesser, O. Arcizet, and T.J. Kippenberg, "Ultralow-dissipation optomechanical resonators on a chip," *Nat Photon*, vol. 2, no. 10, p. 627-633, 2008.

[163] M.J. Burek and M. Loncar, *Device support structures from bulk substrates,* US Patent App. 13/954,108, 2015.

[164] P. Rabiei, W.H. Steier, C. Zhang, and L.R. Dalton, "Polymer micro-ring filters and modulators," *Lightwave Technology, Journal of*, vol. 20, no. 11, p. 1968-1975, 2002.

[165] H. Lee, T. Chen, J. Li, K.Y. Yang, S. Jeon, O. Painter, and K.J. Vahala, "Chemically etched ultrahigh-Q wedge-resonator on a silicon chip," *Nat Photon*, vol. 6, no. 6, p. 369-373, 2012.

[166] J. Li, H. Lee, T. Chen, and K.J. Vahala, "Characterization of a high coherence, Brillouin microcavity laser on silicon," *Optics Express*, vol. 20, no. 18, p. 20170-20180, 2012.

[167] J. Riedrich-Möller, C. Arend, C. Pauly, F. Mücklich, M. Fischer, S. Gsell, M. Schreck, and C. Becher, "Deterministic Coupling of a Single Silicon-Vacancy Color Center to a Photonic Crystal Cavity in Diamond," *Nano Letters*, vol. 14, no. 9, p. 5281-5287, 2014.

[168] D.R. Turner, *Etch procedure for optical fibers,* US Patent 4,469,554, 1984.

[169] D. Vermeulen, S. Selvaraja, P. Verheyen, G. Lepage, W. Bogaerts, P. Absil, D. Van Thourhout, and G. Roelkens, "High-efficiency fiber-to-chip grating couplers realized using an advanced CMOS-compatible Silicon-On-Insulator platform," *Optics Express*, vol. 18, no. 17, p. 18278-18283, 2010.

[170] T. Tsuchizawa, K. Yamada, H. Fukuda, T. Watanabe, T. Jun-ichi, J.-i. Takahashi, T. Shoji, E. Tamechika, S. Itabashi, and H. Morita, "Microphotonics devices based on silicon microfabrication technology," *Selected Topics in Quantum Electronics, IEEE Journal of*, vol. 11, no. 1, p. 232-240, 2005.

[171] M. Eichenfield, J. Chan, R.M. Camacho, K.J. Vahala, and O. Painter, "Optomechanical crystals," *Nature*, vol. 462, no. 7269, p. 78-82, 2009.

[172] M. Davanço, S. Ates, Y. Liu, and K. Srinivasan, "Si 3 N 4 optomechanical crystals in the resolved-sideband regime," *Applied Physics Letters*, vol. 104, no. 4, p. 041101, 2014.

[173] K.E. Grutter, M. Davanco, and K. Srinivasan, "Si3N4 Nanobeam Optomechanical Crystals," *Selected Topics in Quantum Electronics, IEEE Journal of*, vol. 21, no. 4, p. 1-11, 2015.

[174] K.C. Balram, M. Davanço, J.Y. Lim, J.D. Song, and K. Srinivasan, "Moving boundary and photoelastic coupling in GaAs optomechanical resonators," *Optica*, vol. 1, no. 6, p. 414-420, 2014.

[175] J. Chan, T.P.M. Alegre, A.H. Safavi-Naeini, J.T. Hill, A. Krause, S. Groblacher, M. Aspelmeyer, and O. Painter, "Laser cooling of a nanomechanical oscillator into its quantum ground state," *Nature*, vol. 478, no. 7367, p. 89-92, 2011.

[176] A.H. Safavi-Naeini, T.P.M. Alegre, J. Chan, M. Eichenfield, M. Winger, Q. Lin, J.T. Hill, D.E. Chang, and O. Painter, "Electromagnetically induced transparency and slow light with optomechanics," *Nature*, vol. 472, no. 7341, p. 69-73, 2011.

[177] A.H. Safavi-Naeini, S. Groblacher, J.T. Hill, J. Chan, M. Aspelmeyer, and O. Painter, "Squeezed light from a silicon micromechanical resonator," *Nature*, vol. 500, no. 7461, p. 185-189, 2013.

[178] I.S. Grudinin, H. Lee, O. Painter, and K.J. Vahala, "Phonon Laser Action in a Tunable Two-Level System," *Physical Review Letters*, vol. 104, no. 8, p. 083901, 2010.

[179] J. Chan, A.H. Safavi-Naeini, J.T. Hill, S. Meenehan, and O. Painter, "Optimized optomechanical crystal cavity with acoustic radiation shield," *Applied Physics Letters*, vol. 101, no. 8, p. 081115, 2012.

[180] M. Eichenfield, J. Chan, A.H. Safavi-Naeini, K.J. Vahala, and O. Painter, "Modeling dispersive coupling and losses of localized optical andmechanical modes in optomechanicalcrystals," *Optics Express*, vol. 17, no. 22, p. 20078-20098, 2009.

[181] C.A. Klein and G.F. Cardinale, "Young's modulus and Poisson's ratio of CVD diamond," *Diamond and Related Materials*, vol. 2, no. 5–7, p. 918-923, 1993.

[182] A.R. Lang, "The strain-optical constants of diamond: A brief history of measurements," *Diamond and Related Materials*, vol. 18, no. 1, p. 1-5, 2009.

[183] A. Gaidarzhy, M. Imboden, P. Mohanty, J. Rankin, and B.W. Sheldon, "High quality factor gigahertz frequencies in nanomechanical diamond resonators," *Applied Physics Letters*, vol. 91, no. 20, p. 203503, 2007.

[184] A.H. Safavi-Naeini, J. Chan, J.T. Hill, S. Gröblacher, H. Miao, Y. Chen, M. Aspelmeyer, and O. Painter, "Laser noise in cavity-optomechanical cooling and thermometry," *New Journal of Physics*, vol. 15, no. 3, p. 035007, 2013.

[185] E.S. Zouboulis, M. Grimsditch, A.K. Ramdas, and S. Rodriguez, "Temperature dependence of the elastic moduli of diamond: A Brillouin-scattering study," *Physical Review B*, vol. 57, no. 5, p. 2889-2896, 1998.

[186] L. Kipfstuhl, F. Guldner, J. Riedrich-Möller, and C. Becher, "Modeling of optomechanical coupling in a phoxonic crystal cavity in diamond," *Optics Express*, vol. 22, no. 10, p. 12410-12423, 2014.

[187] K. Fang, M.H. Matheny, X. Luan, and O. Painter, "Phonon routing in integrated optomechanical cavity-waveguide systems," *arXiv:1508.05138*, 2015.

[188] K. Stannigel, P. Rabl, A.S. Sørensen, P. Zoller, and M.D. Lukin, "Optomechanical Transducers for Long-Distance Quantum Communication," *Physical Review Letters*, vol. 105, no. 22, p. 220501, 2010.

[189] A. Sipahigil, R. E. Evans, D. D. Sukachev, M. J. Burek, C. Nguyen, J. Borregaard, M. Bhaskar, J. Pacheco, H. Atikian, R. M. Camacho, F. Jelezko, E. Bielejec, H. Park, M. Loncar, and M.D. Lukin, "Quantum optical switch controlled by a color center in a diamond nanocavity," *In preparation*, 2015.

[190] P. Tamarat, T. Gaebel, J.R. Rabeau, M. Khan, A.D. Greentree, H. Wilson, L.C.L. Hollenberg, S. Prawer, P. Hemmer, F. Jelezko, and J. Wrachtrup, "Stark Shift Control of

Single Optical Centers in Diamond," *Physical Review Letters*, vol. 97, no. 8, p. 083002, 2006.

[191] C. Matthiesen, M.J. Stanley, M. Hugues, E. Clarke, and M. Atatüre, "Full counting statistics of quantum dot resonance fluorescence," *Scientific Reports*, vol. 4, p. 4911, 2014.

[192] D. Englund, B. Shields, K. Rivoire, F. Hatami, J. Vučković, H. Park, and M.D. Lukin, "Deterministic Coupling of a Single Nitrogen Vacancy Center to a Photonic Crystal Cavity," *Nano Letters*, vol. 10, no. 10, p. 3922-3926, 2010.

[193] A. Badolato, K. Hennessy, M. Atatüre, J. Dreiser, E. Hu, P.M. Petroff, and A. Imamoğlu, "Deterministic Coupling of Single Quantum Dots to Single Nanocavity Modes," *Science*, vol. 308, no. 5725, p. 1158-1161, 2005.

[194] D.E. Chang, A.S. Sorensen, E.A. Demler, and M.D. Lukin, "A single-photon transistor using nanoscale surface plasmons," *Nat Phys*, vol. 3, no. 11, p. 807-812, 2007.

[195] L.M. Duan and H.J. Kimble, "Scalable Photonic Quantum Computation through Cavity-Assisted Interactions," *Physical Review Letters*, vol. 92, no. 12, p. 127902, 2004.

[196] D. Witthaut, M.D. Lukin, and A.S. Sørensen, "Photon sorters and QND detectors using single photon emitters," *EPL (Europhysics Letters)*, vol. 97, no. 5, p. 50007, 2012.